Patrick Johannes Fritzl, BSc

Numerical Simulation of Electron Beam Welding of Copper

Master's Thesis

to achieve the university degree of
Master of Science / Diplom-Ingenieur
Master's degree programme: Mechanical Engineering

submitted to

Graz University of Technology

Supervisor †
Assoc.Prof. Dipl.-Ing. Dr.techn. Norbert Enzinger

Advisory support ‡
Prof. Dr. Gleb A. Turichin
Dr. Ekaterina Valdaitseva

† Institute of Materials Science and Welding, Graz University of Technology, Austria
‡ Institute of Laser and Welding Technology, St. Petersburg State Polytechnic University, Russia

Graz, January 2016

Affidavit

I declare that I have authored this thesis independently, that I have not used other than the declared sources/resources, and that I have explicitly indicated all material which has been quoted either literally or by content from the sources used. The text document uploaded to TUGRAZonline is identical to the present master's thesis.

Date	Signature

Abstract

In an experimental study, conducted at the Institute of Materials Science and Welding at Graz University of Technology, the electron beam welding of heavy-section copper materials was investigated. Welding defects, especially in the root area of the seams, have been characterised and adequate measures to prevent these very defects were suggested.

The numerical simulation of this process has the potential to give insights in defect formation processes and to ease the determination of actions to be taken as well as to find an ideal set of welding parameters.

As a possible tool for the simulation of electron beam welding on copper materials LaserCAD was investigated. The software was developed at St. Petersburg State Polytechnic University for the numerical simulation of beam welding processes.

With the help of parameter studies a reasonable behaviour of LaserCAD's mathematical model, based on absorption and reflexion of the impinging electron beam, could be proven. In a majority of cases, the validation with suitable experiments revealed good accordance of simulation and reality.

Despite many simplifications of the program such as the restriction on quasi-static processes and welds without beam oscillation, insightful results could be worked out with regard to the welding behaviour of different copper alloys. Basic preconditions for useful results are knowledge about thermo-physical characteristics of the investigated materials and data about beam parameters of the electron beam welding system. However, restrictions could be seen in the calculation of highly conductive copper grades.

Kurzfassung

In einer experimentellen Studie, durchgeführt am Institut für Werkstoffkunde der Technischen Universität Graz, wurde das Elektronenstrahlschweißen dickwandiger Kupfermaterialien untersucht. Schweißfehler, vor allem im Bereich der Wurzel, konnten beschrieben und Ansätze zur Verhinderung derselben gefunden werden.

Die numerische Simulation des Prozesses hat das Potential, Einblicke in Defektformation zu geben und die Ermittlung geeigneter Maßnahmen und idealer Schweißparameter zu erleichtern.

Als mögliches Werkzeug für die Simulation von Elektronenstrahlschweißen von Kupfer wurde LaserCAD untersucht. Die Software wurde an der Polytechnischen Universität St. Petersburg für die numerische Simulation von Strahlschweißverfahren entwickelt.

Mit Hilfe von Parameterstudien konnte ein plausibles Verhalten des hinterlegten mathematischen Modells, das auf Reflexion und Absorption des auftreffenden Elektronenstrahls beruht, nachgewiesen werden. Die Validierung mit geeigneten Experimenten ergab großteils gute Übereinstimmungen zwischen Simulation und Realität.

Trotz vieler Vereinfachungen des Programms wie etwa der Beschränkung auf quasistatische Prozesse und Schweißungen ohne Strahloszillation konnten aufschlussreiche Ergebnisse hinsichtlich des Schweißverhaltens unterschiedlicher Kupferlegierungen erarbeitet werden. Als Grundvoraussetzung für brauchbare Resultate sind Kenntnisse über die thermophysikalischen Kennwerte der untersuchten Materialien sowie das Wissen über die Strahlparameter der Elektronenstrahlschweißanlage zu nennen. Einschränkungen sind jedoch vor allem in der Berechnung hoch leitender Kupfersorten zu sehen.

Резюме

В ходе экспериментального исследования, приведенного в Институте Металловедения Технического Университета Граца, был рассмотрен процесс электронно-лучевой сварки толстостенных медных материалов. Таким образом, дефекты сварки, проявляющиеся в частности в области корни сварочного шва, были описаны и методы предотвращения этих дефектов были найдены.

Благодаря цифровому моделированию сварочного процесса можно исследовать образование дефектов и облегчить определение подходящих методов и идеальных параметров сварочного процесса. В качестве возможного инструмента для моделирования процесса электронно-лучевой сварки меди была рассмотрена программа LaserCAD. Эта программа была разработана экспертами в Санкт-Петербургском Политехническом Университете для цифрового моделирования процессов лазерной и электронно-лучевой сварки.

С помощью исследований параметров вероятное поведение сохраненной математической модели, основывающейся на отражении и поглощении падающего электронного луча, было подтверждено. При последующей валидации результатов с соответствующими экспериментами в большинстве случаев показалось хорошее соответствие между параметрами смоделированного и реального сварочного процесса.

Несмотря на многие средства упрощения программы, как например, ограничение на квазистатические процессы и сварочные процессы без осцилляции электронного луча, в ходе исследования были достигнуты содержательные результаты касательно поведения разных медных сплавов при сварочном процессе. Основной предпосылкой для получения содержательных результатов являются знания о термофизических параметрах исследованных материалов, а также знания о параметрах луча машины электронно-лучевой сварки. Прежде всего, ограничения стали видны при моделировании медных материалов, обладающих высокой проводимостью.

Translated into Russian by
Mag[a]. Magdalena Heu

Acknowledgements

First of all, I want to express my deep gratitude to my supervisor Assoc.Prof. Dipl.-Ing. Dr.techn. Norbert Enzinger for his proficient support. He always took his time and had a sympathetic ear for my requests, especially during my stay in Russia, where Skype conferences at extraordinary hours were held. I am thankful for the aspiring conversations, his patience and his helping guidance throughout the last months.

I place on record, my sincere thanks to Dr. Gleb A. Turichin, head of Institute of Laser and Welding Technology (ILWT) at St. Petersburg State Polytechnic University, who provided expertise and insight in the software used in this thesis and gave me the opportunity to execute my research at his institute.

Furthermore I want to express my gratitude to all members of ILWT who helped me before, during and after my time in Russia, especially Dr. Ekaterina Valdaitseva for her endeavours to acquaint me with the software and her untiring efforts in answering my questions. I would also like to thank Dr. Olga Klimanova for her support in journey preparation and organisation of the dormitory, as well as Dr. Vladislav Somonov for his shared expertises and his qualification as a pleasant dining companion.

My sincere thanks also goes to head of Institute for Materials Science and Welding (IWS) at Graz University of Technology, Univ.-Prof. Dipl.-Ing. Dr.techn. Priv.-Doz. Christof Sommitsch, who gave me the possibility to work in such a pleasant atmosphere at IWS and to do my research in St. Petersburg.

Moreover I wish to express my gratitude to all members of IWS for their help and support. Especially Dipl.-Ing. Christopher Wiednig for his effort to gain experimental data, Georg Weber for the provision of the bell-casting bronze material, Leander Herbitschek for his help with the experiments and Thomas Friedl for his support in specimen preparation.

In addition, I want to thank the Faculty of Mechanical Engineering and Economic Sciences at Graz University of Technology for supporting this thesis with the Clever & Smart research grant.

I also want to thank Peter, Yunfei, Klaus and Zsolt, my dormitory roommates in St. Petersburg, who made my stay in Russia unforgettable.

Last but not least, I would like to thank the most important people in my life. My parents and my sister for supporting me spiritually throughout my studying and my life in general. And my girlfriend Lena for her unceasing encouragement, support and attention, giving me the strength and confidence for this venture.

Table of Contents

List of Figures

List of Tables

List of Acronyms

CCD	Central composite design plan
CCT	Continuous cooling transformation
DoE	Design of experiments
EB	Electron beam
EBW	Electron beam welding
fcc	Face centred cubic
FZ	Fusion zone
GMAW	Gas metal arc welding
HTM	Heat transfer model
HAZ	Heat affected zone
IACS	International annealed copper standard
ILWT	Institute of Laser and Welding Technology at St. Petersburg State Polytechnic University
IWS	Institute of Materials Science and Welding at Graz University of Technology
LBW	Laser beam welding
OFW	Oxyfuel welding
SAW	Submerged-arc welding
SMAW	Shielded metal arc welding
SPbSPU	St. Petersburg State Polytechnic University
TC	Thermocouple
TU Graz	Graz University of Technology

Chapter 1

Introduction

At the Institute of Materials Science and Welding (IWS) at Graz University of Technology, many projects in the research field of joining technology are dedicated to electron beam welding (EBW). The motive for this thesis goes back to a research project, in which the EBW process on heavy-section copper materials was studied [1].

With the academic software LaserCAD [2], provided by its developers from the Institute of Laser and Welding Technology (ILWT) at St. Petersburg State Polytechnic University (SPbSPU), the electron beam welding process of copper materials shall be modelled.

Under the supervision of the developer and head of ILWT Prof. Turichin, first calculations, which were done in order to to get acquainted with LaserCAD, took place in St. Petersburg during a stay for two months.

Figure 1.1: *Emblem of* St. Petersburg State Polytechnic University *in front of the main building*

1.1 Background

In [1], EBW of heavy-section unalloyed copper material Cu-DHP with thicknesses of 30 mm was investigated at the IWS. As a crucial issue at these weldings, a lack of fusion in the root area of the welds emerged. It is assumed that, as described in [3, p. 512], the very small melting range of unalloyed copper (~ 3 °C) is responsible for these welding defects. The transition from solid to liquid occurrs suddenly and the melt is highly fluid (inviscid), hence run outs in flat position can easily happen.

Based on the experimental data from IWS, it was planned to numerically model the EBW process for this very material with the software LaserCAD. The special software, represented in [4], can be used for process simulations of beam welding processes. LaserCAD is developed by Prof. Turichin and his team at ILWT, SPbSPU, one of ten strategic partner universities of TU Graz. Since the majority of ILWT's research deals with laser beam welding processes, the focus of LaserCAD rests on this very welding process, yet it also provides a model for electron beam welding.

1.2 Objectives

The following lines will present and elucidate the objectives this work is proposed to accomplish.

1.2.1 Leading question

The goal of the current thesis is the simulation of the EBW process on thick-walled copper materials with LaserCAD in accordance with the existing experimental data from a research project at IWS at TU Graz [1]. Analysis and parameter studies with the numerical software on these weldings shall be done to explain the process of defect formation and, in addition, find possibilities to control them. Generalised it brings us to the leading question:

Leading question
Is LaserCAD a useful tool for the simulation of electron beam welding of thick-walled copper materials?

1.2.2 Secondary questions / simulation goals

In order to get a more structured outcome, following secondary questions were defined. They can be seen as a breakdown of the leading question and pursue the aim to raise the information value in contrast to solely answering aforementioned question.

Secondary question 1
How accurate is the calculated seam geometry in relation to the experimental data?

One of the main advantages of welding processes with beams of high energy density is the keyhole or deep penetration welding effect. Thus the achievable penetration depth is seen as the most important outcome of the geometry-related calculation results. Nevertheless, additional significant factors like area and shape of the fusion zone need to be examined as well.

Secondary question 2
Can LaserCAD be used to estimate occurring welding defects?

The avoidance of welding defects such as pores, spatters, root craters, run outs, etc. is the prime target when developing a welding process to join mechanical components. With a simulation tool that is able to predict such defects, experimental work and the finding of proper parameters for a stable process could be economised.

Secondary question 3
How sensitive is LaserCAD in welding parameter influences?

Virtual investigations on the influence of different welding parameters in keyhole formation, weld geometry, molten pool geometry, weld pool dynamics, etc. would expose useful potential to save time and money consuming experiments.

Secondary question 4
How sensitive is LaserCAD according to different copper alloys?

Referring to the experimental work from [1], different copper alloys showed completely different behavior. Especially the root formation as well as the appearance of runouts and pores are strongly connected to the alloy composition in the fusion zone.

Chapter 2

Theoretical aspects

2.1 Copper materials

If not denoted otherwise, the information represented in this section is from [5].

Copper is a nonferrous metal with a face centred cubic (fcc) crystal lattice. In the Periodic Table of Elements, copper with the element symbol Cu, has the atomic number 29. With a density of about 8.96 $\mathrm{g/cm^3}$, copper is part of the group of heavy metals[1]. Table 2.1 gives an overview of characteristics and physical properties of pure copper. Due to its excellent electrical and thermal conductivity as well as its high corrosion resistance, copper holds a high technical importance in a wide field of application.

Table 2.1: *Physical properties of copper [7]*

Attribute	Value		Note
Element symbol	Cu		
Atomic number	29		
Crystal lattice	fcc		
Atomic weight	63.546	$\mathrm{g/mol}$	
Density	8.96	$\mathrm{g/cm^3}$	
Melting temperature	1083.4	°C	
Boiling temperature	2567	°C	at atmospheric pressure
Electrical conductivity at 20 °C	max. 60	$\mathrm{m/(\Omega\ mm^2)}$	$\hat{=}$ 103.4 % IACS
Thermal conductivity at 20 °C	395	$\mathrm{W/(m\ K)}$	
Heat capacity at 20 °C	380	$\mathrm{J/(kg\ K)}$	from 20 to 400 °C
Thermal expansion coefficient	17	$\mathrm{10^{-6}/K}$	from 25 to 300 °C
Young's modulus	125 000	$\mathrm{N/mm^2}$	from [5]
Tensile strength †	200 ... 360	$\mathrm{N/mm^2}$	from [5]
Fracture elongation †	2 ... 45	%	from [5]

† Minimum value, depending on copper material and treating condition

Copper materials can basically be divided into two groups. The group of unalloyed copper materials embraces all end products of copper production, regardless how many admixtures needed for the production process were removed. This is necessary

[1] Metal materials with density $\rho > 5\,\mathrm{g/cm^3}$ [6]

to achieve certain properties. On the other hand, there is the group of alloyed copper materials, where intentionally different amounts of alloy components are added to influence the material properties.

2.1.1 Unalloyed copper

With its face centred cubic crystal structure, copper is a very ductile material and has good values in low-temperature impact resistance. Owing to the high ductility at low strength, copper has favourable conditions for plastic forming and can easily be formed to pipes, wires, profiles, shells, etc. Cross section area reductions of over 90 % are possible with appropriate forming processes. The moderate strain hardening behaviour of copper can be neutralised with quite low annealing temperatures (Figure 2.1a). Strength properties of unalloyed copper depend in some extend on the amount of dissolved additions. The strength of pure copper is the lowest. Even moderate increased temperatures reduce the strength of all copper materials (Figure 2.1b). Table 2.2 gives a brief overview and characterisation of selected unalloyed copper grades.

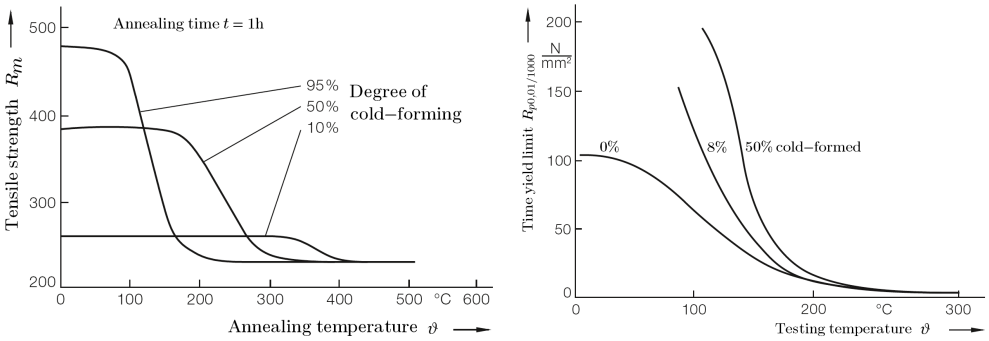

(a) *Recrystallisation annealing of cold-formed copper*

(b) *Creep behaviour of copper*

Figure 2.1: *Recrystallisation annealing as well as creep behaviour of copper; adapted from [5]*

Table 2.2: *Characterisation, electrical and thermal conductivity of selected unalloyed copper materials [5]*

Standard DIN EN 1976 (DIN 1708)	Chemical comp. wt. %	Characteristics and typical usage
Cu-DHP (SF-Cu)	Cu ≥ 99.90 P = 0.015 . . . 0.04	Deoxidised copper with a relatively high amount of residual phosphorus. Used for applications with low requirements in electrical conductivity. Very good weldability and brazeability, not susceptible to hydrogen embrittlement.
Cu-DLP (SW-Cu)	Cu ≥ 99.90 P = 0.005···0.014	Deoxidised copper with limited amount of residual phosphorus, weldable.
Cu-ETP (E1-Cu 58)	Cu ≥ 99.90 O_2 = 0.005 . . . 0.04	By electrolytic deposition refined high-conductivity copper with low oxygen content.
Cu-OF (OF-Cu)	Cu ≥ 99.95	Oxygen free high-conductivity copper. Fulfils high requirements of hydrogen resistance.

The electrical conductivity[2] of copper, which is ~ 60 $^{m}/_{\Omega mm^2}$, is nearly six times higher than iron ones, 60 % higher than aluminium ones and can only be surpassed by the conductivity of silver. According to WIEDEMANN-FRANZ's law, thermal conductivity is proportional to electrical conductivity.

Table 2.3: *Selected thermophysical properties for different copper grades, bronze and steel [3]*

Standard	Melting point (or range)	Thermal expansion coefficient (25 ... 300 °C)	Heat capacity (20 ... 400 °C)	Thermal conductivity (at 20 °C)
	°C	$^{10^{-6}}/_{K}$	$^{J}/_{(kg\ K)}$	$^{W}/_{(m\ K)}$
Copper grades according to DIN EN 1976 (DIN 1708)				
Cu-DHP (SF-Cu)	1083	17	380	240 ... 360
Cu-ETP (E1-Cu 58)	1083	17	380	≤ 386
Cu-DLP (SW-Cu)	1083	17	380	≤ 345
Cu-OF (OF-Cu)	1083	17	380	393
Cu-FRHC (OF-Cu)	1083	17	380	≤ 384
Phosphorus bronze (Copper/Tin)				
CuSn6 [8]	900 ... 1050	18.5	377	75
Steel grades				
Low-carbon steel † [3]	1500 ... 1530	12	470	34
1.4313 ‡ [9]	1450 ... 1510	11.6	430	25

† 0.05 % ... 0.12 % C; 0.2 % ... 0.4 % Mn; 0.4 % P+S
‡ X3CrNiMo13-4: Martensitic nickel–chromium stainless steel with molybdenum addition

To a large extend, the conductivity depends on the degree of purity of the copper material. Both, thermal and electrical conductivity can be affiliated to the mobility of electrons in the metallic state. Foreign atoms in the crystal lattice lead to interferences, affect the electron mobility negatively and decrease the conductivity. Even small amounts of impurities can lead to a strong increase of the electrical resistivity (Figure 2.2).

Table 2.3 compares different unalloyed copper grades with a copper-tin bronze material and steel grades. The thermal conductivity of unalloyed copper grades reaches values up to 393 $^{W}/_{(mK)}$ at room temperature. A tin amount of 6 % leads to a drastically drop of thermal conductivity to 75 $^{W}/_{(mK)}$. The conductivity of steel in contrast is with ~ 30 $^{W}/_{(mK)}$ a fraction of copper ones.

In [10], different thermophysical values for pure copper at high temperatures were investigated and an extract is presented in Figure 2.3. At the melting point, a distinct drop of thermal conductivity λ can be observed. Likewise, a drop in thermal diffusivity a, as a consequence of equation (2.1), can be noticed as well (Figure 2.3c).

$$a = \frac{\lambda}{c_p\,\rho} \tag{2.1}$$

Heat capacity c_p remains roughly constant, excepting a peak at melting point in consequence of the discontinuity in the enthalpy graph corresponding to the latent heat of melting ΔH_{SL}.

[2] Measured in $^{m}/_{(\Omega\ mm^2)}$ or % IACS (International Annealed Copper Standard); 100 % IACS corresponds to 58 $^{m}/_{(\Omega\ mm^2)}$ (Cu-ETP quality) [7]

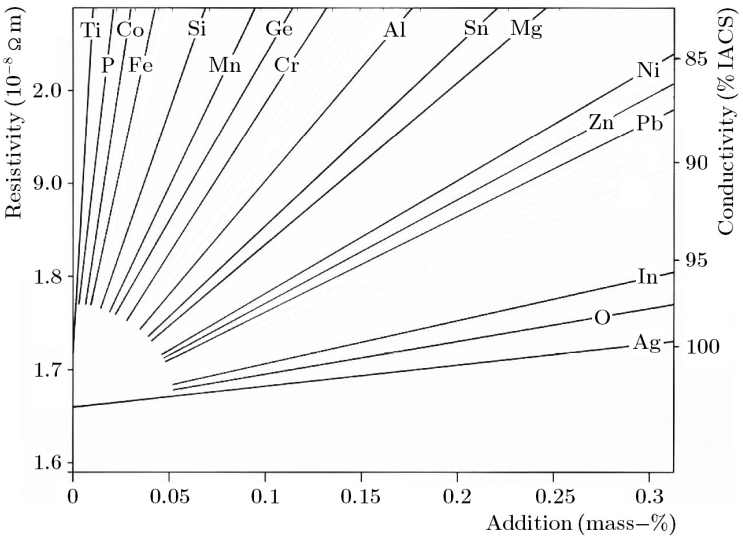

Figure 2.2: *Influence of impurities on the electrical conductivity of copper; adapted from [11]*

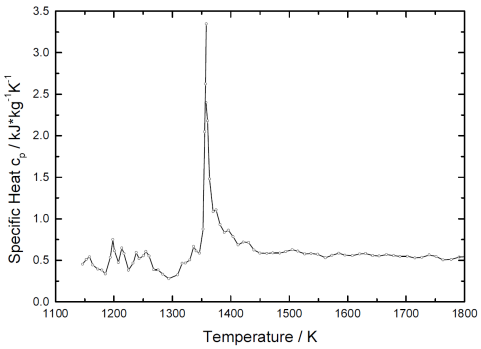

(a) *Heat capacity c_p versus temperature*

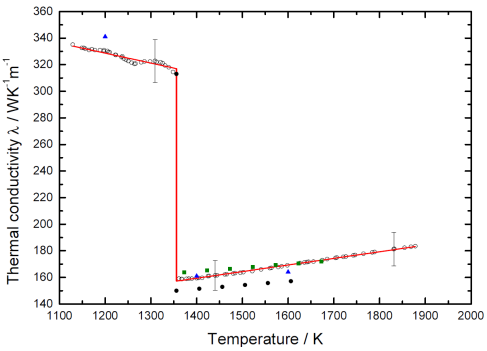

(b) *Thermal conductivity λ versus temperature*

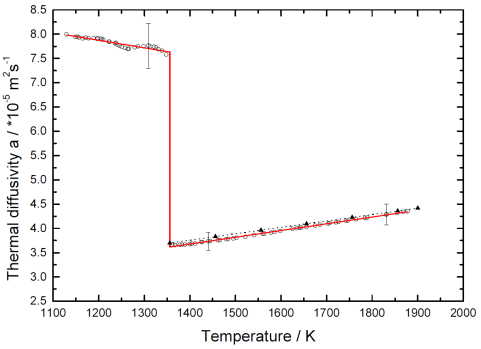

(c) *Thermal diffusivity a versus temperature*

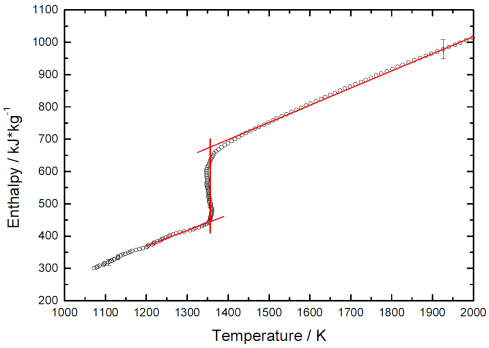

(d) *Enthalpy versus temperature*

Figure 2.3: *Thermal dependency of heat capacity c_p, thermal conductivity λ, thermal diffusivity a and enthalpy of pure copper at high temperatures [10]*

With regard to their intended purpose, one can distinguish between copper grades for electro-technical purpose, mostly oxygen-bearing and thus not suitable for welding (e.g. Cu-ETP, Cu-FRHC), and phosphorusdeoxidised, oxygen-free copper grades for apparatus engineering (e.g. Cu-DHP, Cu-OF), whose welding behaviour is good. [3]

In Table 2.4, several thermophysical properties of pure copper and Cu-DHP needed for the numerical simulation with LaserCAD from different sources are listed.

Table 2.4: *Thermophysical properties of Cu-DHP or pure Cu from different sources*

Attribute		Value	Note	Source
Melting point temperature	T_M	1083 °C		[12, 13]
Boiling point temperature	T_B	2595 °C	pure Cu	[13, 14]
		2562 °C	pure Cu	[15, 16]
Heat capacity	c_p	386 $^{J}/_{(kg\ K)}$	at 20 °C	[12, 13]
		415 $^{J}/_{(kg\ K)}$	at 300 °C	[12]
		427 $^{J}/_{(kg\ K)}$	pure Cu at 500 °C	[17]
		473 $^{J}/_{(kg\ K)}$	pure Cu at 1000 °C	[17]
Density	ρ	8.94 $^{g}/_{cm^3}$	at 20 °C	[12]
		8.92 $^{g}/_{cm^3}$	at 20 °C	[13]
		8.33 $^{g}/_{cm^3}$	at 1083 °C	[12]
		8.32 $^{g}/_{cm^3}$	at 1083 °C (solid)	[13]
		7.99 $^{g}/_{cm^3}$	at 1083 °C (liquid)	[13]
Thermal conductivity	λ	305 $^{W}/_{(m\ K)}$	at 20 °C	[12]
		334 $^{W}/_{(m\ K)}$	at 200 °C	[12]
		300 $^{W}/_{(m\ K)}$	pure Cu at 27 °C	[15]
		339 $^{W}/_{(m\ K)}$	pure Cu at 927 °C	[15]
		244 $^{W}/_{(m\ K)}$	pure Cu at 1037 °C	[17]
Surface tension coefficient	σ_L	1.585 $^{N}/_{m}$	pure Cu	[18]
		1.290 $^{N}/_{m}$	pure Cu	[19]
Surface tens. temp. coeff.	σ_T	$-0,211$ $^{mN}/_{(m\ K)}$	pure Cu	[18]
		-0.234 $^{mN}/_{(m\ K)}$	pure Cu	[19]
Latent heat of evap.	ΔH_{LG}	4827 $^{kJ}/_{kg}$	calc. by LaserCAD	[2]
		4730 $^{kJ}/_{kg}$	pure Cu	[20, 21]

2.1.2 Alloyed copper

Since copper can be alloyed with numerous elements (e.g. Zn, Sn, Mn, Ni, Al, Fe, Cr, Be, Cd, Si), alloy systems of a great number are available. As well as unalloyed copper, most alloyed copper materials are one-phase materials, depending on the amount and type of alloying elements. Providing the alloy has sufficient ductility, copper alloys can be strain hardened and some alloys can be precipitation hardened.

Most important copper alloys are brass (Cu-Zn), bronzes (Cu-Sn, Cu-Al, Cu-Mn, Cu-Si), gunmetals (Cu-Sn-Zn-Pb), copper-nickel alloys, nickel silver (Cu-Ni-Zn) and beryllium coppers as the hardest and strongest of any copper alloy. [22]

Since in [1], copper-tin bronze is used as filler metal, a closer look on the Cu-Sn system is taken in this section.

Copper-tin bronze

The alloy system copper-tin is the classical bronze material. According to the equilibrium diagram, Cu-Sn alloys solidify as one-phase alloys up to a tin amount of 14 % (Figure 2.4a).

Usually small amounts of phosphorus are added for deoxidisation, this is why tin bronze materials are also known as phosphorus bronzes. The addition of phosphorus is leading to more complex solidification processes than depicted in the two-phase diagram. With an amount of 0.2 % P, the equilibrium diagram changes its shape with a strongly increased melting range (Figure 2.4b). The brittle and phosphorus-rich δ-phase appearing in the primary microstructure can be resolved by an appropriate heat treatment in the area of the α-solid solution.

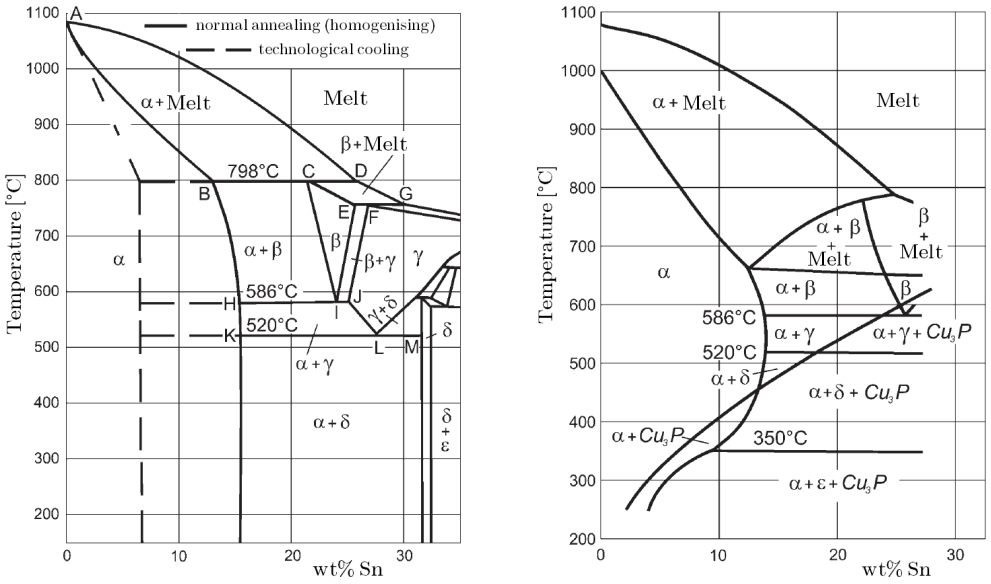

(a) *Equilibrium diagram for Cu-Sn*

(b) *Equilibrium diagram for Cu-Sn-P with 0.2 % P*

Figure 2.4: *Equilibrium diagram for copper-tin and copper-tin-phosphorus; adapted from [23]*

Up to ~ 6 % tin, a homogenisation of the primary microstructure to maintain optimum toughness at technically acceptable annealing times can be accomplished (e.g. 24 h at 650 °C).

Low-alloyed bronzes with 1.5 % tin in hard-drawn condition are commonly used as wires for telephone lines. For this kind of application, the bronze material needs to be phosphorus free (regard Figure 2.2).

Wrought bronzes with tin amounts of 6 %...8 % and tensile strengths around 900 $^{N}/_{mm^2}$ are used for relay springs. Soft bronze wires are widely used for the production of metal screens for paper industry.

Cast alloys use the strength increasing effect of tin up to an amount of 14 %. In the primary microstructure, the fcc, yet brittle δ-phase appears in a great extend.

For the application in mechanical engineering, it is essential to get rid of this ductility minimising components by the use of a heat treatment. Looking at Figure 2.4, this is possible up to a composition of 14 % Sn.

Cast bronzes with tin amounts of 12 % ... 14 % reach maximum strength at adequate ductility and are used for e.g. gears and other highly stressed parts. Cast bronze with 20 % tin is very hard and brittle, thus unsuitable for mechanical engineering but, among other things, used for bell casting.

In Figure 2.5, the influence of tin on selected physical and mechanical properties is shown. As already mentioned, with increasing tin amount, tensile strength R_m increases. Fracture elongation reaches a maximum at ~ 5 % tin. Electrical and, correspondingly, thermal conductivity decrease rapidly with increased tin amount.

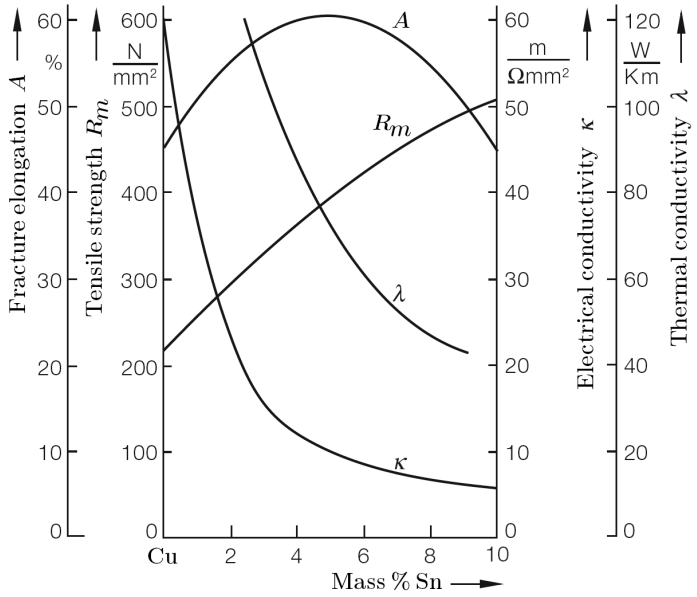

Figure 2.5: *Physical and mechanical properties of copper-tin alloys with different amounts of tin [5]*

In Table 2.5, density ρ, heat capacity c_p and thermal conductivity λ for different bronze materials and for the unalloyed copper grade Cu-DHP are listed. The values are graphically depicted in Figure 2.6. With increasing tin amount heat conductivity remains quite constant, density decreases slightly and thermal conductivity decreases strongly in common with Figure 2.5. On the supposition that these tendencies continue, properties of the bell casting bronze material with 20 % tin can roughly be estimate to $\rho = 8.56\,\mathrm{g/cm^3}$, $c_p = 0.37\,\mathrm{J/(kg\,K)}$, $\lambda_{(20\,^\circ\mathrm{C})} = 48\,\mathrm{W/(m\,K)}$ and $\lambda_{(200\,^\circ\mathrm{C})} = 60\,\mathrm{W/(m\,K)}$.

The numerical simulation with LaserCAD requires the input of the surface tension coefficients. Surface tension depending on temperature $\sigma(T)$ is approximated with the surface tension coefficient σ_L and the surface tension temperature coefficient σ_T according to equation (2.2).

$$\sigma(T) = \sigma_L + \sigma_T \cdot T \tag{2.2}$$

In [18] and [19], coefficient values for copper and copper-tin alloys are given. Based on that data, values for CuSn6 and Cu80 Sn20 were estimated by interpolation. The values of the surface tension σ versus the temperature T are graphically depicted in Figure 2.7.

Table 2.5: *Thermophysical properties of Cu-Sn alloys and Cu-DHP from different sources*

Material	Sn %	ρ (20 °C) g/cm³	c_p (20 °C) J/(kg K)	λ (20 °C) W/(m K)	λ (200 °C) W/(m K)	Source
Cu-DHP	0	8.94	386	305	334	[12]
CuSn4	4	8.85	377	90	120	[24]
CuSn6	6	8.82	377	75	98	[8]
CuSn8	8	8.79	377	67	81	[25]
CuSn10-C	10	8.74	380	59	76	[26]
CuSn12-C	12	8.72	376	55	70	[27]

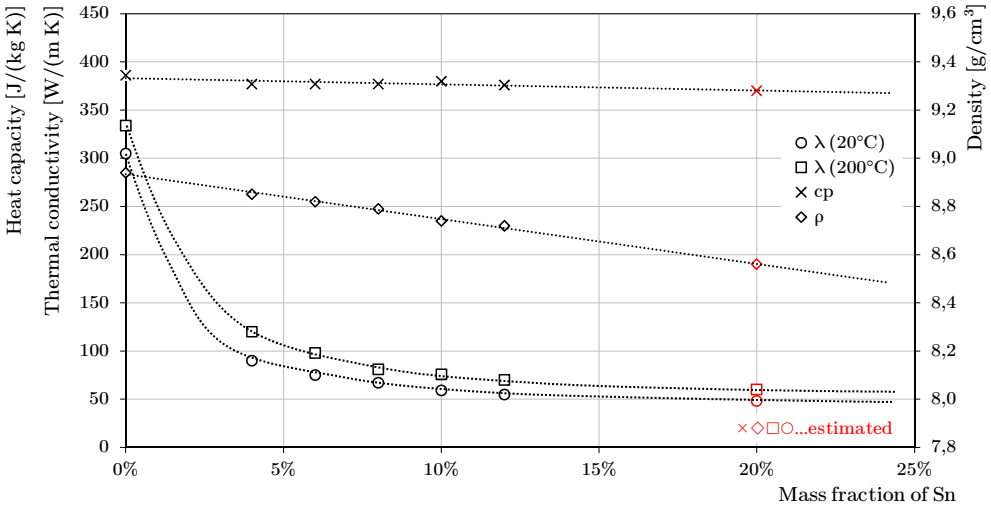

Figure 2.6: *Thermophysical properties of copper-tin alloys with different amounts of tin according to data from Table 2.5*

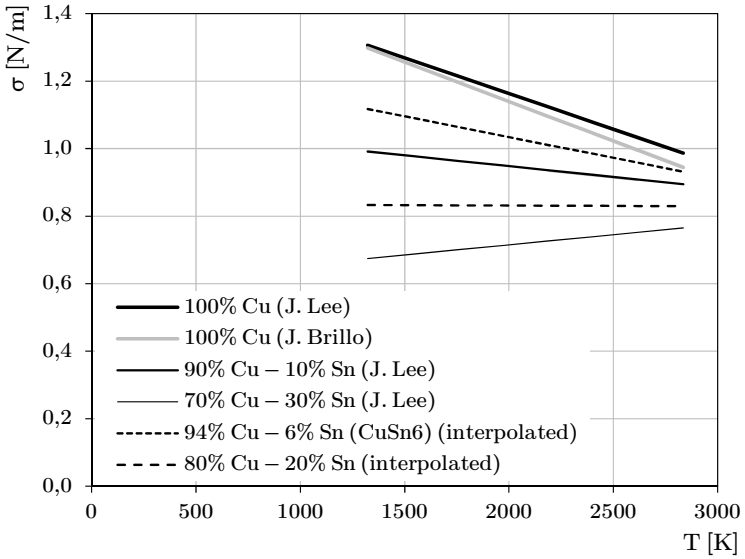

Figure 2.7: *Estimation of surface tension of Cu-Sn alloys; Reference data from J. Lee [18] and J. Brillo [19]*

Table 2.6: *Thermophysical properties of CuSn6 respectively of their main alloy components*

Attribute		Value	Note	Source
Melting point temperature	T_M	900 °C	solidus	[8]
		1050 °C	liquidus	[8]
Boiling point temperature	T_B	2595 °C	pure Cu	[13, 14]
		2562 °C	pure Cu	[15, 16]
		2270 °C	pure Sn	[21]
		2602 °C	pure Sn	[16]
Heat capacity	c_p	377 $^{\mathrm{J}}/_{(\mathrm{kg\ K})}$	at 20 °C	[8]
Density	ρ	8.82 $^{\mathrm{g}}/_{\mathrm{cm}^3}$	at 20 °C	[8]
Thermal conductivity	λ	75 $^{\mathrm{W}}/_{(\mathrm{m\ K})}$	at 20 °C	[8]
		98 $^{\mathrm{W}}/_{(\mathrm{m\ K})}$	at 100 °C	[8]
Surface tension coefficient	σ_L	1.28 $^{\mathrm{N}}/_{\mathrm{m}}$	see Figure 2.7	
Surface tens. temp. coeff.	σ_T	−0.123 $^{\mathrm{mN}}/_{(\mathrm{m\ K})}$	see Figure 2.7	
Latent heat of evap.	ΔH_{LG}	4827 $^{\mathrm{kJ}}/_{\mathrm{kg}}$	calc. by LaserCAD	[2]
		4730 $^{\mathrm{kJ}}/_{\mathrm{kg}}$	pure Cu	[20, 21]
		2492 $^{\mathrm{kJ}}/_{\mathrm{kg}}$	pure Sn	[21]

2.1.3 Welding of copper materials

The information given in this chapter is based on [3]. Other sources are denoted separately.

On a large scale, the welding behaviour of copper is influenced by the following five material characteristics:

- Thermal conductivity
- Oxygen content
- Thermal expansion
- Tendency to gas absorption
- Viscosity of the melt pool

Thermal conductivity

The high thermal conductivity makes copper materials difficult to weld. Compared to unalloyed steels, the thermal conductivity is approximately seven times higher at room temperature and up to 15 times higher at 1000 °C. In consequence, a large amount of the heat introduced in the fusion zone flows into the base material and cannot be used to melt the material. To maintain a fusion weld, either a highly concentrated heat source (e.g. electron beam welding) is required or, when welding with processes of lower energy density, preheating at temperatures up to 600 °C is necessary.

Since minimal amounts of admixtures can strongly decrease the thermal conductivity (Figure 2.2), copper alloys usually do not need to be preheated or only to a much lower temperature level.

Oxygen content

The oxygen amount of oxygen-bearing coppers lays within 0.005 and 0.04 %. Especially for electro-technical applications, oxygen is applied for the oxidation of impurities during the refining process to increase the electrical conductivity [28]. Generally in copper as the base material, oxygen exists ligated as copper oxide Cu_2O, which forms an eutectic system with Cu. The cooling of an oxygen-bearing copper melt results in a structure of primary α(Cu) and eutectic (α-)Cu_2O. The brittle Cu_2O is concentrated at the grain boundaries. After the following recrystallisation during the hot forming process, these depositions are finely crushed and dispersed, so that mechanical properties or electrical and thermal conductivity are not negatively affected.

When heated to levels of high temperature the copper oxide has a tendency to accumulate at the grain boundaries (Figure 2.8a). In the heat affected zone (HAZ) of the weld, this concentration of brittle Cu_2O causes significant reduction of material strength and ductility.

If oxygen-bearing coppers are heated in hydrogen-containing atmospheres (e.g. conventional gas welding) with the so-called Hydrogen embrittlement another complicating factor can appear. Atomic hydrogen is able to diffuse into solid and heated copper (to more than 1065 °C) and reduces the oxides at the grain boundaries:

$$2\ H + Cu_2O \longrightarrow 2\ Cu + (H_2O)_{vapour}$$

The steam created during this process is insoluble in copper and cannot diffuse. High pressure builds up and the material "bursts". Figure 2.8b shows the metallographic analysis of a copper microstructure suffering from hydrogen embrittlement.

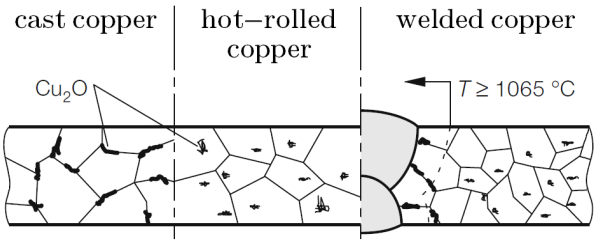

(a) *Dispersion of eutectic* Cu_2O *in cast (left) and hot formed copper (middle) and the accumulation of brittle* Cu_2O *at the grain boundaries in the heat affected zone of a weld seam (right); adapted from [3]*

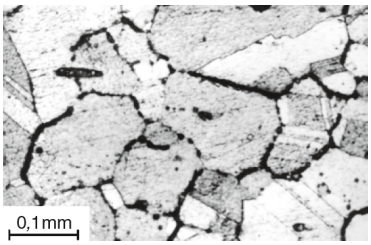

(b) *Intercrystalline cracks as a consequence of hydrogen embrittlement in an oxygen-bearing copper structure [5]*

Figure 2.8: *Embrittlement phenomena in copper materials*

Both discussed embrittlement phenomena can be avoided using phosphorusdeoxidised, and thus oxygen-free copper grades. A residual, not bounded to the oxygen amount of phosphorus bewares the material from oxygen absorption during welding process. Due to the strong negative impact of phosphorus on the electrical conductivity (Figure 2.2), such materials are not used for electro-technical purpose but are common in apparatus and heat exchangers engineering thanks to their good weldability.

Thermal expansion

As a consequence of the high coefficient of thermal expansion in combination with the required preheating and the high heat input in most welding processes, considerable distortion of the weldments can be expected. With application of welding processes of high power densities like electron beam welding, the preheating is unnecessary and the heat input can be reduced leading to minimal warping and distortion phenomena.

Gas absorption

At temperatures above ~ 600 K, copper tends to absorption of atmospheric gases. This may have a negative impact on mechanical properties like the embrittlement phenomena already explained. Such influences can be avoided with the help of shielding gas, welding in an atmosphere of inert gases or welding in vacuum.

Viscosity of the melt pool

In case of unalloyed coppers, the weldability is aggravated by the fact, that pure copper has a melting point, no melting range. The change from solid to liquid occurs immediately and the emerging melt is highly inviscid which makes the process susceptible to run outs. For this reason, without exception, alloys are used as filler metals in order to create a melting range, hence a more viscid molten pool and a better moldability of the melt.

2.1.4 Electron beam welding of heavy-section copper

The electron beam welding of heavy-section copper materials like investigated in [1], has its reasons for existence in certain fields of application.

The high thermal conductivity of copper makes it the ideal material for processes requiring a large amount of heat flux. Water-cooled moulds of continuous casting processes are therefore usually made of thick-walled copper to achieve a good cooling performance of the cast material. [29]

The excellent corrosion resistance of copper makes it a suitable material for the purpose of high-level waste disposal like nuclear waste. Hence, the majority of publications about EBW of thick copper is dedicated to this very application [30–36].

In contrast to [1] the weldments in these works are unexceptional designed as partially penetrating welds. Either joint shapes with centring lips [30–32, 35], joint shapes with backing plates [33, 36] or both [34] are used.

In [30], [31] and [33], horizontal EB welding of copper lids were described. The joints in [30] and [31] are designed with a so-called "fronting bar" shown in Figure 2.9 to prevent the molten material from pouring out during the weld process.

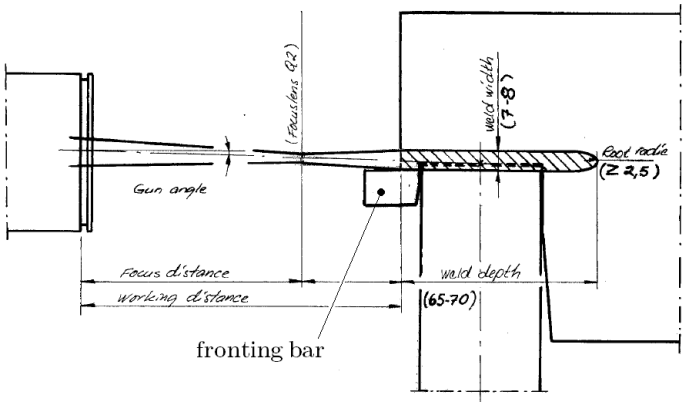

Figure 2.9: *Fronting bar in horizontal electron beam welds; adapted from [31]*

In [31] and [32], the root shape was found to be essential in root defect formation. Sharp roots are susceptible to root defects, a fusion zone like depicted in Figure 2.10 should be intended.

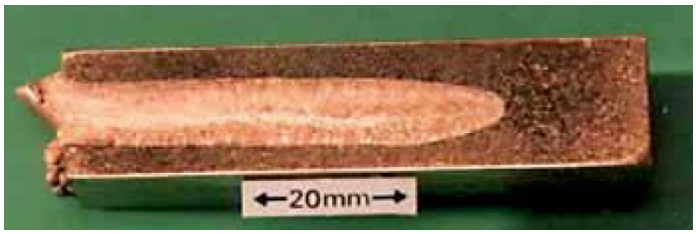

Figure 2.10: *Intended shape of fusion zone to avoid root defects in EBW of heavy-section copper [31]*

In [34], Cu-OF, Cu-OFP and Cu-DHP grades were investigated. The weldability of Cu-OF and Cu-OFP turned out to be good while the higher oxygen content in Cu-DHP led to excessive porosity formation. Excessive run outs and root defects occurred in horizontal welding position. To gain defect free roots and avoid run outs, a backing bar is recommended. Narrow weld profiles when welding at high speeds led to root defects or even lack of fusion. Vacuum pressure alteration between 10^{-4} mbar $\ldots$ 10^{-2} mbar had a minor impact on the quality of the welds.

In [35], investigations on EB weldings carried out in flat position is presented. Proper usage of beam deflection was found to be a key option in reducing porosity formation and root discontinuities.

In [36], defects like large cavities, erratic metal overflow and undercutting turned up when welding with high beam power in combination with high welding speeds. Welding with lower beam power and welding speed lead to smooth and defect free weldings except low levels of gas porosity.

2.2 Electron beam welding

The following section will give a general overview of the electron beam welding (EBW) process and its characteristics in its application. Furthermore the deep penetration welding effect and the interaction between the electron beam and the base material will be described in greater detail. If not denoted otherwise, the information given in this chapter is obtained from [37].

The EBW process is a fusion welding process, where a beam of accelerated and focused electrons serves as the energy source for welding metal materials. The process is characterised by a very high power density of about $10^7\,\mathrm{W/cm^2}$ at the focus point of the beam. Depending on the beam parameters, the power density can even reach up to $10^8\,\mathrm{W/cm^2}$ [38].

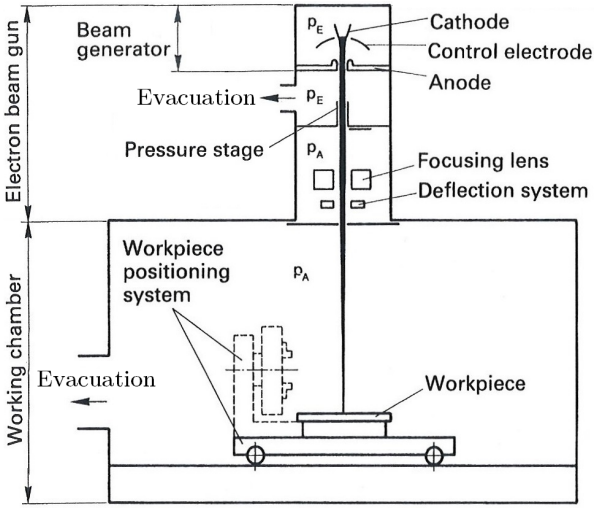

Figure 2.11: *Schematic setup of a typical EBW machine: Electron beam gun with beam generator, focusing lens and deflection system to generate the beam; evacuated working chamber with the workpiece; pressure in the electron beam gun* $p_E = 10^{-4} \ldots 10^{-9}\,\mathrm{mbar}$*; working pressure* $p_E = 10^{-2} \ldots < 10^{-4}\,\mathrm{mbar}$*; adapted from [37]*

A typical EBW machine consists of an electron beam gun to generate the beam and a working chamber, where the workpiece can be placed. With few exceptions, EBW is carried out in vacuum. Thus no shielding gas is required and weld seams with very high purities can be achieved, even with reactive materials such as titanium or zirconium.

One of the biggest benefits of EBW is the deep penetration welding effect, also known as keyhole welding effect. This effect leads to a very narrow seam and heat affected zone with achievable aspect ratios[3] of 1:10 to 1:50. Thus the heat input, compared to other fusion welding processes, is very low, resulting in little distortion of the welded material.

The beam powers range from much less than 1 kW up to 300 kW, which provides the possibility of welding steel with thicknesses of < 0.5 mm up to 300 mm. Regardless of the material thickness, due to the keyhole effect, edge preparation is not necessary. Due to the fact, that butt welds need very few machining for preparation, they are the preferred weld types. Usually EBW works without the need of filler metal, unless

[3] Ratio of seam width to depth = $\frac{W}{H}$

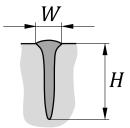

it is necessary to affect the metallurgical properties of the seam or needed to enable dissimilar material combinations.

With EBW, a great number of electric conductive materials can be welded. Besides structural steels, alloy steels and non-ferrous metals, even highly reactive metals can be joined successfully, since the process is executed in a vacuum chamber.

All electrical and mechanical welding parameters are computer-monitored and -controlled, hence EBW is highly reproducible process leading to higly reproducible weld qualities.

The electron beam offers the possibility of inertia free beam deflection, thus numerous options like static beam deflection, beam oscillation (Figure 2.17), beam modulation (deflection and adaption of e.g. beam current) and multi-beam technologies (e.g. multi-pass welding).

2.2.1 Electron beam generation and beam shaping

After a short description of how the beam is generated, the focusing and deflection of the electron beam shall be explained.

Beam generation

As a part of the electron beam gun, the beam generator consists of the cathode, the control electrode and the anode (Figure 2.11). To put it simply, the cathode serves as the source of free electrons. Considering the incredibly low electron rest mass of 9.1×10^{-31} kg and an acceleration to velocities of about one third of the speed of light, one barely can imagine, how many electrons are needed to weld metal materials. The purpose of the cathode is to provide these electrons. The outer electrons of metal atoms can move freely within the crystal lattice of the metal material. But yet they are unable to get away from the surface of the material. To overcome this potential barrier, the cathode is heated to a high temperature. As this increases the energy of the electrons, they can escape from the surface of the metal. These free electrons are arranged around the cathode, forming an electron cloud.

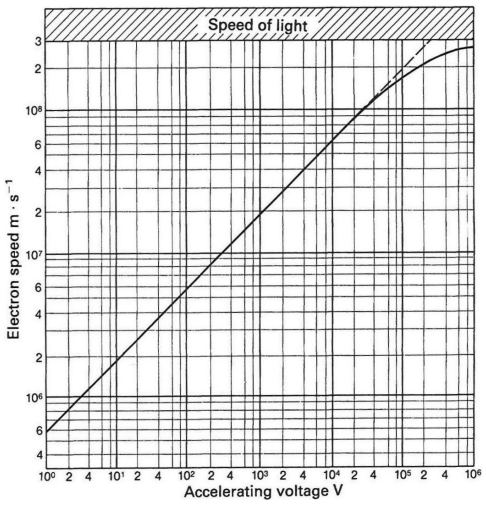

Figure 2.12: *Relationship between accelerating voltage and electron speed [37]*

To accelerate the electrons and thereby give them the required kinetic energy to weld metal materials, the anode comes into action. According to COULOMBS law, when the cathode and the anode get applied to high voltage, the positive anode is

able to attract the negatively charged electrons. Depending on the voltage level, the electrons accelerate to gain the required amount of energy to weld metal. With a typical accelerating voltage for EBW of 150 kV, electrons can reach a speed of 2×10^8 m/s, which is about two thirds the speed of light c. With the formula

$$E_{kin} = \frac{m_e \cdot v_e^2}{2} = \frac{m_{e0} \cdot v_e^2}{2} \cdot \frac{1}{\sqrt{1 - v_e^2/c^2}} = e \cdot U_A$$

where m_e is the relative mass of an electron with the charge e, accelerated to the velocity v_e with the acceleration voltage U_A, the kinetic energy E_{kin} can be calculated [39]. At this velocity relativistic effects become noticeable, that an increase of about 35 % of the relative mass is supplemented to the term $m_{e0} \cdot v_e^2/2$, with m_{e0} as the electron rest mass.

A cathode and an anode can be the simplest kind of a beam generator, called a "diode" system. With this system, the beam current can only be controlled by differing the acceleration voltage or the cathodes temperature. This considerable disadvantage can be avoided by adding a control electrode to obtain a "triode" system. The control electrode, also known as WEHNELT CYLINDER is at cathode potential but has a higher negative voltage level overlaid on it. Depending on the level of control voltage U_C, the control electrode is capable to repel the electrons back towards the cathode, in defiance of the applied accelerating voltage U_A between cathode and anode. The effective emitting surface of the cathode decreases and so does the beam current I_B. At a sufficient high level of U_C, the beam current can be totally blocked.

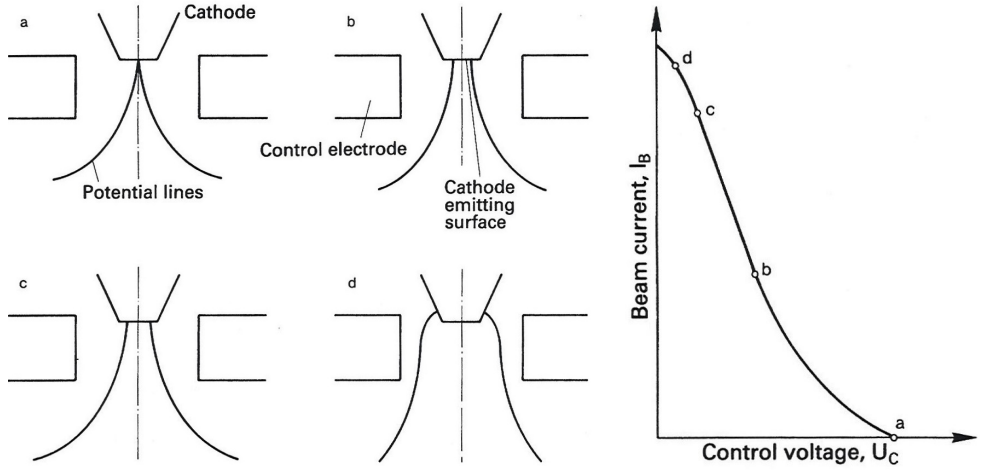

Figure 2.14: *Controlling the beam current I_B by altering control voltage U_C: a) Blocking the beam current; b) Low beam current; c) High beam current; d) Distortion of the beam because of inadequate control voltage; adapted from [37]*

In order to prevent the cathode, which is heated to temperatures of about 2750 °C, from damage by oxidation and to avoid ionisation of the air between the cathode, the control electrode and the anode, the beam generator needs to be evacuated. The maximum pressure allowed in the beam generator is about $p_E = 10^{-4}$ mbar. In some cases ultra high vacuum of $p_E = 10^{-9}$ mbar is necessary within the beam generator system [38].

Beam focusing

Using the LORENTZ FORCE LAW $\vec{F} = -e(\vec{E} + \vec{v} \times \vec{B})$, the electromagnetic lens can affect the flight paths of the electrons and focus the beam to a small spot [40]. An electron with the charge e moving with the velocity $\vec{v}$ in presence of an electric field with field strength $\vec{E}$ and a magnetic field $\vec{B}$ experiences a force $\vec{F}$ perpendicular to $\vec{v}$ and $\vec{B}$ [41]. Like shown in Figure 2.15, the divergent beam passes an annular coil, where the magnetic field influences the electron paths without effecting their speed. The aim is to concentrate the beam to a single focal point with typical diameters from about 0.1 mm to 1 mm, depending on the beam power and the focal distance. This enables the high power density necessary for welding metal materials with thicknesses of several centimetres. The focal distance mainly depends on the acceleration voltage U_A and the lens current I_L. Usually the focal distance is varied by changing the latter.

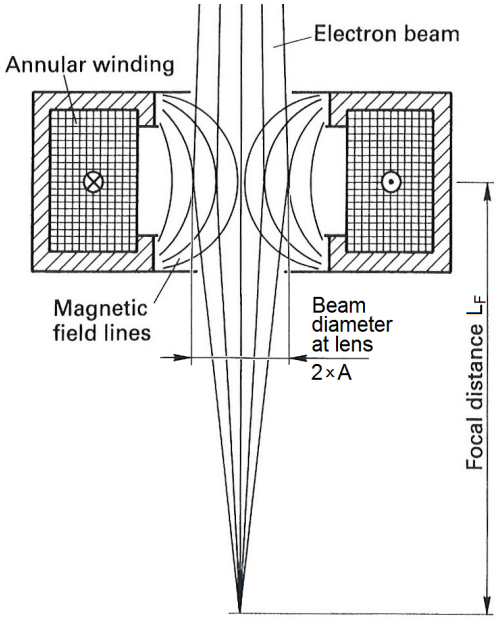

Figure 2.15: *Electromagnetic lens using the* LORENTZ FORCE *to focus the electron beam; adapted from [37]*

Beam deflection

After the electromagnetic lens, the beam passes the deflection system. Four coils, arranged along the x- and y-axis around the beam, are wound on either a number of cores, or a single core (Figure 2.16). When a direct current is applied, the beam can be statically moved in the directions of these axes or any angle between. By using a function generator and applying alternating current it is possible to make the beam oscillate through any required path. Since the beam is practically inertia free, beam deflection is feasible without any limit in frequency or oscillation shape.

2.2.2 Welding parameters

Following lines will give a short overview of the most important welding parameters and their influence on the outcome of the EBW process.

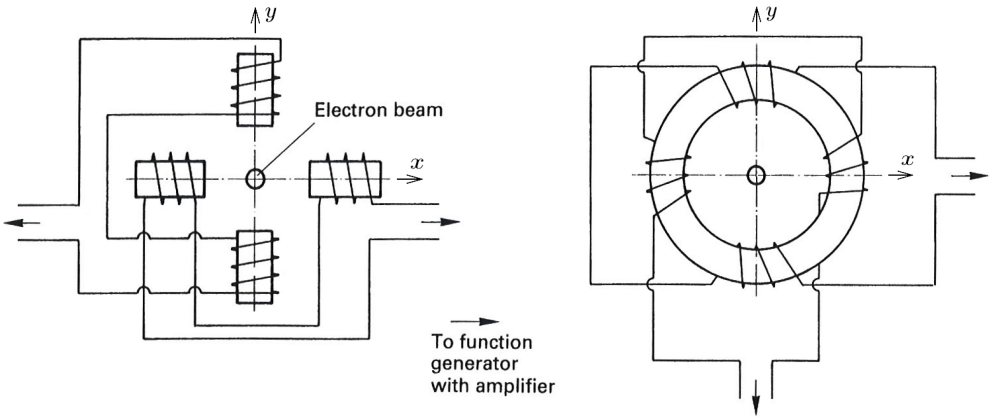

(a) *Main field coils* **(b)** *Subsidiary field coils*

Figure 2.16: *Beam deflection system; adapted from [37]*

Acceleration voltage

The acceleration voltage U_A is not only influencing the speed of the electrons. Together with the beam current I_B, the beam power

$$P = U_A \times I_B \tag{2.3}$$

is defined. Furthermore, U_A has an effect on the beam emittance ε, thus the achievable focal diameter of the beam. With increasing acceleration voltage ε decreases, which leads to a smaller diameter in the focus of the beam (see also equation (4.1) on page 48). Hence, welds made with a certain beam power P tend to be narrower with higher acceleration voltage.

Beam current

The impinging beam current I_B is the sum of the workpiece current I_W and the transmitting current I_T. During the welding process in an EBW machine, the workpiece is part of a closed electric circuit, allowing an electrical current I_W to flow through the workpiece. The transmitting current is the part of I_B passing through the keyhole in case of a full penetration welding of e.g. a butt weld. I_T keeps the keyhole open in the root part of the workpiece and affects the shape of the root cap.

When welding a butt weld, the EB should pass the workpiece with a certain residual beam power (transmitting power P_T) to form a proper root. For example when a bead on plate weld made with a certain parameter set achieved the penetration depth H, a full penetration butt weld with the same parameters ensuring a proper root forming can be done at a workpiece with the thickness $t \sim 0.8 \times H$.

If the beam current is too low, a convex weld crown is emerging while the fusion zone in the root is very narrow or the workpiece is even not fully through-welded.

If the beam current is too high, the weld crown is concave with either a convex root cap, droplets along the root or even drop outs of molten metal leading to a concave root cap.

Welding speed

Together with P, the welding speed v determines the energy input per unit length E:

$$E = \frac{P}{v} \tag{2.4}$$

The energy input per unit length decreases with increasing welding speed. Both, beam power and welding speed are the main factors determining the achieveable penetration depth H. Furthermore, the welding speed affects dynamic processes in the keyhole like solidifaction and cooling.

At high welding speeds the molten envelope surrounding the keyhole cavity can decrease in such a way, that the material transport around the keyhole is interfered and drop-like formations on the crown and/or the root of the weld can occur.

When processing with a very low welding speed, the weld bath becomes too wide and the keyhole is unable to penetrate deeper in the weld pool. In other words, for a certain material, a certain depth of fusion zone exists, which cannot be exceeded by reducing the weld speed at a given power.

Focal position

The focal position f_P is defined as the distance between the upper workpiece surface and the location of the focal point, the point where the highest power density of the electron beam is achieved. At positive counted focal positions (over-focused), the focal point is above the workpiece and at negative positions (under-focused), the beam focus is inside or even underneath the workpiece. This influences the width of the seam, the shape of the fusion zone, the penetration depth, the melt flow, etc.

A normal focal position $f_P = 0\,\mathrm{mm}$ is not always the optimum position. Depending on the workpiece geometry, the gap, the material, the welding parameters, etc., welding with an over- or under-focused beam is necessary in order to produce as fewest defects as possible.

Beam oscillation

With dynamic periodic beam deflection or beam oscillation it is possible to affect the dynamics of the molten zone.

With suitable oscillation figures and proper settings of amplitude and frequency, good conditions for a defect free fusion and solidification can be created as well as the forming of the root and/or the crown of the weld can be affected beneficially. Generally, beam oscillation increases the size of the fusion zone and facilitate gas pores to rise in the melt pool and escape from the fusion zone. However, except for oscillation in the direction of welding trajectory (x-oscillation), the penetration depth tends to decrease compared to welding with static beam.

Beam oscillating with small amplitudes and high frequencies increase the size of the keyhole and prevent the molten envelope from collapsing. According to [37], for steel materials and at deflection frequencies $f > 25\,\mathrm{Hz}$, the electron beam moves within the keyhole, hence expands it. When welding with high amplitudes and small frequencies $f < 25\,\mathrm{Hz}$, the electron beam moves the keyhole, leading to a “stirring” effect in the molten pool.

Working pressure

To avoid collisions of the accelerated electrons with atoms or molecules of atmospheric gases, the working chamber is evacuated to the working pressure p_A. The light elec-

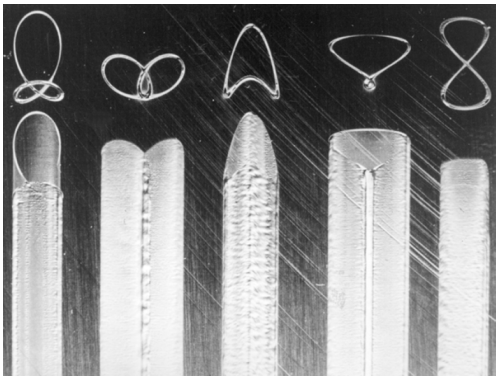

Figure 2.17: *Examples of different beam oscillation figures [42]*

trons with a mass of 9.1×10^{-31} kg get deflected and scattered when colliding with the heavy gas molecules. This leads to a broadening of the beam (Figure 2.19) and therefore a decrease of the power density. A decrease of the achievable penetration depth owing to scattering, begins to get noticed at working pressures of $p_A > 10^{-2}$ mbar. This value can be seen as the maximum value which can be tolerated in the working chamber. Nevertheless, working pressures of $p_A < 10^{-4}$ mbar or less can be necessary, depending on the gas sensitivity of the welded material.

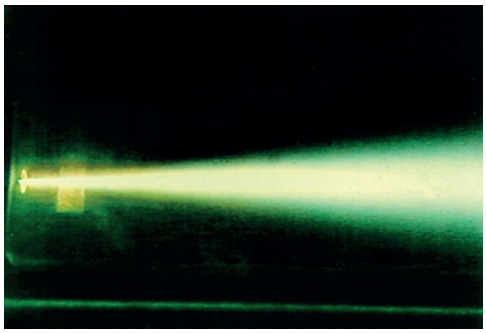

(a) *Noticeable beam expansion in an ambience with* 500 mbar *residual gas*

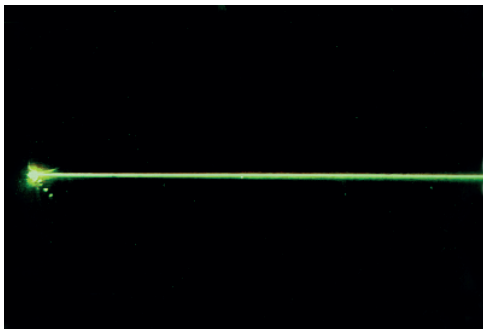

(b) *In an ambience with* 50 mbar *hardly any widening of the beam can be recognised*

Figure 2.19: *Beam expansion of an electron beam due to multiple scattering of electrons colliding with gas molecules [40]*

2.2.3 Electron behaviour in penetrating metal [43]

After impinging on the surface, the electrons generate heat by converting their kinetic energy into thermal energy. Numerous elastic and inelastic collisions of the incoming electrons with the nuclei and the electrons of the absorber happen.

Electrons impinging on a target are either absorbed, backscattered because of large-angle deflections or transmitted to deeper layers. These fractions are denoted with the coefficients η_A, η_B and η_T, fulfilling equation (2.5).

$$\eta_A + \eta_B + \eta_T = 1 \tag{2.5}$$

In the event of (nearly) elastic nuclear scattering, electrons can undergo large-angle deflections from their original trajectories and lose small amounts of their kinetic energy by emitting photons. Most of the kinetic energy from the electrons is consumed

due to inelastic collisions with atomic electrons of the target material. Based on scattering events, the energy distribution broadens and a bulb shaped electron-material interaction volume, like schematically depicted in Figure 2.20a, is developing.

Numerous collisions happen until the electrons kinetic energy is given over to the absorber material. At a certian depth R, depending on the material and the energy of the impinging electrons, nearly all of the kinetic energy is transformed to heat.

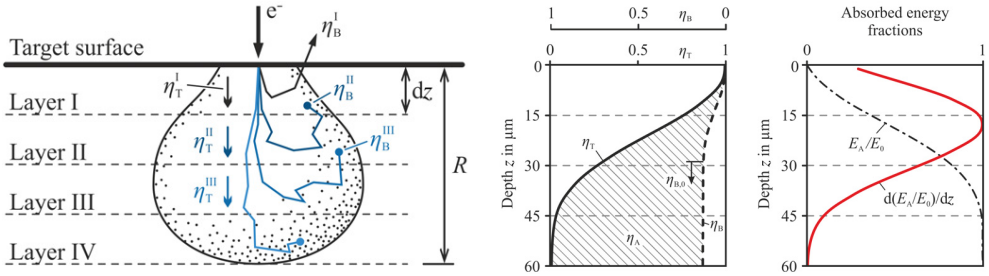

(a) *Typical energy dissipation for single electrons impingement*

(b) *Absorbed energy fractions as a function of depth z*

(c) *Normalised energy distribution*

Figure 2.20: *Scheme of a typical energy dissipation volume of single electrons interacting with the material* (a)*; Energy fractions as a function of the depth z* (b) *with fractions of electrons transmitted through η_T, backscattered from η_B and absorbed in η_A an infinitesimal layer with thickness dz and energy distribution normalised to their maximum values* (c)*; Examples for target material aluminium irridiated by* 100 keV *electrons at normal incidence [43]*

2.2.4 Electron backscattering

Since the model of LaserCAD takes multiple reflections of electrons inside the keyhole into account (see Section 4.1), the following lines will give some further information about backscattering of accelerated electrons based on [41], [43] and [44].

The backscattering effect causes emission of electrons in the processing area of the electron beam with an energy spectrum reaching up to the energy of the impinging electrons. The fraction of the backscattered electrons, their energy spectrum and their directional distribution are primarily determined by the atomic number of the target material and the incident angle of the electrons. In contrast to the thermal electron emission, the backscattering effect is independent of the temperature and, unlike the emission of secondary electrons, independent of thin surface layers.

Figure 2.21a shows the dependence between the backscattering coefficient η_B and the atomic number of the target material with an incident angle perpendicular to the surface. In Figure 2.21b, the influence of the energy, hence the acceleration voltage ($E_0 = e \cdot U_A$) on η_B is presented. The graph reveals, that, to a great extend, the back scattering does not depend on the energy of the impinging beam. Figure 2.21c shows the backscattering coefficient versus the incidence angle α measured between the beam axis and the surface normal of the target. In the case of a perpendicular incidence ($\alpha = 0\,°$), η_B is on its lowest level and increases with increasing α.

The intensity distribution of the backscattered electrons is club-shaped with an intensity maximum, which is approximately fulfilling the optical law of reflexion: entrance angle equal exit angle (Figure 2.22).

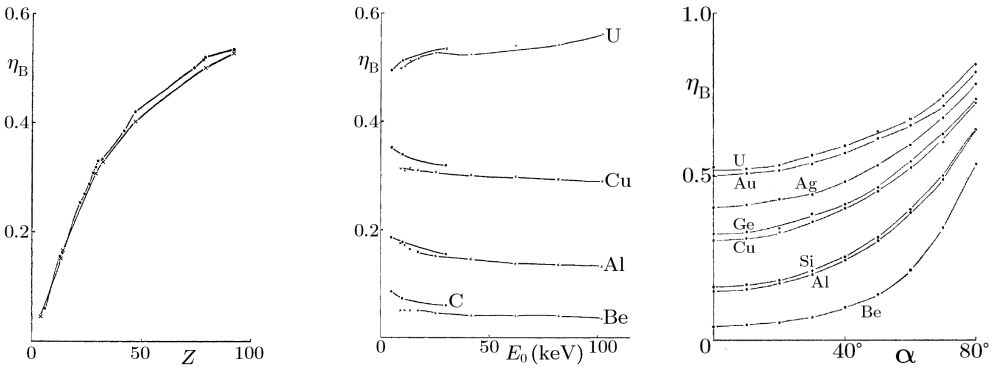

(a) *Backscattering coefficient η_B at perpendicular incidence as a function of the atomic number Z at a beam energy of* 30 kV (·) *and* 25 kV (×)

(b) *Backscattering coefficient η_B at perpendicular incidence as a function of the beam energy E_0*

(c) *Backscattering coefficient η_B at* 25 kV *as a function of the beam incidence angle α*

Figure 2.21: *Backscattering coefficient η_B versus atomic number Z* (a)*, beam energy* (b) *and incident angle α* (c)*; adapted from [44]*

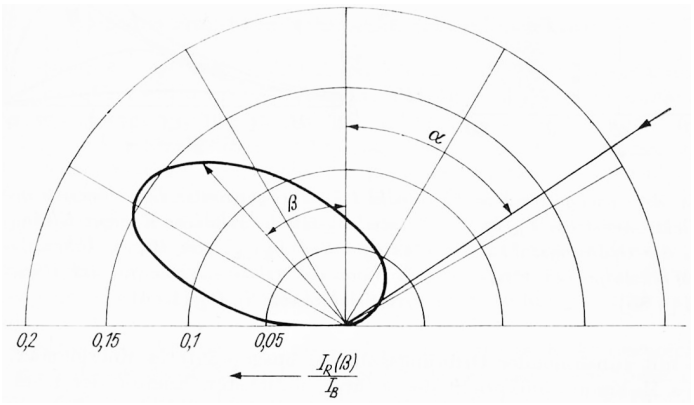

Figure 2.22: *Angular distribution of the relative backscattered electron current $I_R(\beta)$ at inclined beam impact for aluminium ($Z = 13$) with a* 50 keV *beam at $\alpha = 55°$ [41]*

Owing to backscattering, the energy loss during the process is considerable (Figure 2.23a). For steel ($Z = 26$) ~ 24 %, for copper ($Z = 29$) ~ 26 %. These are values for a beam impinging perpendicular to the surface ($\alpha = 0°$) on a flat area. In the case of deep penetration welding (Figure 2.23b), the beam penetrates the cavity and electrons are impinging on the cavity walls. Very few of the backscattered electrons find their way out of the keyhole. The deeper the keyhole, the greater the impact of this effect. The majority of the electrons is "trapped" inside and, after reflection, impinges at another part of the cavity. Hence, even after (multiple) reflections, the electrons are still able to generate process heat. According to [37], the efficiency of the energy conversion at EBW for steel is ~ 0.60 when starting the welding process and ~ 0.90 . . . 0.95 during welding.

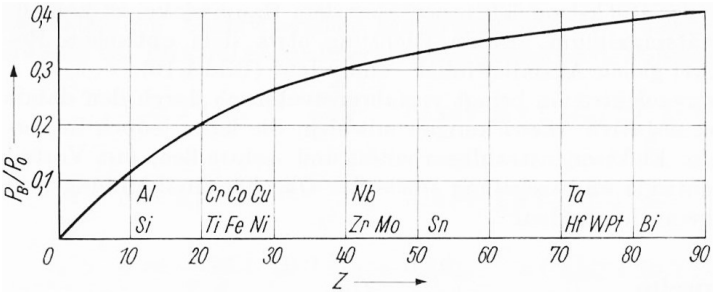

(a) *Ratio of backscattered power P_B and impinging power P_0 versus atomic number Z for perpendicular beam incidence $\alpha = 0\,^\circ$*

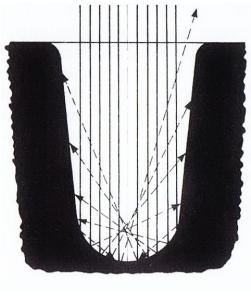

(b) *Reduction of the energy loss when a deep cavity is formed*

Figure 2.23: *Ratio of backscattered power P_B and impinging power P_0 versus atomic number Z and the reduction of the losses (P_B) in case of deep penetration welding; adapted from [41]*

2.2.5 Deep penetration welding

When welding with an electric arc or an autogenous gas flame, the thermal energy is transfered from the outside, while in EBW the "cold" eletron beam is generated to heat inside the material. An electron accelerated with $U_A = 150\,\mathrm{kV}$ is able to penetrate steel up to a depth of $\sim 0.06\,\mathrm{mm}$. Hence, the difference to e.g. arc welding seems negligibly. Nevertheless, with EBW much smaller aspect ratios ($= \frac{\text{width of seam}}{\text{depth of seam}}$), and therefore much thicker materials are weldable with a single pass.

Table 2.7: *Power densities of different welding processes*

Welding process		Energy density		Source
Oxyfuel welding	(OFW)	$\sim 10^3$	$\mathrm{W/cm^2}$	[45]
Shielded metal arc welding	(SMAW)	$10^4 \ldots 10^5$	$\mathrm{W/cm^2}$	[3]
Gas metal arc welding	(GMAW)	$10^5 \ldots 10^6$	$\mathrm{W/cm^2}$	[3]
Submerged-arc welding	(SAW)	$10^5 \ldots 10^6$	$\mathrm{W/cm^2}$	[3]
Electron beam welding	(EBW)	$10^7 \ldots 10^8$	$\mathrm{W/cm^2}$	[3]
Laser beam welding	(LBW)	$10^8 \ldots 10^9$	$\mathrm{W/cm^2}$	[3]

The decisive factor is the difference of the power density. Table 2.7 gives an overview of the power densities of certain welding processes. With a gas flame or an electric arc, the heat to melt the material in the fusion zone is provided by conduction. At power densities $> 10^5\,\mathrm{W/cm^2}$ the melting of the material starts initially without significantly heating adjacent regions by conduction (Figure 2.24a). The melting is further heated, begins to vaporise and the vapour is further superheated. The reaction force of the expandig vapour presses the molten material downwards and sideways, while the vapour is released upwards (Figure 2.24b). A depression in the melt is formed, allowing the beam to impinge on deeper material layers, heating, melting and vaporising the "fresh" material likewise. The depression grows and a deep cavity filled with superheated vapour with an envelope of molten material, also known as keyhole, is formed (Figure 2.24c).

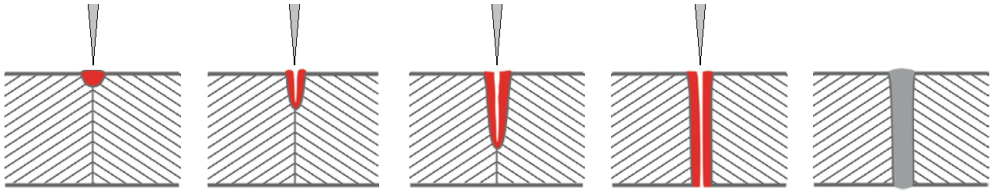

(a) *Melting* **(b)** *Depression* **(c)** *Growth* **(d)** *Penetration* **(e)** *Finish*

Figure 2.24: *Scheme of the keyhole forming process; The beam impinges and the material melts initially* (a)*; The pressure of further heated and vaporised material forms a depression* (b)*; The depression grows by further melting and vaporising of deeper layers* (c)*; The keyhole reaches the bottom part of the workpiece* (d)*; The beam is turned off, the vapour pressure declines and the cavity fills with molten metal solidifying to a weld seam* (e)*; adapted from [40]*

During welding the keyhole moves with welding speed v along the specimen as depicted in Figure 2.25. The welding direction is defined as x-direction. While the beam moves foreward, the material on the front wall of the keyhole is continuosly heated, molten and vaporised. The molten material in front of the keyhole flows around against welding direction and an elongated weld bath is formed.

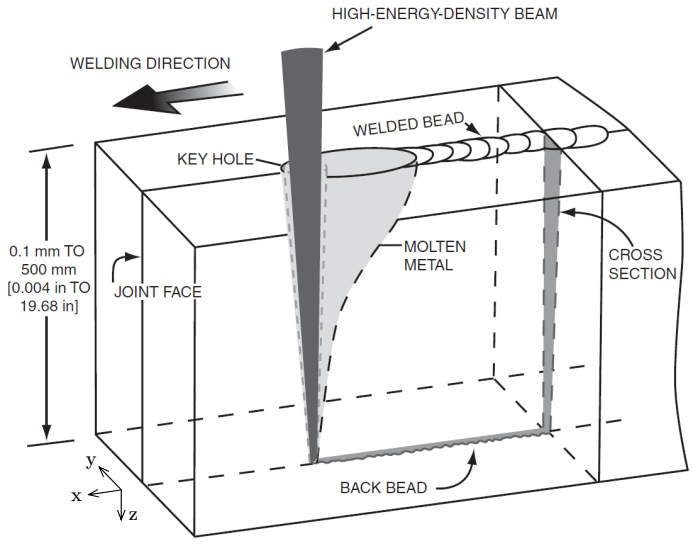

Figure 2.25: *Scheme of a keyhole welding process with indicated coordinate system; adapted from [42]*

The keyhole is a complex system and in order to ensure a continually open keyhole, various forces need to interact. The major of them are schematically depicted in Figure 2.26. Inside the keyhole the pressure of the vaporised material F_1 acts against the forces resulting from surface tension F_2 and the hydrostatic pressure of the molten envelope F_3. The weight of the molten material F_5 is supported by the frictional forces the flowing vapour is applying to the inner wall of the cavity F_4.

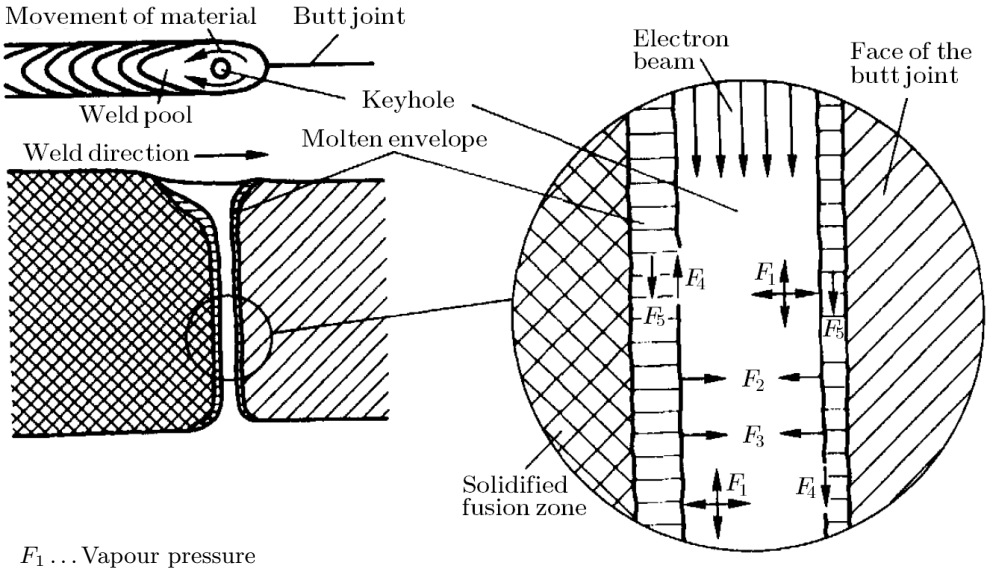

F_1 ... Vapour pressure
F_2 ... Laplace pressure
F_3 ... Hydrostatic pressure
F_4 ... Frictional force from escaping metal vapour
F_5 ... Gravitational force

Figure 2.26: *Scheme of major forces acting in the keyhole and molten envelope during the deep penetration welding process; adapted from [37]*

Chapter 3

Experimental data

The following lines will give an overview of the available experimental data for this work. Besides experiments with copper materials, electron beam welds of stainless steel were made as a comparison. All listed experiments have been realised with the EBW-machine with model number EBG 45-150 K14 from PRO-BEAM at the INSTITUTE OF MATERIALS SCIENCE AND WELDING at TU Graz.

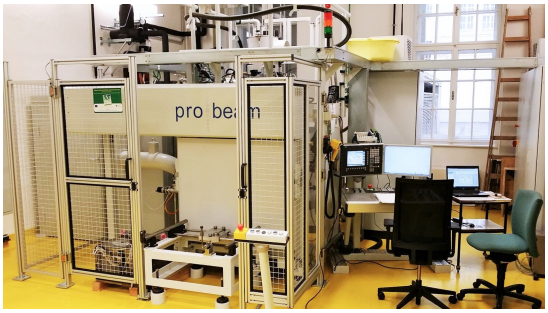

Figure 3.1: *Electron beam welding machine at TU Graz; Universal-chamber machine EBG 45-150 K14 from pro-beam AG & Co. KGaA*

Electron beam gun parameters		
$U_{A;max}$	150	kV
I_B	0.1 . . . 300	mA
P_{max}	45	kW

3.1 Experiments with Cu-DHP

After giving a brief overview of available experimental data from [1], the experiments which were carried out for this work, will be presented.

3.1.1 Oscillating figure weldings with and without filler metals

In [1], many experiments were done in order to minimise root defects like pores and craters. The majority of them were carried out with Cu-DHP. Table 3.1 gives a compendium of weldings made with Cu-DHP as base material. It represents all weldings with metallographic data of at least one section cut. As can be noticed, all weldings were executed with oscillating beam figures. Most of the welds are bead on plate welds, some are butt welds. In some of the butt welds, filler material with a sheet of CuSn6 between the two joint faces was used. Figure 3.2 shows an example of bead on plate welds with noticeable root craters.

Table 3.1: *Excerpt of experimental welding parameters and available metallography data for Cu-DHP from [1]; Acceleration voltage U_A = 150 kV*

ID	Filler	Metallography	I_B mA	P kW	v mm/s	f_P mm	Figure	dx mm	dy mm	f Hz	Note
SF-D1-Naht1		SR, N	120	18	5	-20	○	0.5	0.5	1000	
SF-D1-Naht2			120	18	10	-20	○	0.5	0.5	1000	
SF-D1-Naht3			140	21	5	-20	○	0.5	0.5	1000	
SF-D1-Naht4			140	21	10	-20	○	0.5	0.5	1000	
SF-D2-Naht1		SR, N, L	180	27	10	-10	○	0.5	0.5	1000	
SF-D2-Naht2			180	27	10	-20	○	0.5	0.5	1000	
SF-D2-Naht3			180	27	10	-10	"Qualle"	0.5	0.5	1000	
SF-D2-Naht4			180	27	10	-20	"Qualle"	0.5	0.5	1000	
SF-D3-Naht1		SR, N	180	18	5	-20	○	0.5	0.5	1000	
SF-D3-Naht2			180	18	10	-20	○	0.5	0.5	1000	
SF-D3-Naht3			210	21	5	-20	○	0.5	0.5	1000	
SF-D3-Naht4			210	21	10	-20	○	0.5	0.5	1000	
SF-D7-Naht1		SR, N, L	140	21	10	-10	∩	1	1	20	
SF-D7-Naht2			140	21	10	-10	∩	1	1	1000	
SF-D7-Naht3			140	21	10	-10	△	1	1	20	
SF-D7-Naht4			140	21	10	-10	△	1	1	1000	
SF-V1	CuSn6	SR, N, L	140	21	10	-10	△	0	1	1000	
SF-V2		SR, N, L	140	21	10	-10	△	0	1	1000	
SF-V3	CuSn6	SR, N, L	140	21	10	-10	△	0	1	1000	
SF-V4	CuSn6	SR, N, L	140	21	10	-10	△	0	1	1000	first pass
			120	18	5	-10	△	0	1	1000	second pass
SF-V17	CuSn6	SR, N	120	18	5-9	-15	△	0	1.5	21	
SF-V20	CuSn6	SR, N, L	120	18	5-9	-15	△	0	1.5	21	
SF-V21	CuSn6	SR, N	120	18	5-9	-15	△	0	1.5	1000	
SF-V22		SR, N	120	18	5-9	-15	△	0	1.5	21	
SF-V23	CuSn6	SR, N	120	18	5-9	-15	△	0	1.5	21	
SF-V24	CuSn6	SR, N	130	19.5	5-9	-15	△	0	1.5	21	
SF-V25	CuSn6	SR, N	120	18	5-9	-15	△	0	1.5	21	
SF-V29	CuSn6	SR, N	100	15	5	-15	△	0	1.5	1000	first pass
			140	0	10	-15	△	0	1	30	second pass
SF-V30		SR, N	100	15	5	-15	△	0	1.5	1000	first pass
			140	0	10	-15	△	0	1	30	second pass

SR . . . . Pictures of upper seam and root
N . . . . . Cross section cut (normal to weld path)
L . . . . . Longitudinal section cut (in the plane of the joint faces)

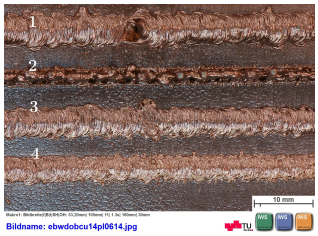

(a) *SF-D7; Upper seam; Naht1. . . Naht4 (top. . . bottom)*

(b) *SF-D7; Root with noticeable defects (root craters); Naht1. . . Naht4 (top. . . bottom)*

(c) *SF-D7; Cross section cut; Naht1. . . Naht4 (left. . . right)*

Figure 3.2: *Example of metallographic data from the experiments made in [1]; Bead on plate welds with full penetration (ID: SF-D7)*

3.1.2 Point figure welds

One restriction of LaserCAD is, that it is not possible to simulate an oscillating beam. Hence, the data shown in [1] cannot be directly related to the simulation results. To get comparable welds for validation, experiments with Cu-DHP without oscillating beam (point figure) were done. The simulation parameters are listed in Table 3.2. The chosen values for U_A and I_B are values, where the beam parameters divergence θ and emittance ε are known, owing to measurements by PRO-BEAM [46] (see Table

4.4 on page 49). For each of these two parameter settings seams with welding speed v of 5, 10 and 20 $^{mm}/_{s}$ were made.

After the EBW process, the specimen was cut at three positions normal to the weld path. At each position, denoted as I, II, and III, the section planes were analysed looking into the welding direction ("←" in Figure 3.3a), that means the run-in part of the specimen (right) was not investigated. All three section cuts were polished and etched with etching solution *Cu-M1* suggested in [47] to detect the fusion zone. Looking at Figure 3.3b, V-shaped seams with slightly concave sides, a sharp root and a maximum penetration depth of ~ 17 mm are recognisable.

Table 3.2: *Welding parameters for bead on plate welds and average penetration depth H, width at surface W_0 and width at half of depth $W_{H/2}$; Material: Cu-DHP; Figure: point (no beam oscillation)*

Seam		1	2	3	4	5	6
U_A	kV	120	120	120	120	120	120
I_B	mA	80	80	80	60	60	60
v	$^{mm}/_{s}$	10	5	20	5	20	10
P	kW	9.60	9.60	9.60	7.20	7.20	7.20
E	$^{kJ}/_{mm}$	0.96	1.92	0.48	1.44	0.36	0.72
H^I	mm	13.10	16.10	13.60	12.80	10.00	10.80
H^{II}	mm	13.30	17.10	13.90	–	–	10.70
H^{III}	mm	13.30	16.80	13.60	13.20	10.20	10.60
H	mm	13.23	16.67	13.70	13.00	10.10	10.70
W_0^I	mm	4.60	5.10	4.20	5.10	4.30	4.30
W_0^{II}	mm	4.20	5.30	4.10	–	–	4.40
W_0^{III}	mm	4.40	5.50	4.30	5.00	4.00	4.30
W_0	mm	4.40	5.30	4.20	5.05	4.15	4.33
$W_{H/2}^I$	mm	1.10	1.20	1.10	1.40	0.95	1.10
$W_{H/2}^{II}$	mm	1.10	1.30	1.20	–	–	1.10
$W_{H/2}^{III}$	mm	1.00	1.30	1.00	1.20	1.10	1.00
$W_{H/2}$	mm	1.07	1.27	1.10	1.30	1.03	1.07

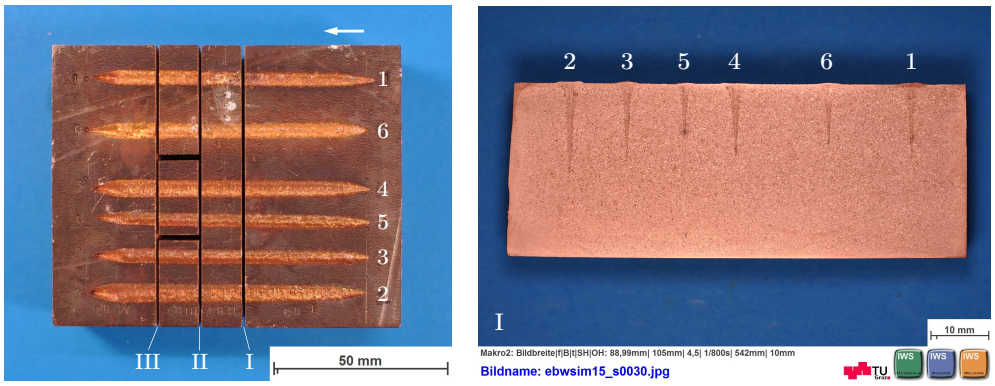

(a) *Cut specimen block for cross section analysis of the section planes I, II and III*

(b) *Cross section cut at section plane I*

Figure 3.3: *Bead on plate welds of Cu-DHP according to parameters from Table 3.2*

In order to record thermal cycles of three different distances from the centre of the welds, three thermocouples (TC) type K (NiCr-Ni, max. ~1100 °C) were placed

Distances		
L_1_1	4.0	mm
L_1_2	7.5	mm
L_1_3	11.0	mm
L_6_1	11.0	mm
L_6_2	7.5	mm
L_6_3	4.0	mm

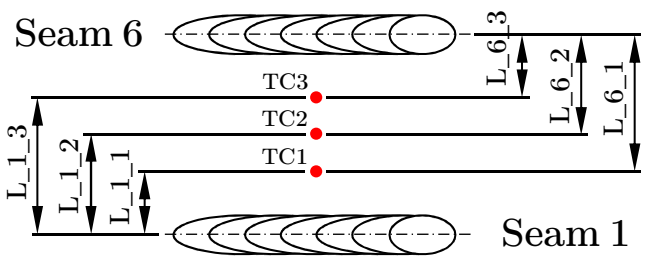

Figure 3.5: *Arrangement of thermocouples and their distance to seam axis for Cu-DHP; The thermocouples were placed on the upper surface (y = 0 mm)*

on the surface between seams with number 1 and 6 according to Figure 3.5. Looking at Figure 3.3a, three white spots between section planes I and II can be recognised, indicating the positions of the thermocouples. Although aluminium foil was used in order to shield the TC wires from scattered electron radiation, artefacts in the measurement signal occurred during the welding period. The middle one of the TCs showed irrational behaviour (TC No. 2; grey lines in Figure 3.4), which cannot only be attributed to a signal offset, since the offset values before and after the welding process are different. Furthermore, the slope of the signal is unreasonable, in relation to the other two signals. Hence, these graphs are not considered for further investigations.

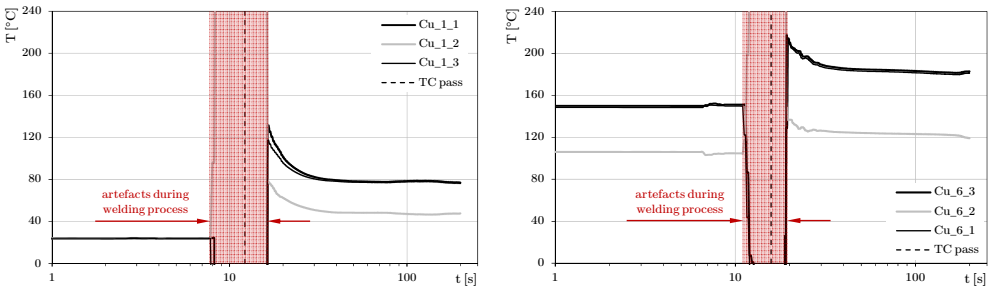

(a) *Thermal cycle of seam number 1*

(b) *Thermal cycle of seam number 6*

Figure 3.4: *Recorded thermal cycles of seams number 1 and 6 with Cu-DHP; Parameters according to Table 3.2*

3.2 Experiments with Cu80 Sn20

Similar to the weldings of Cu-DHP, the bronze material Cu80 Sn20 with 20 % tin was welded with the same parameters (Table 3.3). The weld specimen consists of two milled and stacked casting plates. As investigated in [48], an influence in the fusion zone geometry due to the parting plane can be excluded.

The bell casting bronze material Cu80 Sn20 is a very brittle material. During the cooling of the specimen after the welding process, a cold crack across all seams except No. 2 occured, which can bee recognised on the left of Figure 3.8a. Since the widest gap of the crack can be noticed at seam No. 4, the thermal stress was probably the highest at this area, which leads to the assumption that the crack initiation was a discontinuity in seam No. 4.

In the cast basis material, many pores could be recognised (Figure 3.6). In the same way as mentioned above, the specimen was cut in four parts, sanded, polished, etched and the analysis of the parting planes I, II and III were done at the face viewing in the direction of welding ("←" in Figure 3.8a).

Nail-shaped seams with a wide weld crown, a narrow middle part and a V-shaped bottom part can be recognised in Figure 3.8b. Seam No. 2 reached full penetration, leading to excessive run outs and cavity formation. Pores, especially in the vicinity of the parting plane, exist. Compared to Cu-DHP point figure welds, the tip of the root appears less sharp.

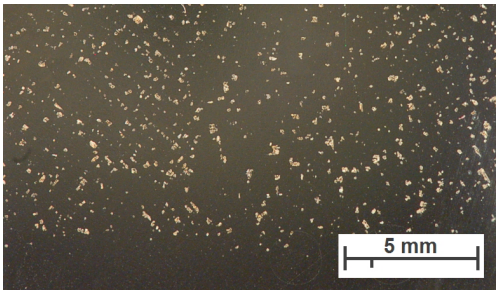

Figure 3.6: *Pores in Cu80 Sn20 casting plate; adapted from [49]*

Table 3.3: *Welding parameters for bead on plate welds and average penetration depth H, width at surface W_0 and width at half of depth $W_{H/2}$;*
Material: Bronze Cu80 Sn20; Figure: point (no beam oscillation)

Seam		1	2	3	4	5	6
U_A	kV	120	120	120	120	120	120
I_B	mA	80	80	80	60	60	60
v	$^{mm}/_{s}$	10	5	20	5	20	10
P	kW	9.60	9.60	9.60	7.20	7.20	7.20
E	$^{kJ}/_{mm}$	0.96	1.92	0.48	1.44	0.36	0.72
H^I	mm	35.80	37.00	27.60	32.00	22.20	31.12
H^{II}	mm	36.20	37.00	28.10	36.70	23.70	32.20
H^{III}	mm	34.70	37.00	29.20	32.10	24.60	28.60
H	mm	35.57	37.00	28.30	33.60	23.50	30.64
W_0^I	mm	6.70	3.40	5.70	10.20	5.90	6.60
W_0^{II}	mm	7.00	3.50	5.50	11.10	6.00	6.80
W_0^{III}	mm	6.60	3.50	5.50	11.30	5.30	6.90
W_0	mm	6.77	3.47	5.57	10.87	5.73	6.77
$W_{H/2}^I$	mm	1.90	2.70	1.70	4.30	1.60	2.10
$W_{H/2}^{II}$	mm	2.50	3.20	2.00	5.11	1.90	2.90
$W_{H/2}^{III}$	mm	2.30	3.50	1.90	4.70	1.80	2.60
$W_{H/2}$	mm	2.23	3.13	1.87	4.70	1.77	2.53

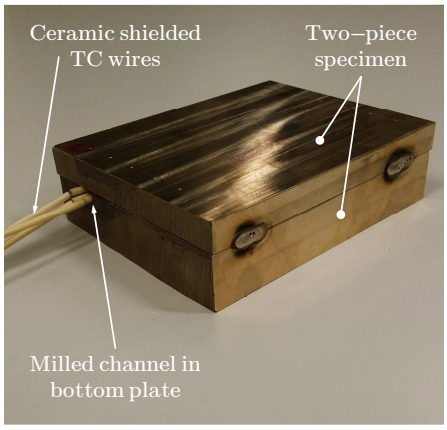

(a) *Two-piece specimen with milled channel for thermocouple application*

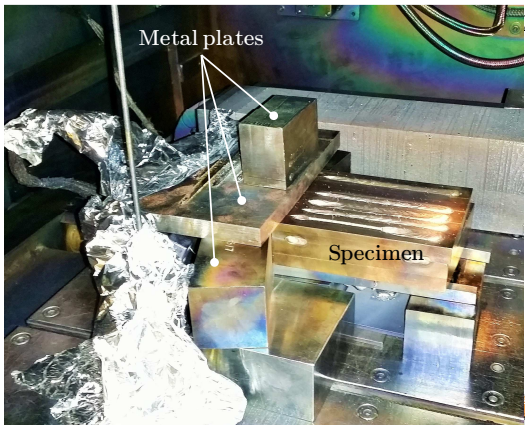

(b) *Shielding of the measuring cables, connections and thermocouple wires with aluminium foil and metal plates*

Figure 3.7: *Preparation of the bronze specimen*

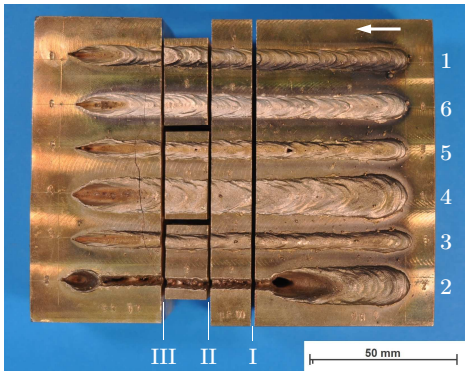

(a) *Cut specimen block for cross section analysis of the section planes I, II and III*

(b) *Cross section cut at section plane III*

Figure 3.8: *Bead on plate welds of bronze Cu80 Sn20 according to parameters from Table 3.3*

Inside the specimen, three thermocouples were placed between seams number 1 and 6 according to Figure 3.9. The TCs were applied on the bottom surface of the upper plate and the ceramic-shielded wires were laid in a milled channel of the bottom plate (Figure 3.7a and dark area in Figure 3.8b). Placed inside the specimen, the thermocouples are well shielded by the surrounding material. The wires outside the specimen and the electrical connections to the measuring lead were shielded with aluminium foil. Additionally, metal plates were stacked around the connections, in order to avoid the influence of scattered radiation on the TC signal (Figure 3.7b). Despite all these measures, artefacts during the welding process occurred (Figure 3.10).

Distances		
L_1_1	4.5	mm
L_1_2	8.0	mm
L_1_3	11.5	mm
L_6_1	11.0	mm
L_6_2	7.5	mm
L_6_3	4.0	mm

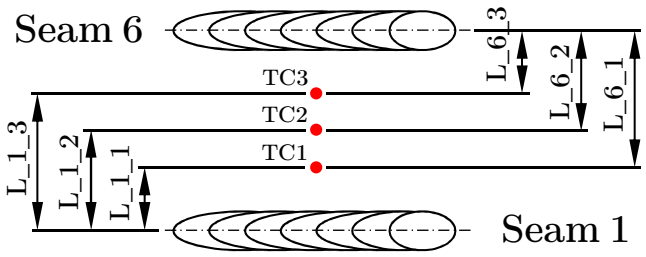

Figure 3.9: *Arrangement of thermocouples and their distance to seam axis for Cu80 Sn20; The thermocouples were placed* 13 mm *below the surface*

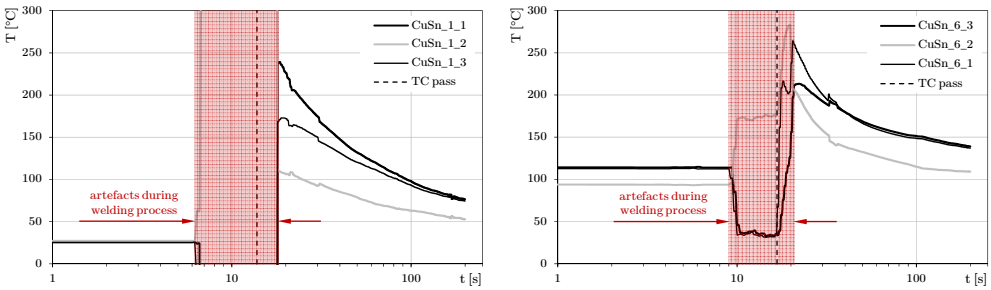

(a) *Thermal cycle of seam number 1*

(b) *Thermal cycle of seam number 6*

Figure 3.10: *Recorded thermal cycles of seams number 1 and 6 with Cu80 Sn20; Parameters according to Table 3.3*

3.3 Experiments with 1.4313

For comparison with copper and bronze, as well as for investigations on the behaviour of LaserCAD's numerical model, EB-weldings with stainless steel 1.4313 were conducted. It is a martensitic nickel–chromium stainless steel with molybdenum addition. The chemical composition and the physical properties of this material are listed in Table 3.4.

For investigations on the influence of the focal point position, a CCD DoE schedule was chosen. The weldings were realised without oscillating beam and the parameters as well as the achieved penetration depth H and the area of the fusion zone S are listed in Table 3.5.

The section cuts are shown in Figure 3.11. In contrast to weldings carried out on Cu-DHP and Cu80 Sn20, most of the seams tend to have an I-shaped cross section. In seams No. 2, 6 and 13 big cavities in the middle and bottom part of the fusion zone can be recognised. Weld No. 1 has a sharp root tip, leading to a small root cavity.

Table 3.4: *Thermophysical properties of 1.4313 [9]*

Attribute		Value		Note
Melting temperature	T_M	1450 ... 1510	°C	
Boiling point temperature	T_B	2861	°C	at atmosph. press. [16]
Heat capacity	c_p	430	J/(kg K)	at 20 °C
Density	ρ	7.70	g/cm³	at 20 °C
Thermal conductivity	λ	25	W/(m K)	at 20 °C
Surface tension †	σ	1.4 ... 1.8	N/m	range of values from [50]
Latent heat of evap.	ΔH_{LG}	6092	kJ/kg	calc. by LaserCAD [2]

Chemical composition

C ≤ 0.05 % Si ≤ 0.70 % Mn ≤ 1.50 % Mo = 0.30 ... 0.70 %
P ≤ 0.04 % S ≤ 0.015 % Cr = 12.0 ... 14.0 % Ni = 3.50 ... 4.50 %

† Total value of surface tension $\sigma = \sigma_L + \sigma_T \cdot T$

Table 3.5: *Welding parameters for bead on plate welds and penetration depth H, width at surface W_0 and width at half of depth $W_{H/2}$ (CCD DoE schedule); Material: 1.4313; Figure: point (no beam oscillation) U_A = 150 kV; v = 10 mm/s*

No.	Beam current I_B mA	Beam power P kW	Focal position f_P mA	Penetration depth H mm	Fusion zone area S mm²	Width at $H/2$ $W_{H/2}$ mm
1	60	9.0	-25	29.8	41.2	4.1
2 †	120	18.0	-25	48.9	82.4	4.5
3	60	9.0	25	21.9	39.6	5.8
4	120	18.0	25	36.3	89.9	6.8
5	48	7.2	0	22.6	30.5	4.3
6 †	132	19.8	0	46.3	86.2	4.8
7	90	13.5	-35	40.1	64.2	4.3
8	90	13.5	35	25.2	69.4	8.3
9	90	13.5	0	35.0	57.7	5.6
10	90	13.5	0	35.0	56.5	5.3
11	90	13.5	0	35.3	60.4	5.6
12	120	18.0	0	44.2	78.5	5.0
13 †	60	9.0	0	28.0	41.4	4.6

1 ... 4 Corner points 5 ... 8 Star points
9 ... 10 Centre points 11 ... 13 Additional points

† Seams with welding defects (pores) in section cut

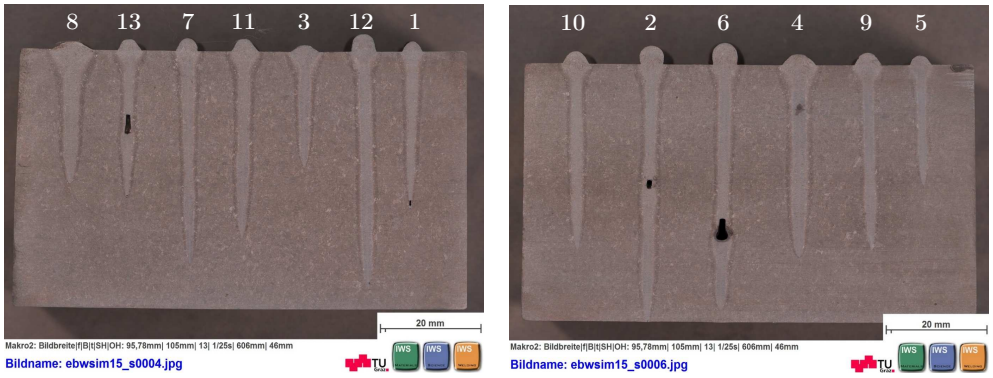

Figure 3.11: *Section cut of bead on plate welds without beam oscillation through 1.4313 steel specimen; thickness* $\approx 80\,\mathrm{mm}$*; Welding parameters according to Table 3.5*

Chapter 4

Numerical simulation

4.1 LaserCAD

The software LaserCAD was developed by the team of Prof. Gleb A. Turichin[1] from St. Petersburg State Polytechnic University (SPbSPU) in cooperation with RWTH-Aachen University. Unless otherwise indicated, the information in this section is taken from [4].

4.1.1 Introduction and overview

LaserCAD is a CAE system to predict the geometrical characteristics of welds made with beams of high energy density. It calculates the steady state solution of beam welding processes and is based on special numerical and analytical models developed by Prof. Turichin. [51] Among deep penetration models of laser beam welding and electron beam welding, models of hybrid welding with deep penetration and surface melting are included.

The laser welding model calculates the heat transfer solution in liquid and solid phases, solution of melt flow hydrodynamics, metal vapour flowing and laser-induced plasma formation as well as beam-plasma interaction. The model for electron beam welding considers heat and mass transfer, gas dynamics, dispersion kinetics of metal vapours in vacuum and beam scattering due to metal vapour in deep penetration welding.

A graphical user interface in dialogue mode offers a convenient and clear work environment (Figure 4.1). The system is developed as a MDI[2] programme and allows the user to work in multi-window mode (Figure 4.2). Several independent simulations can be opened and edited simultaneously, which facilitates the comparison and analysis of calculated results. Written in Object Pascal in Delphi6 developement system, the mathematical models and the solving algorithms are optimised for efficient computation with a minimum of resources. Hence, the calculation of one welding mode with minimal system requirements (Pentium-III/700, 128 Mb RAM) can be fulfilled in less than one minute.

The information of the investigated materials is stored in the integrated material database system for metals, alloys and non-metals[3] as shown in Figure 4.3. Among data about thermophysical properties and chemical composition, for steel materials

[1] Head of the Institute of Laser and Welding Technology at SPbSPU, Russia
[2] Multiple document interface
[3] Only for laser beam welding, not for electron beam welding

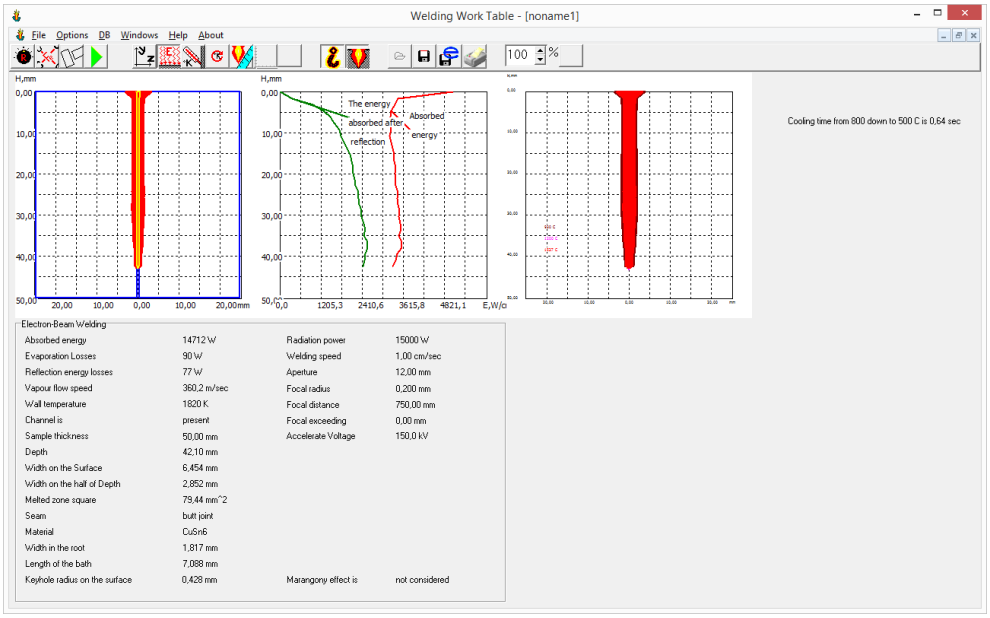

Figure 4.1: *Graphical user interface of LaserCAD Version 4.0 with a sample calculation output for an electron beam welding simulation; screenshot from [2]*

Figure 4.2: *Multi-window mode for simultaneous analysis of several simulation problems; screenshot from [2]*

it is possible to insert data on phase transformation behaviour in form of a CCT-diagram[4]. For laser beam welding applications, a process equipment database (Figure 4.4) is included for easy selection of proper equipment according to the process requirements. All databases are accessible not only for updating and editing, but also for adding new material or equipment entries.

LaserCAD's field of application is not only the technological process designing of weldings and finding suitable process parameters, equipment and material [52, 53], but also serving as a computer simulator to train the technical personnel in handling beam welding machines.

[4]Continuous cooling transformation diagram

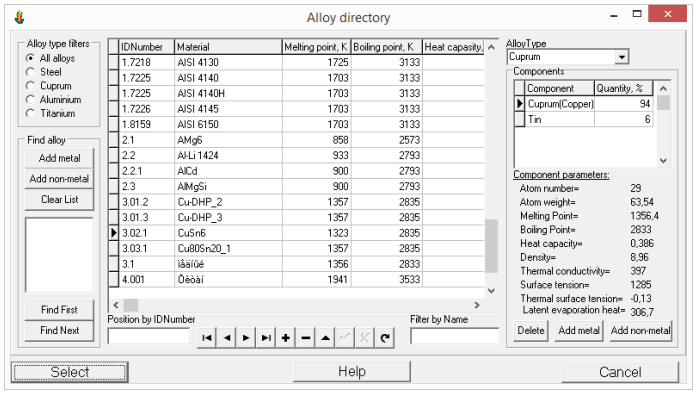

Figure 4.3: *Material database; screenshot from [2]*

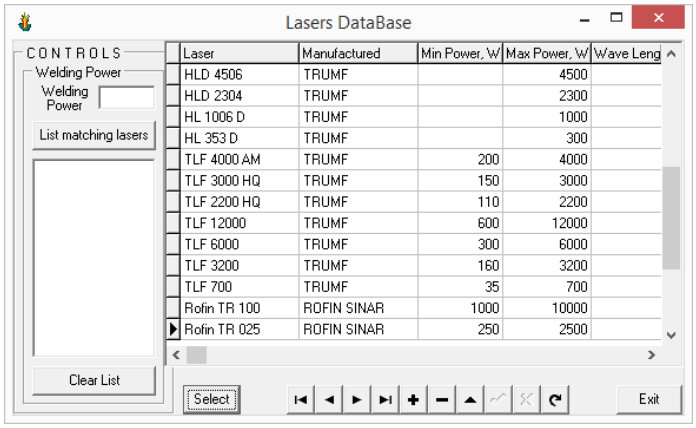

Figure 4.4: *Laser equipment database; screenshot from [2]*

Since the Institute of Laser and Welding Technology at SPbSPU is well equipped with different laser welding machines, the development of LaserCAD was primarily done for the laser welding model. Physically adequate models of essential processes for laser welding simulation like laser-induced plasma formation [54] and laser-plasma interaction [55] are implemented in LaserCAD. Formation of plasma during laser welding may result in the reduction of the impinging laser power on the workpiece. This shielding effect leads to a limitation of the penetration depth and can have a negative impact on the quality of the welding. Also different models for hybrid laser welding [56] like laser-arc and laser-light welding have been realised.

Moreover, a model for thermocapillary convection has been developed and implemented in LaserCAD. When the surface tension of the liquid metal depends on the temperature ($\sigma_L \neq 0$), a fluid flow of the molten material emerges in presence of a temperature gradient. The so-called Marangoni effect influences size and shape of the melt pool [57] (see also Section 4.2.5).

In [58], a model for calculating temperature field and melt pool behaviour in pulse laser welding under space conditions is introduced. Not implemented in the provided version of LaserCAD, the mentioned model can support repair welding missions for manual repairing of constructions in space.

Besides improvements of steady state process models, dynamic models are currently beeing developed [59–61]. The description of the melting pool's dynamic behaviour makes it possible to predict keyhole oscillation effects and thus welding defects like pores or humping [59, 60]. Likewise dynamic hybrid welding models are investigated [61]. Contemporary, these models are in research state and not implemented

in the current version of LaserCAD due to occasionally occurring instabilities [62]. Further maturation of such dynamic models and their implementation in the software will for sure broaden LaserCAD's scope of application.

4.1.2 About the EBW process model

Since the EB-model, developed by Prof. Turichin, is not open for public access, no detailed information about the mathematical models can be presented. Nevertheless, a rough overview based on [62], in order to understand LaserCAD's operating principles can be given.

Calculation algorithm

The solution of the mathematical model for EBW with deep penetration is a complex problem. A number of tasks, such as electron beam absorption and multiple beam reflection, evaporation and vapour flow dynamics inside the keyhole, heat transfer in solid and liquid phase and the melt flow around the keyhole need to be solved. Looking at the structure of LaserCAD's steady state process model in Figure 4.5, one can notice that many tasks are connected to each other. A special numerical-analytical algorithm with iterative computation steps was developed and implemented in LaserCAD.

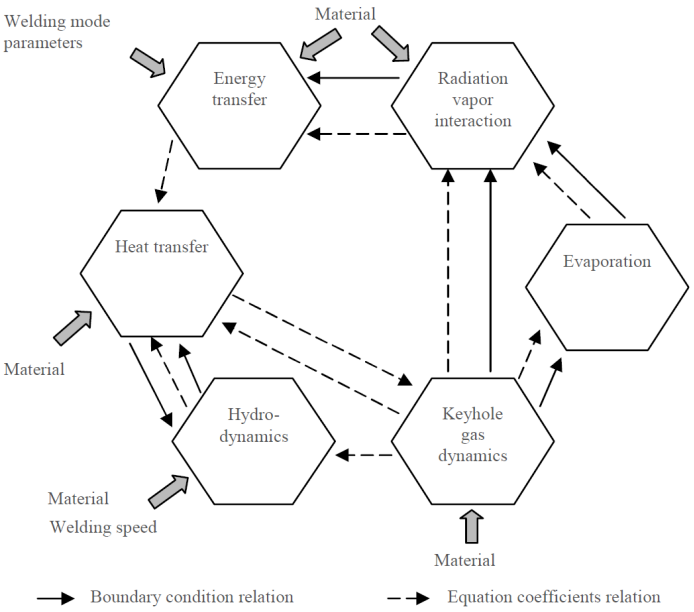

Figure 4.5: *Structure of LaserCADs steady state process model for beam welding processes; adapted from steady state process for hybrid welding from [61]*

Beginning at the upper surface, the size and shape of the keyhole and the fusion zone as well as the temperature distribution in the liquid and the solid phase are calculated layer by layer.

Although physical parameters of metal materials generally depend on temperature, LaserCAD uses constant values for the calculation. An ambience temperature of 20 °C and a chamber pressure of 0.0001 mm Hg = 1.3×10^{-4} mbar is determined in LaserCAD.

Energy absorption

A physically adequate model based on geometric beam optics is used to calculate the reflection and absorption of the impinging beam. The model considers a variation of the reflection coefficient depending on the angle of incidence and the angular distribution of the reflected electrons. As a result of multiple reflections, the model gives distributions of the absorbed power over the keyhole depth for both, initially absorbed energy and absorbed energy after reflection.

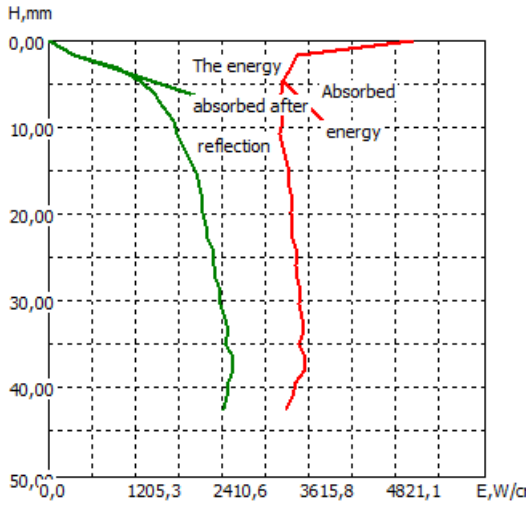

Figure 4.6: *Distribution of initially absorbed energy and absorbed energy after reflection over the penetration depth H; Unit of E is* $^{\mathrm{W}}/_{\mathrm{cm}}$

Losses due to electron reflection and losses due to metal vapour flow out of the cavity are considered. Radiation losses are not taken into account.

Beam-material interaction

The heat generation of the impinging beam is assumed to take place directly at the cavity surface. Transformation of the electrons' kinetic energy into thermal energy owing to multiple collisions with nuclei and electrons of the material are not considered. Since these complex interaction processes happen in a very thin layer under the surface [37, 43], this simplification is eligible.

Keyhole model

The forces considered in the keyhole model are the surface tension, vapour pressure, hydrostatic pressure, chamber pressure and gravity (see Figure 2.26 on page 28).

Melt flow

Since experiments showed that v_z, the melt velocity component parallel to the cavity axis is very small compared to other directions ($v_z \ll v_x, v_y$), the melt flow is described as a two-dimensional problem in a plane perpendicular to the cavity axis. Estimated Reynolds number is rather small ($Re \approx 10 \ldots 10^3$), thus ideal liquid flow (potential flow, $\nabla\varphi = 0$) is assumed, except at the area near the two boundary surfaces (solid-liquid boundary and keyhole wall). The evaporation flux at the keyhole wall is neglected (impenetrable boundary for liquid flux). The velocity at the solid-liquid boundary is equal to zero. Additionally a region of turbulent trace emerging behind the keyhole is taken into account.

Heat transfer

Convective heat transfer is considered. The fluid flow around the keyhole transfers mass, thus heat to the rear of the melt pool and shifts the melt pool's widest part to the tail. Latent heat of melting is neglected. Heat loss owing to evaporating material is neglected, since it is $\sim 100 \ldots 1000$ times smaller than the flux density of the radiation power impinging on the keyhole wall. Two different heat transfer models (HTM) are implemented in LaserCAD, a 2D- and a 3D-HTM. The 2D model assumes no heat flux in z-direction, while the 3D model allows heat flux in all directions.

4.1.3 Process data

This section will give a brief overview about necessary input data when dealing with the program as well as obtainable calculation output data.

Input data

LaserCAD's input parameters (Table 4.1) can be divided into three groups, beam-, material- and joint-parameters. All parameters can easily be entered in the input windows shown in Figure 4.7.

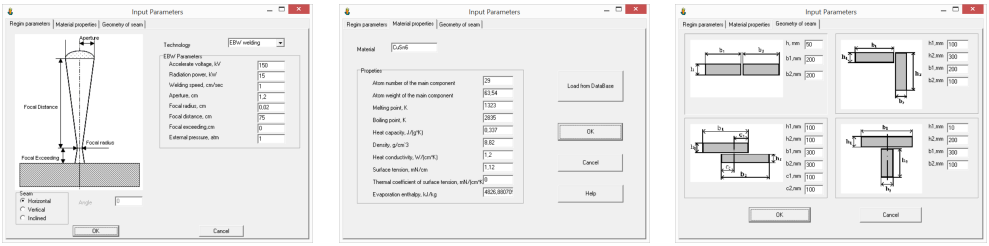

(a) *Beam parameters* **(b)** *Material properties* **(c)** *Seam geometry*

Figure 4.7: *LaserCAD input window for calculation input parameters; screenshots from [2]*

After choosing the proper welding technology, in our case electron beam welding, selection of 2D- or 3D-HTM and entering all necessary input data, the simulation can be started.

Output data

Once the computation is done, following information is available as output data.

Graphic output data In the cross section result (Figure 4.8a), as well as in the longitudinal section result (Figure 4.8b) the yellow-coloured area denotes the keyhole (vapour phase), the red-coloured area identifies the molten material (liquid phase) and the white-coloured area the base material (solid phase). They show the steady state during the welding process. It can happen, that inside the yellow area, another red area appears (e.g. Figure 4.13 on page 51), according to [63], this can be attributed to a failure in the graphical computation and has no relevance for the interpretation of the result.

Table 4.1: *Overview of LaserCAD's input parameters*

Parameter (as mentioned in LaserCAD)	Symbol	Unit	Description
Beam parameters			
Acceleration voltage	U_A	kV	
Radiation power	P	kW	Beam power = $U_A \cdot I_B$
Welding speed	v	$^{cm}/_{s}$	
Aperture	A	cm	Beam radius at lens
Focal radius	r_0	cm	
Focal distance	L_F	cm	Figure 2.15
Focal exceeding	f_P	cm	
External pressure	p_A	atm	Working pressure in chamber
Material properties			
Melting point	T_M	K	
Boiling point	T_B	K	
Heat capacity	c_p	$^{J}/_{(g\ K)}$	
Density	ρ	$^{g}/_{cm^3}$	
Heat conductivity	λ	$^{W}/_{(cm\ K)}$	Thermal conductivity
Surface tension	σ_L	$^{N}/_{m}$	
Thermal coeff. of surf. tens.	σ_T	$^{mN}/_{(m\ K)}$	
Evaporation enthalpy	ΔH_{LG}	$^{kJ}/_{kg}$	Latent heat of evaporation
Joint geometry			
Type of joint			Butt-, Corner-, Lap- or T-joint
Thickness	h	mm	
Width	b	mm	

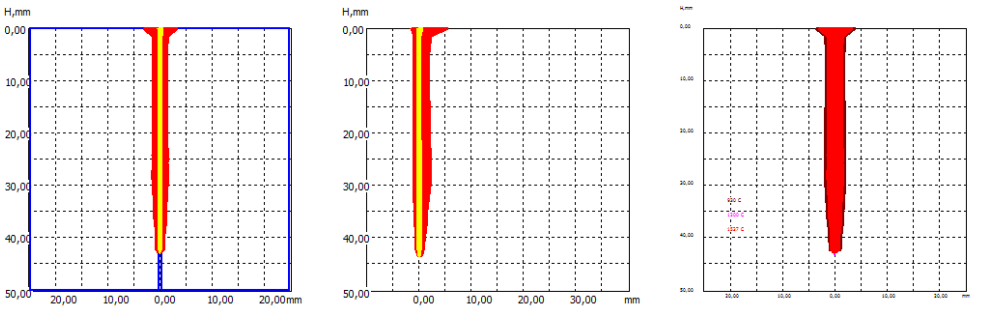

(a) *Cross section plane*

(b) *Longitudinal section plane*

(c) *Cross section plane with heat affected zone*

Figure 4.8: *LaserCAD's graphical output data (I)*

In Figure 4.8c, which can be seen as a section cut after the welding process, the red area denotes the fusion zone area and the heat affected zone (HAZ) is supposed to be indicated by purple and brown areas. For the present case, the HAZ is indicated very narrow.

Additionally, the distribution of the initially absorbed energy and absorbed energy after reflection along the cavity axis, the keyhole wall temperature distribution and the thermal cycle of any chosen point of the cross section plane are outputted (Figure 4.9).

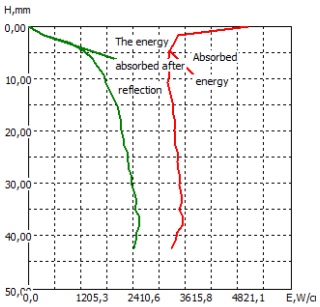

(a) *Distribution of absorbed energy along the keyhole depth*

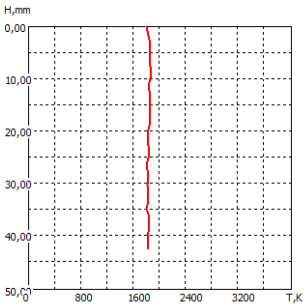

(b) *Distribution of keyhole wall temperature along the keyhole depth*

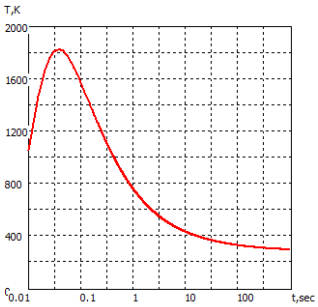

(c) *Thermal cycle of a point chosen from the cross section plane*

Figure 4.9: *LaserCAD's graphical output data (II)*

Moreover, for steel materials it is possible to provide data of CCT-diagrams and, together with the thermal cycle diagram, to predict the microstructure of the FZ and the HAZ.

Numeral output data Besides the graphical output described above, several calculation results are provided as numeral values, listed in Table 4.2. Among seam geometry-related output data like penetration depth and melted zone square (FZ area) information on the keyhole and energy balance is also available.

Table 4.2: *LaserCAD's numeral output values*

Output attribute	Output unit	Note
Depth	mm	Seam geometry-related
Width on the Surface	mm	
Width on the half of Depth	mm	
Width in the root	mm	
Melted zone square	mm^2	
Length of the bath	mm	
Absorbed energy	W	Energy-related
Evaporation losses	W	
Reflection energy losses	W	
Wall temperature	K	Keyhole-related
Keyhole radius on the surface	mm	
Vapour flow speed	$^m/_s$	

4.2 Systematic analysis

Following investigations were done to find out about the influence of input parameters on the response of LaserCAD's EB-model. It is essential to be aware of the fact, that there are no "correct" input values for a numerical welding calculation. In practice neither beam parameters nor material parameters are precise.

Defined in EN ISO 14744 [64–69], acceptable welding parameter variations of EBW machines underlie a small tolerance range. Nevertheless, slight fluctuations of acceleration voltage, beam power, focus position, etc. occur.

Likewise, material properties cannot be assumed as constant or precise. According to the chemical composition of metal materials, standards define tolerance ranges, minima or maxima. The amount of admixtures, alloying elements or impurities differs not only from one manufacturer to another, but also from batch to batch. Even in one workpiece the composition and hence the physical properties are not uniform across the whole volume.

Therefore not "correct" but "suitable" input parameters are needed in order to obtain proper results. For appropriate interpreting of these results and to estimate the influence of divergences between simulation and real process, it is necessary to grasp the impact of the various input parameters on LaserCAD's calculation output.

4.2.1 Beam parameters

Investigations on beam parameter influences have been done with material 1.4313 for the following reasons. EB-weldings of steels are widely used and well known in literature, which makes it reasonable to compare LaserCAD's behaviour with such materials. Experimental data for 1.4313 is available at the Institute of Materials Science and Welding at TU Graz.

Performance-related parameters

Acceleration voltage U_A, radiation power P ($= U_A \times I_B$) and welding speed v are direct input parameters for EBW-machines. Like mentioned above, hardly any fluctuations of these parameters during the welding process can be expected. A parameter study was made to investigate the EB-model's behaviour, resulting from the variation of these parameters. A central composite design plan (CCD) was chosen to provide the basis for the parameter study. CCD needs more data in comparison to a factorial design plan, but can describe non-linear relations between input factors and responses [70]. In the case at issue, where the "experiments" are simulations with LaserCAD, thus not very time consuming, and factors are few, the additional effort is small. The design of experiments (DoE) schedule (Table 4.3) and the analysis was made with the help of the statistical software Minitab 17 [71].

Looking at Figure 4.10, the model shows reasonable behaviour. With increasing U_A and I_B as well as decreasing v, the energy input per unit length $E = U_A \cdot I_B \cdot v^{-1}$ increases. Thus the penetration depth as well as the fusion zone area increases, which can be found in literature likely [37, p. 49, Fig. 62] [72].

The interaction plots reveal almost parallel graphs, hence no strong interactions between the three factors U_A, I_B and v can be detected. Nevertheless with higher beam current I_B the influence of the welding speed v on the penetration depth H and fusion zone area S increases. An experimental study at IWS at TU Graz done for the martensitic chromium-nickel stainless steel 1.4317 showed a similar interaction behaviour [76] (Figure 4.11).

Table 4.3: *CCD DoE schedule with the three factors U_A, I_B and v and two responses penetration depth H and fusion zone area S*

	Factors (input)			Responses (output)	
No.	Acceleration voltage U_A kV	Beam current I_B mA	Welding speed v $^{cm}/_{s}$	Penetration depth H mm	Fusion zone area S mm^2
1	100.00	50.00	1.00	30.83	53.60
2	150.00	50.00	1.00	44.33	93.38
3	100.00	100.00	1.00	50.70	88.31
4	150.00	100.00	1.00	70.95	148.53
5	100.00	50.00	2.00	23.33	33.20
6	150.00	50.00	2.00	33.83	57.84
7	100.00	100.00	2.00	37.20	52.56
8	150.00	100.00	2.00	50.70	84.84
9	82.96	75.00	1.50	30.08	53.78
10	167.04	75.00	1.50	55.20	92.39
11	125.00	32.96	1.50	23.33	31.51
12	125.00	117.04	1.50	55.20	101.73
13	125.00	75.00	0.66	58.58	109.44
14	125.00	75.00	2.34	34.95	44.36
15	125.00	75.00	1.50	42.83	62.49

Geometry-related parameters

Aperture radius A, focal radius r_0, focal distance L_F and focal exceeding f_P define the geometric form and dimensions of the beam. Since the upmost layer of the defined material serves as "input" for the calculation algorithm [62], only the shape of the impinging beam on the upper surface has an influence on the calculation. To be exact, solely the diameter of the beam on the surface d_S and the impinging angles of the electrons determine the calculation results.

Since the angle of divergence θ can be calculated as $\theta = \arctan(^{A}/_{L_F})$, a change of the focal distance by multiplying it with a factor X like $L_F^* = L_F \cdot X$ will not change the beam impinging angle, as long as the value for aperture is also changed to $A^* = A \cdot X$. Calculations with A^* and L_F^* instead of A and L_F lead to the exact same results, independent of factor X's magnitude.

This observation implies, that trajectories of electrons do not change, no matter how long the electrons have to travel through an ambience with the pressure p_A. In other words, no beam scattering owing to working pressure (Figure 2.19) is taken into account. Since $p_A \ll 10^{-2}$ mbar, this influence is definitely negligible [37, p. 59].

The focal radius r_0 is a critical input factor in the meaning of finding suitable values. The size of the beam diameter in the focal spot depends on the two performance-related parameters acceleration voltage U_A and beam current I_B and on the geometry-related parameter beam divergence θ (or focal distance L_F). With decreasing U_A or

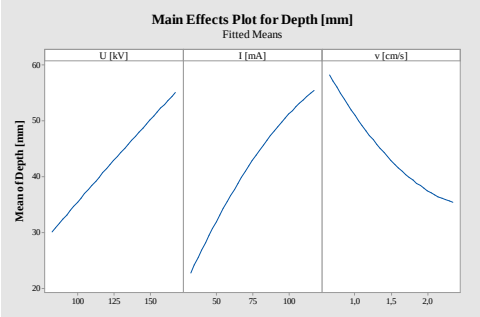

(a) *Main effects plot for penetration depth H*

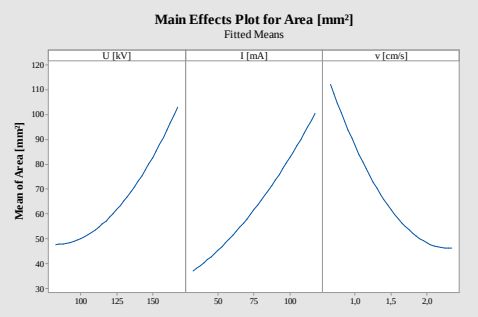

(b) *Main effects plot for fusion zone area S*

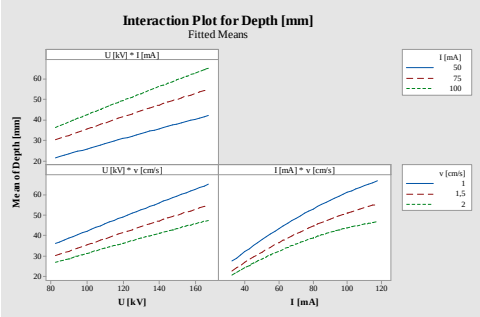

(c) *Interaction plot for penetration depth H*

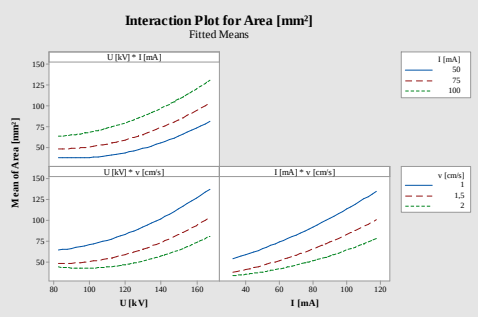

(d) *Interaction plot for fusion zone area S*

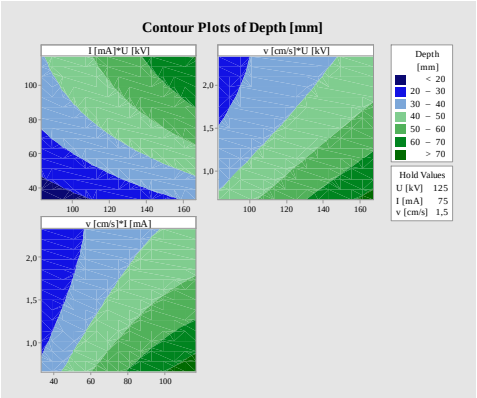

(e) *Contour plots of penetration depth H*

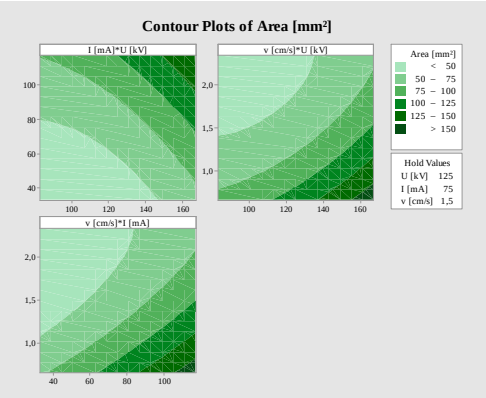

(f) *Contour plots of fusion zone area S*

Figure 4.10: *Main effects, interactions and contour plots for the responses (penetration depth H and fusion zone area S) on the factors acceleration voltage U_A, beam current I_B and welding speed v [71]*

increasing I_B the focal diameter d_0 increases [37, p. 40]. Divergence θ and focal diameter d_0 define the beam parameter product (BPP) or emittance ε with the unit mm·mrad [40, 73]:

$$\varepsilon = \frac{d_0 \cdot \theta}{4} \tag{4.1}$$

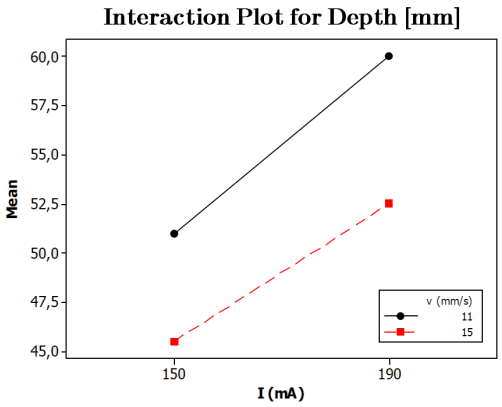

Figure 4.11: *Interaction plot for penetration depth H on the factors beam current I_B and welding speed v; DoE: Full factorial design; Acceleration voltage: U_A = 150 kV Material: Steel 1.4317; Specimen thickness:* 80 mm*; Oscillation figure: Ellipse (*dx = 1 mm, dy = 0.5 mm, f = 1 kHz*); adapted from [76]*

In this equation ε is a conserved quantity, as long as there are no image defects in beam optics. A more focused beam leads to a bigger divergence angle θ and to a smaller focal diameter d_0. With known emittance ε, the beam diameter for each divergence angle (focal position) can be calculated.

For the electron beam welds made in Graz, different settings for U_A and I_B were used. The emittance and divergence measurements were made by PRO-BEAM [46]. The measured angle of divergence θ_C is the beam divergence at the cathode. For small divergence angles, the divergence at the electromagnetic lens θ can be calculated by multiplying θ_C with the ratio of crossover distance (distance from virtual crossover to lens) and focus distance:

$$\theta = \theta_C \cdot \frac{L_C}{L_F} \tag{4.2}$$

Table 4.4: *Used beam parameters and measured values for beam emittance ε, beam divergence in the crossover at the cathode θ_C and distance from crossover to lens L_C by* PRO-BEAM*; Measurements with U_A = 150 kV where unsuccessfull due to the high beam power [46]*

Acceleration voltage U_A kV	Beam current I_A mA	Beam power P kW	Beam emittance ε mm·mrad	Divergence at crossover θ_C mrad	Crossover distance L_C mm
150	60 . . . 210	9 . . . 31.5	—	—	—
120	60	7.2	3.0	29	760
120	80	9.6	3.5	30	764

The beam diameter is usually defined as a diameter which indicates a specified amount of the assumed GAUSSIAN distribution of the power density of the electron beam. Therefore it is necessary to bare in mind, that LaserCAD's beam intensity distribution is calculated by

$$I(r) = I_0 \cdot \exp\left(-\frac{r^2}{r_{0,\mathrm{LC}}^2}\right) \tag{4.3}$$

where LaserCAD's focal radius input $r_{0,\mathrm{LC}}$ indicates a circular surface, corresponding to $(1 - 1/\mathrm{e}) \simeq 63\,\%$ of the total beam power [62]. Provided beam parameter measurements by PRO-BEAM base on a GAUSSIAN distribution of

$$I(r) = I_0 \cdot \exp\left(-2\frac{r^2}{r_{0,\mathrm{PB}}^2}\right), \tag{4.4}$$

where the measured focal radius $r_{0,\mathrm{PB}}$ indicates a circular surface, corresponding to $(1 - 1/\mathrm{e}^2) \simeq 86.5\,\%$ of the total beam power [46]. To avoid divergences between calculation input and measurement as depicted in Figure 4.12a, the measured focal radius $r_{0,\mathrm{PB}}$ needs to be multiplied with factor $1/\sqrt{2}$ (Figure 4.12b):

$$\begin{aligned} I(r)_{\mathrm{LC}} &\stackrel{!}{=} I(r)_{\mathrm{PB}} \\ I_0 \cdot \exp\left(-\frac{r^2}{r_{0,\mathrm{LC}}^2}\right) &= I_0 \cdot \exp\left(-2\frac{r^2}{r_{0,\mathrm{PB}}^2}\right) \\ r_{0,\mathrm{LC}} &= \frac{r_{0,\mathrm{PB}}}{\sqrt{2}} \end{aligned}$$

In this document, when the focal radius r_0 is written without indices "LC" or "PB", the input value for LaserCAD $r_{0,\mathrm{LC}}$ is meant:

$$r_0 = r_{0,\mathrm{LC}}$$

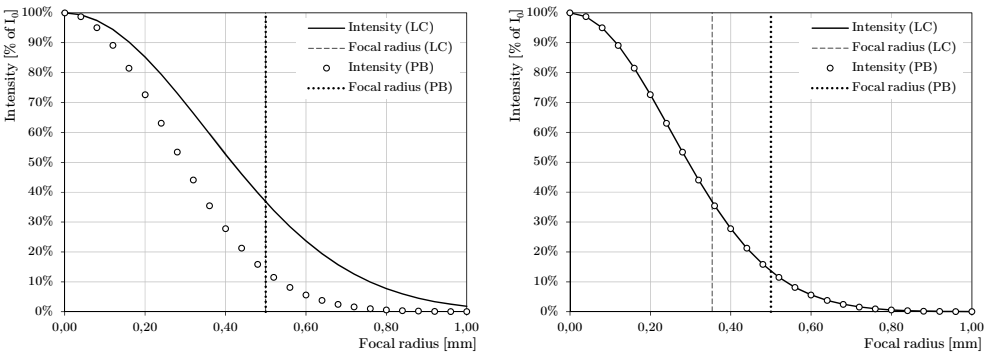

(a) *Setting LaserCAD's focal radius input value to $r_{0,\mathrm{LC}} = r_{0,\mathrm{PB}}$ leads to a divergent beam intensity distribution in comparison to experiment*

(b) *Setting $r_{0,\mathrm{LC}} = r_{0,\mathrm{PB}} \cdot 1/\sqrt{2}$ brings LaserCAD's beam intensity distribution equal to the measured intensity distribution*

Figure 4.12: *Difference between focal radius measured by* PRO-BEAM *and focal radius input value for LaserCAD;* (LC)*... LaserCAD input;* (PB)*... Measurement by* PRO-BEAM

Concerning the parameter cases with known beam diameters (Table 4.5) investigations on the influence of deviations from these focal radii were conducted. Starting from calculations with known focal radius r_0 (60 mA and 80 mA at 120 kV), the radius was varied from $0.4 \times r_0$ to $2 \times r_0$ and the influence on LaserCAD's results of depth, area, width and length of the weld seam was examined. Besides calculations for the stainless steel 1.4313, simulations with the bronze material Cu80 Sn20 were also done. The deviations were calculated according to equation (4.5), where X is a particular value with a deviation $\mathrm{dev}(X)$ compared to a reference value X_0. In Figure 4.14, the

outcomings are shown. Reference values for all parameters were simulation results for known beam parameters (normalised focal radius = 1).

$$\mathrm{dev}(X) \quad = \quad \frac{X}{X_0} - 1 \tag{4.5}$$

Table 4.5: *Aperture A and focal radius r_0 calculated for the known beam parameters from Table 4.4*

Acceleration voltage U_A kV	Beam current I_A mA	Beam power P kW	Aperture A cm	Focal radius r_0 cm
120	60	7.2	1.10	0.14
120	80	9.6	1.15	0.16

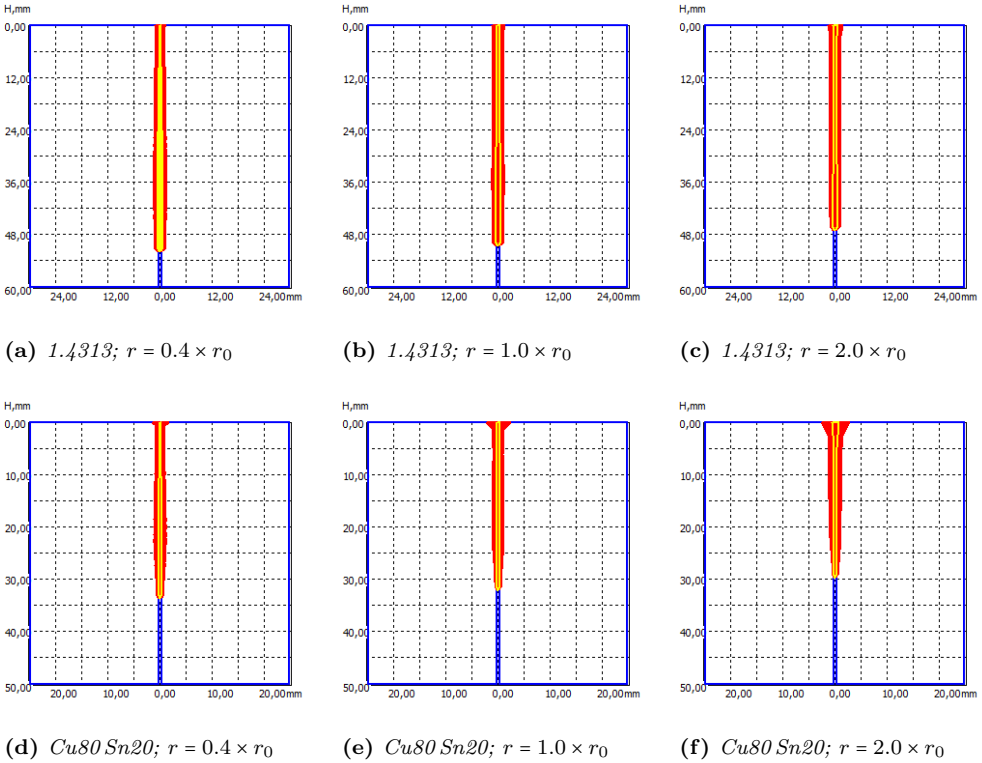

(a) *1.4313;* $r = 0.4 \times r_0$ **(b)** *1.4313;* $r = 1.0 \times r_0$ **(c)** *1.4313;* $r = 2.0 \times r_0$

(d) *Cu80Sn20;* $r = 0.4 \times r_0$ **(e)** *Cu80Sn20;* $r = 1.0 \times r_0$ **(f)** *Cu80Sn20;* $r = 2.0 \times r_0$

Figure 4.13: *Cross section results for investigations on focal radius influence;* $U_A = 120\,\mathrm{kV}$*;* $I_B = 80\,\mathrm{mA}$*;* $v = 10\,\mathrm{mm/s}$*;* $f_P = 0\,\mathrm{mm}$

Up to a focal radius input of $\sim 2 \times r_0$, the penetration depth results are relatively stable. At this point, a reduction of only approximately 7 % takes place. Further considerations show, that at $\sim 2.5 \times r_0$ penetration depth reductions of 10 % and at $\sim 4 \times r_0$ reductions of 30 % occur.

The result of the width on the surface W_0 is nearly proportional to the focal radius input. As already mentioned, the upper layer with impinging beam serves as the input layer for the model, this behaviour is evident.

Similar observations can be seen in [37, p. 40], where welds with different focal distances are compared. An increasing focus length L_F leads to decreasing θ and, according to equation (4.1), an increasing focal diameter d_0. This results in broadening of the welding geometry and reducing of the penetration depth [37, p. 40, Fig. 46].

Looking at the graph for the fusion zone area, a difference between steel and bronze material becomes apparent. Whilst the fusion zone area of 1.4313 is almost constant and does not change within a range of $0.4 \times r_0$ to $2 \times r_0$, the fusion zone area of bronze material shows an increasing behaviour with increasing focal radius.

This means, that the width of the seam is independent of the focal radius at steel weldings but increases linearly with increasing r_0 at bronze weldings.

For both, steel and bronze material, the length of the bath linearly depends on the focal radius input. The bathlength increases and decreases according to r_0.

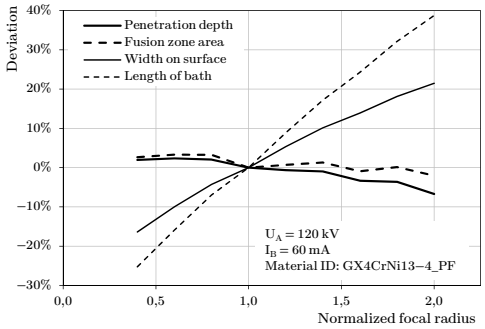

(a) *Stainless steel;* $U_A = 120\,\mathrm{kV}$*;* $I_B = 60\,\mathrm{mA}$

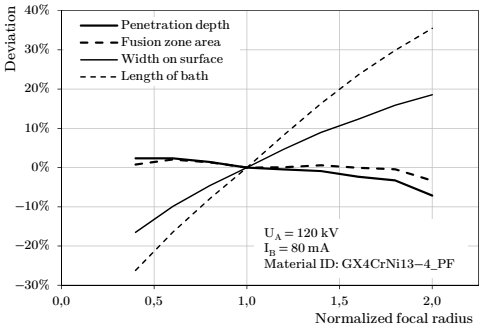

(b) *Stainless steel;* $U_A = 120\,\mathrm{kV}$*;* $I_B = 80\,\mathrm{mA}$

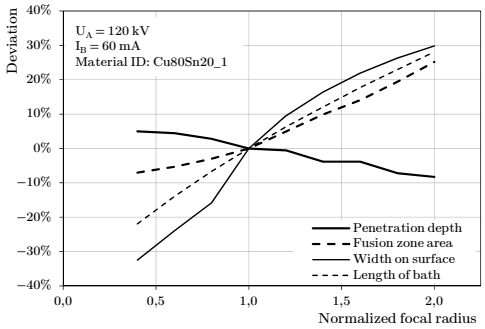

(c) *Bronze;* $U_A = 120\,\mathrm{kV}$*;* $I_B = 60\,\mathrm{mA}$

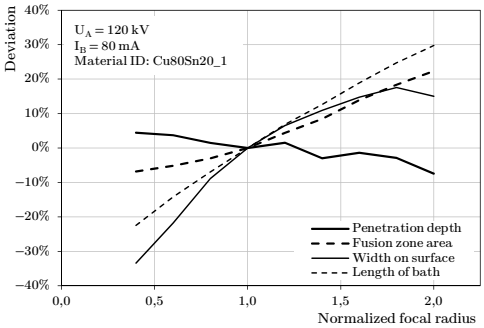

(d) *Bronze;* $U_A = 120\,\mathrm{kV}$*;* $I_B = 80\,\mathrm{mA}$

Figure 4.14: *Normalised focal radius versus penetration depth H, fusion zone area S, width on surface W_0 and length of bath L*

Table 4.6: *Material input parameters for investigations on geometry-related parameter influences*

Attribute		Steel 1.4313	Bronze Cu80 Sn20	Unit
Material ID		GX4CrNi13-4_PF	Cu80Sn20_1	
Melting point	T_M	1725	1357	K
Boiling point	T_B	3133	2835	K
Heat capacity	c_p	0.46	0.40	$^{J}/_{(g\ K)}$
Density	ρ	7.70	8.70	$^{g}/_{cm^3}$
Heat conductivity	λ	0.25	1.00	$^{W}/_{(cm\ K)}$
Surface tension	σ_L	1.82	0.84	$^{N}/_{m}$
Thermal coeff. of surf. tens.	σ_T	0.034	0.000	$^{mN}/_{(m\ K)}$
Evaporation enthalpy	ΔH_{LG}	6092.41	4826.88	$^{kJ}/_{kg}$

4.2.2 Material properties

The input of material properties comes with a high potential of error sources. Besides the fact, that physical properties depend on the chemical composition of the material, hence underlie a considerable range of variations, whilst not all properties necessary for the simulation are known for each material. Especially properties at high temperatures are difficult to find for certain materials.

In order to estimate the influence of input parameters for different material properties, several simulations were conducted. Starting from parameters for steel from Table 4.6, one by one a single parameter was changed and the influence in penetration depth and area was observed. The variation of the input property as well as the variation of the calculation results were normalised and compared. Table 4.7 gives an overview of the different material factors and its influence on penetration depth and fusion zone area.

Table 4.7: *Variation of material properties and its influence on calculated penetration depth and melted zone area*

Attribute		Value adjustment	Penetration depth	Fusion zone area
Melting point temperature	T_M	↑	⇆	↓
Boiling point temperature	T_B	↑	○	○
Heat capacity	c_p	↑	↓	↓
Density	ρ	↑	↓	↓
Thermal conductivity	λ	↑	↓	↓
Surface tension coefficient	σ_L	↑	↓	↑
Surface tension temp. coeff.	σ_T	↑	○	⇆
Latent heat of evaporation	ΔH_{LG}	↑	↓	↑

↑ . . . increasing ↓ . . . decreasing ⇆ . . . weak influence ○ . . . no influence

This matrix can be used as a rough overview to estimate the influence of the material input parameters on LaserCAD's result. For a deeper understanding of material-related influences on the EB-model, especially interactions between the dif-

ferent parameters, a DoE investigation using MINITAB 17 [71] was done. To examine the main effects of the 8 material input factors and to identify the critical factors with the major influence on the results, a screening design plan was created. Table 4.8 shows the defined level values for each factor. A screening plan with 24 runs was defined.

Table 4.8: *Factor levels of the material input parameters for the screening design plan*

Factor		Low	High	Unit
Melting point	T_M	1400	1700	K
Boiling point	T_B	2800	3100	K
Heat capacity	c_p	0.38	0.47	$^{J}/_{(g\ K)}$
Density	ρ	7.70	8.70	$^{g}/_{cm^3}$
Heat conductivity	λ	0.25	1.00	$^{W}/_{(cm\ K)}$
Surface tension	σ_L	0.80	1.80	$^{N}/_{m}$
Thermal coeff. of surf. tens.	σ_T	0.05	0.20	$^{mN}/_{(m\ K)}$
Evaporation enthalpy	ΔH_{LG}	4800	6100	$^{kJ}/_{kg}$

As results to be analysed, besides the penetration depth H, the ratio of the fusion zone area per penetration depth S/H were chosen. Simple consideration of the fusion zone area S would not be reasonable, since the magnitude of S is directly correlated with the penetration depth H. The variable S/H can be seen as a normalised fusion zone area and is practically the average width of the seam.

The main effects plot (Figure 4.15) shows, that thermal conductivity λ has the biggest influence in H, followed by latent heat of evaporation ΔH_{LG} and surface tension σ_L.

While the melting point temperature has no influence on the penetration depth at all, the effect for S/H is rather significant. The factors surface tension σ_L and latent heat of evaporation ΔH_{LG} correlate proportional with S/H and inversely proportional with H. The higher the evaporation enthalpy, the smaller the penetration depth but the broader the seam ($S/H \mathrel{\hat{=}}$ average width). Surface tension shows similar behaviour.

When the factors are arranged according to their impact on the responses, it is easy to figure out which factors are relevant for the observed output and which ones are not. For penetration depth, the most important factor is the thermal conductivity λ, followed by ΔH_{LG}, σ_L and c_p. The standardised effect of density ρ is with ~ 2.13 only one potential factor having an effect on H, hence the density was neglected for further investigations.

The greatest effects concerning the width of the seam are detected observing melting point T_M, heat conductivity λ and latent heat of evaporation ΔH_{LG}, followed by σ_L and c_p. Boiling point T_B, density ρ and temperature coefficient of surface tension σ_T have neglectable effects on S/H.

A CCD plan to find out about possible interactions between the main factors of penetration depth H was set up. 30 runs for the 4 most important factors λ, ΔH_{LG}, σ_L and c_p with factor levels from Table 4.9 were done. Other material input values were $T_M = 1400\,\mathrm{K}$, $T_B = 2800\,\mathrm{K}$, $\rho = 8.70\,{}^{g}/_{cm^3}$ and $\sigma_T = 0.20\,{}^{mN}/_{(mK)}$.

As shown in Figure 4.17, there are no strong interactions between these four investigated parameters. Nevertheless weak interactions between λ and c_p as well as between λ and σ_L can be recognised. With increasing thermal conductivity λ, the influence of c_p and σ_L on the penetration depth decreases.

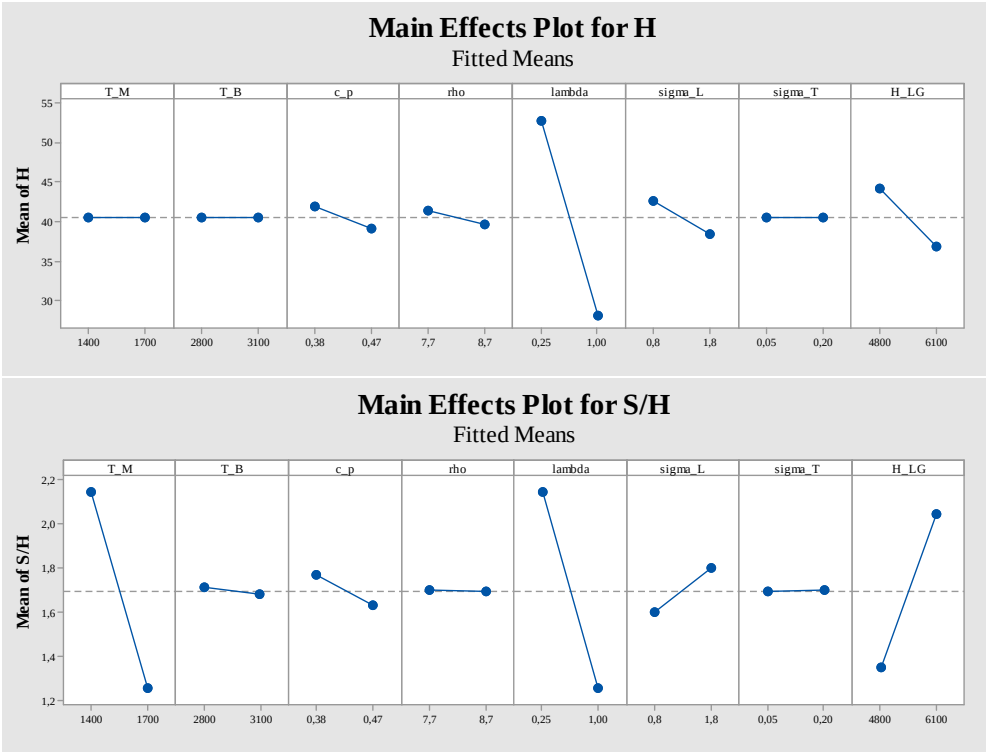

Figure 4.15: *Main effects plot of material properties on the responses depth H and area per depth S/H [71]*

Table 4.9: *Factor levels of the material input parameters for the CCD plan*

Factor		Low	High	Unit
Heat capacity	c_p	0.35	0.50	$^{\mathrm{J}}/_{(\mathrm{g\ K})}$
Heat conductivity	λ	0.50	1.00	$^{\mathrm{W}}/_{(\mathrm{cm\ K})}$
Surface tension	σ_L	0.80	1.80	$^{\mathrm{N}}/_{\mathrm{m}}$
Evaporation enthalpy	ΔH_{LG}	4800	6100	$^{\mathrm{kJ}}/_{\mathrm{kg}}$

4.2.3 Seam geometry

LaserCAD gives the user the possibility to choose between butt-, corner-, lap- and T-joint (see input window for seam geometry: Figure 4.7c on page 43). In the provided version of LaserCAD, the EB-model does not regard the gap between the joint faces (gap = 0 mm). Hence, regardless of which seam type is chosen, the simulation results do not change. Figure 4.18 shows four simulation results with the same input parameters but different chosen joint types. Only the displayed shape of the joint differs in the cross section view (blue lines in Figure 4.18).

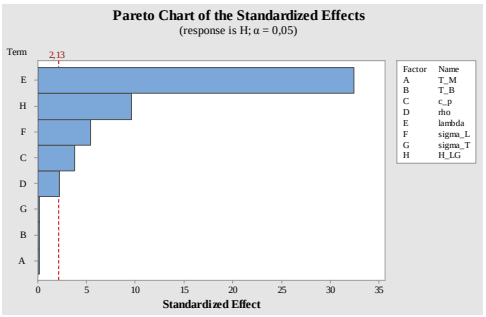

(a) *Pareto chart of standardised effects on penetration depth H*

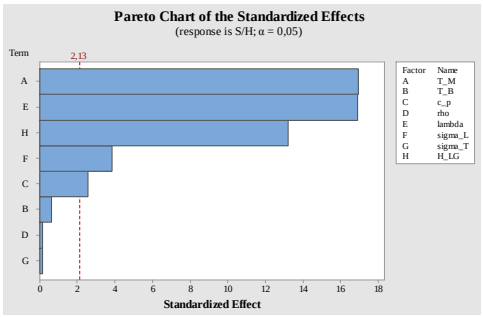

(b) *Pareto chart of standardised effects on fusion zone area per depth S/H*

Figure 4.16: *Pareto charts of the standardised effects on H and S/H to determine potentially important material properties [71]*

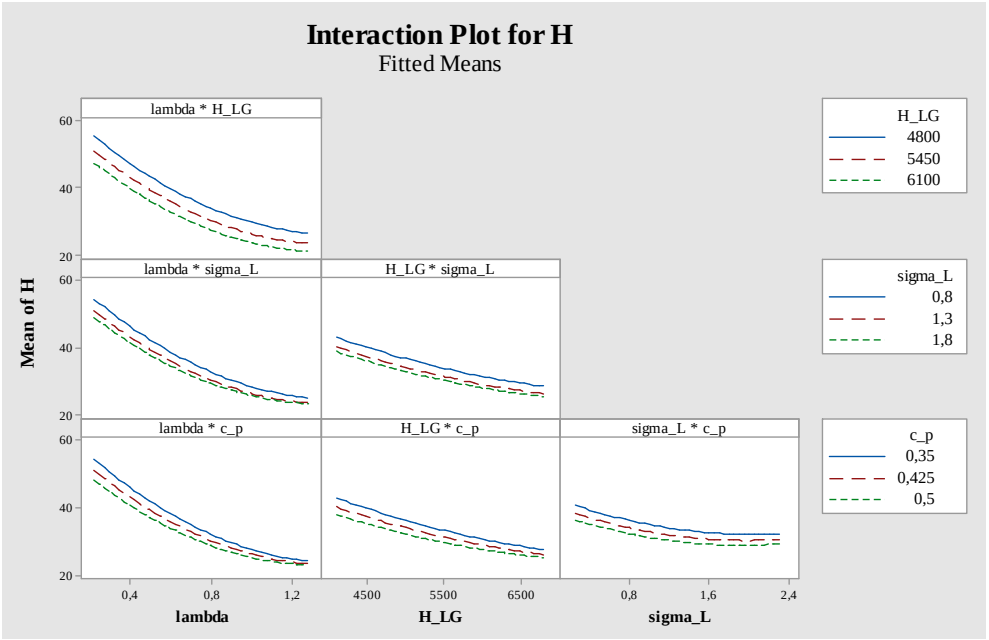

Figure 4.17: *Interaction plots for the penetration depth response H on the factors thermal conductivity λ, latent heat of evaporation ΔH_{LG}, surface tension σ_L and heat capacity c_p [71]*

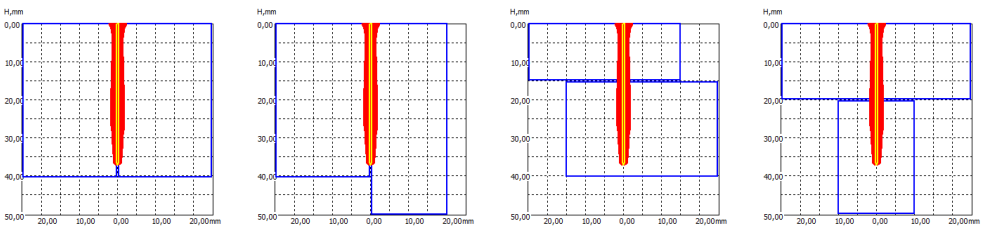

(a) *Butt-joint* (b) *Corner-joint* (c) *Lap-joint* (d) *T-joint*

Figure 4.18: *Simulation results of the cross section with different joint types*

Furthermore, changes of the specimen width input parameters b_i showed no influence on calculation results. Figure 4.19 shows three simulation results with altered workpiece widths. Except for the indicated blue line in the cross section, the results are not affected by the different widths.

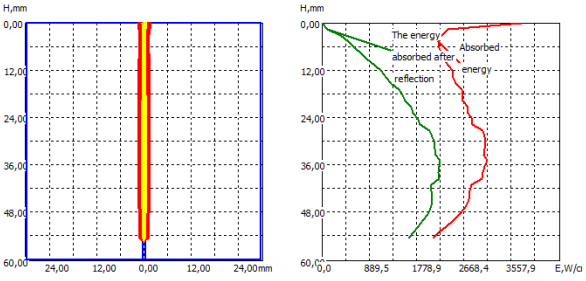

Absorbed Energy	14625 W	Radiation Power	15000 W
Evaporation Losses	185 W	WeldingSpeed	1,50 cm/sec
Reflection energy losses	55 W	Aperture	20,00 mm
Vapour flow speed	442,1 m/sec	Focal radius	0,200 mm
Wall temperature	2094 K	Focal distance	750,00 mm
Channel is	present	Focal exceeding	0,00 mm
Sample thickness	60,00 mm	Accelerate Voltage	150,0 kV
Depth	54,10 mm		
Width on the Surface	3,249 mm		
Width on the half of Depth	2,943 mm		
Melted zone square	102,09 mm^2		
Seam	butt joint		
Width in the root	2,439 mm		
Length of the bath	6,934 mm		
Keyhole radius on the surface	0,443 mm		
Material	Low-carbon steel	Marangony effect is	not considered

(e) *Simulation results with* $b_1 = 200\,\text{mm}$ *and* $b_2 = 200\,\text{mm}$

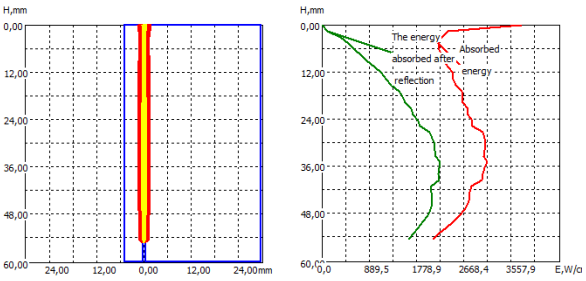

Absorbed Energy	14625 W	Radiation Power	15000 W
Evaporation Losses	185 W	WeldingSpeed	1,50 cm/sec
Reflection energy losses	55 W	Aperture	20,00 mm
Vapour flow speed	442,1 m/sec	Focal radius	0,200 mm
Wall temperature	2094 K	Focal distance	750,00 mm
Channel is	present	Focal exceeding	0,00 mm
Sample thickness	60,00 mm	Accelerate Voltage	150,0 kV
Depth	54,10 mm		
Width on the Surface	3,249 mm		
Width on the half of Depth	2,943 mm		
Melted zone square	102,09 mm^2		
Seam	butt joint		
Width in the root	2,439 mm		
Length of the bath	6,934 mm		
Keyhole radius on the surface	0,443 mm		
Material	Low-carbon steel	Marangony effect is	not considered

(f) *Simulation results with* $b_1 = 5\,\text{mm}$ *and* $b_2 = 200\,\text{mm}$

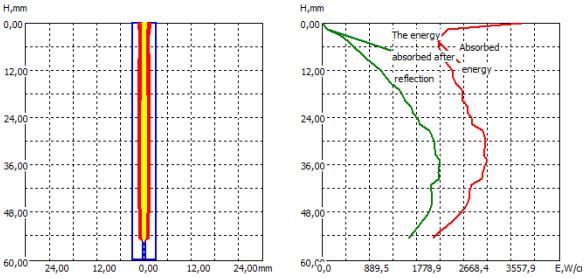

Absorbed Energy	14625 W	Radiation Power	15000 W
Evaporation Losses	185 W	WeldingSpeed	1,50 cm/sec
Reflection energy losses	55 W	Aperture	20,00 mm
Vapour flow speed	442,1 m/sec	Focal radius	0,200 mm
Wall temperature	2094 K	Focal distance	750,00 mm
Channel is	present	Focal exceeding	0,00 mm
Sample thickness	60,00 mm	Accelerate Voltage	150,0 kV
Depth	54,10 mm		
Width on the Surface	3,249 mm		
Width on the half of Depth	2,943 mm		
Melted zone square	102,09 mm^2		
Seam	butt joint		
Width in the root	2,439 mm		
Length of the bath	6,934 mm		
Keyhole radius on the surface	0,443 mm		
Material	Low-carbon steel	Marangony effect is	not considered

(g) *Simulation results with* $b_1 = 3\,\text{mm}$ *and* $b_2 = 3\,\text{mm}$

Figure 4.19: *Simulation results with different specimen widths* b_1 *(left from beam axis) and* b_2 *(right from beam axis)*

Moreover, an influence of the sample thickness h was investigated. The left picture in Figure 4.20 shows an EBW simulation with an achieved penetration depth H_0. As long as $h > H_0$, no differences are detected in the simulation output. When further decreasing the sample thickness, the values of absorbed energy P_a decreases as well, while evaporation losses P_v and reflection losses P_r remain constant. The diagram depicted in Figure 4.20 shows the amount of the transmitting power P_T in relation to the impinging beam power P. Transmitting power is beam power minus absorbed power and losses:

$$P_T = P - P_a - (P_v + P_r) \tag{4.6}$$

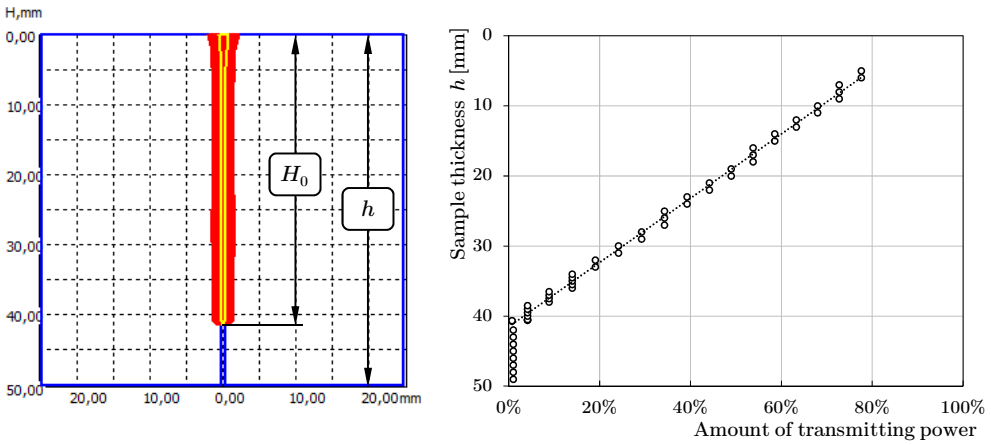

Figure 4.20: *Influence of the sample thickness h on the amount of the transmitting power P_T*

4.2.4 Heat transfer model

LaserCAD offers two different heat transfer models to calculate the temperature field arising during the welding process. A two dimensional and a three dimensional model, like mentioned in section 4.1.2 on page 43. Figure 4.21 shows an example of graphical outputs of an electron beam welding simulation carried out with both, the 2D- and the 3D-HTM. The result of the absorbed energy distribution, the keyhole shape and the achievable penetration depth remain unchanged, which is evident as the heat transfer model has no influence on the model of vapourisation and keyhole formation. The only disparity in the results is the width of the fusion zone, in x- as well as in y-plane.

Since the 2D-HTM solely allows heat flux normal to the cavity axis, it was expected, that the solution of the 3D-HTM leads to a narrower fusion zone. The additional heat flux in z-direction of the 3D-HTM, would lead to a heat loss compared to the 2D-model, thus to a decreasing seam width, especially in the bottom part of the weld. Nevertheless, the fusion zone calculated with the 3D-HTM is much bigger than the one of the 2D-HTM (Figure 4.21). And no matter what input parameters are used, all EB simulations show the same behaviour.

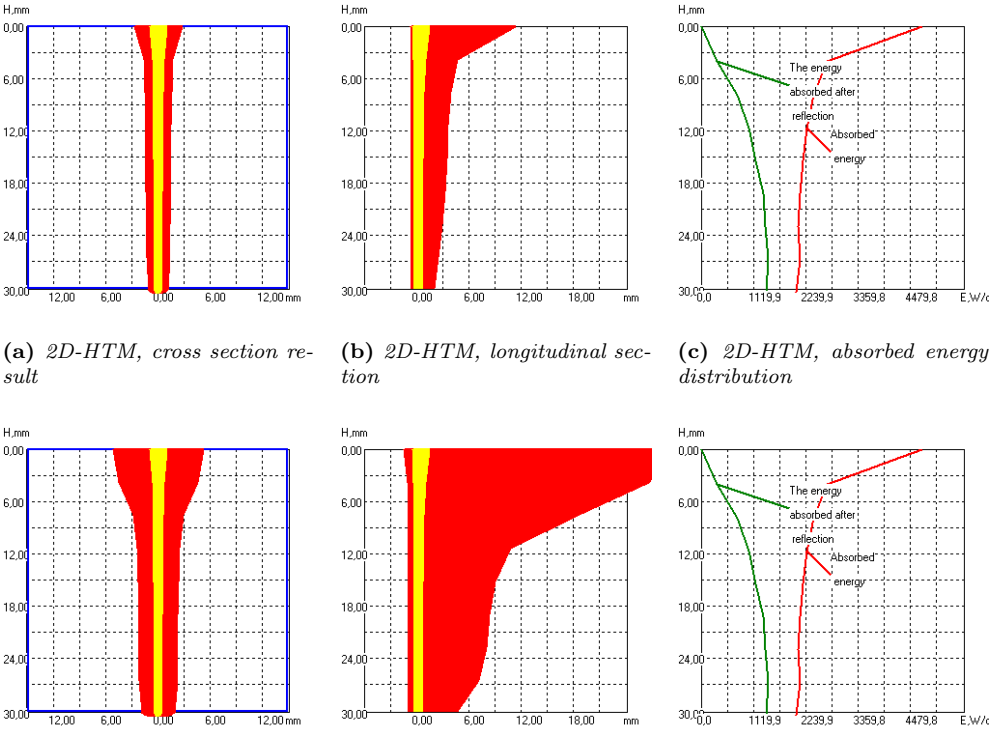

(a) *2D-HTM, cross section result*

(b) *2D-HTM, longitudinal section*

(c) *2D-HTM, absorbed energy distribution*

(d) *3D-HTM, cross section result*

(e) *3D-HTM, longitudinal section*

(f) *3D-HTM, absorbed energy distribution*

Figure 4.21: *Example solutions of an EBW simulation carried out with both, 2D- and 3D-heat transfer model*

For a better understanding, a comparison of two analytical solutions was done. The following equations show analytical solutions of heat sources based on the works of Rosenthal and Rykalin. With different simplifications like an assumed point heat source, no heat loss on surface, no temperature dependency of thermophysical material properties and neglection of latent heat, two cases of heat flow can be distinguished. Equation (4.7) represents a two dimensional heat flux in a thin plate and equation (4.8) represents a three dimensional heat flux in a thick specimen. [74, p. 222]

$$\text{2D-solution} \ldots \qquad \Delta T = \frac{E}{d \cdot \sqrt{4 \cdot \pi \cdot \lambda \cdot \rho \cdot c_p \cdot t}} \cdot \exp\left(\frac{-r^2}{4 \cdot a \cdot t}\right) \tag{4.7}$$

$$\text{3D-solution} \ldots \qquad \Delta T = \frac{E}{2 \cdot \pi \cdot \lambda \cdot t} \cdot \exp\left(\frac{-r^2}{4 \cdot a \cdot t}\right) \tag{4.8}$$

The temperature distribution at two different moments ($t = 0.08\,\text{s}$ and $0.2\,\text{s}$) is plotted in Figure 4.22. Table 4.10 gives the used values for these calculations. As expected, the 3D curve (red) is narrower, which would lead to a narrower fusion zone.

It has to be noticed, that equation (4.7) is only valid for a thin plate. With increasing thickness d, the temperature distribution of the 2D-solution changes drastically. The graphs marked with "$*$" are calculated for $d = 20\,\text{mm}$. As can easily be seen, the temperature ΔT is inversely proportional to the thickness of the plate d with limit 0:

$$\lim_{d \to \infty} \Delta T = 0$$

Table 4.10: *Values for the calculation of analytical solutions of point heat sources according to equations* (4.7) *and* (4.8)

Attribute		Value	Unit	Note
Beam power	P	2000	W	
Welding speed	v	10.0	$^{mm}/_{s}$	
Energy input per unit length	E	200	$^{J}/_{mm}$	
Specimen thickness	d	4.00	mm	only for 2D
Heat conductivity	λ	3.69	$^{W}/_{(cm\ K)}$	
Heat capacity	c_p	0.44	$^{J}/_{(g\ K)}$	
Thermal diffusivity	a	0.94	$^{cm^2}/_{s}$	$a = {}^{\lambda}/_{(c_p \rho)}$

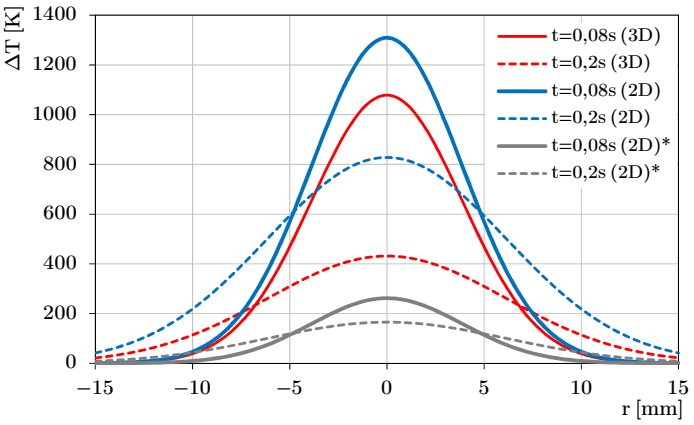

Figure 4.22: *Temperature distribution of analytical solutions for point heat sources based on* Rosenthal *and* Rykalin*; Input values: Table 4.10; Graphs marked with "∗": $d = 20\,\text{mm}$*
2D. . . . . equation (4.7)
3D. . . . . equation (4.8)

For the deep and narrow fusion zone occurring in electron beam welding, such a point heat source is not a suitable model to calculate the heat flux. Nevertheless, some similarities to LaserCAD's electron beam model can be illustrated. In Figure 4.23, the heat flux is schematically depicted for both, LaserCAD's HTMs and the equations by Rosenthal and Rykalin. Similar to the solutions of Rosenthal and Rykalin, LaserCAD's HTM does not take heat flux in z-direction into account in the 2D case. In the 3D case, heat flux in all directions is calculated.

But besides all these things in common, the layer by layer calculation of LaserCAD is an important difference compared to the point heat sources of Rosenthal and Rykalin. Figuratively speaking in each layer either a line heat source (2D-HTM) or a point heat source (3D-HTM) is modelled. This arrangement of several point (or line) heat sources along the keyhole (one for each layer) is used by LaserCAD's HTMs to calculate the deep and narrow fusion zone of the electron beam welding process.

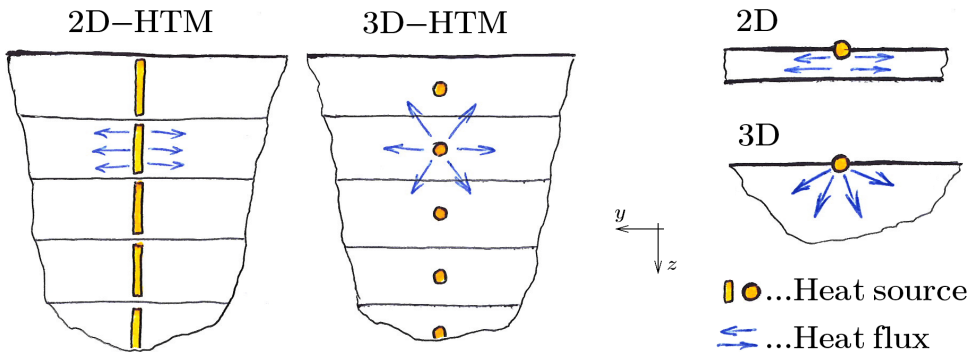

(a) *LaserCAD's heat transfer models* **(b)** Rosenthal *and* Rykalin

Figure 4.23: *Schematic comparison of the heat flux in LaserCAD's heat transfer models and the equations* (4.7) *and* (4.8) *from* Rosenthal *and* Rykalin

Further analysis of differences in 2D- and 3D-HTM results showed discrepancies between the thermal cycle output and the fusion zone results. In Figure 4.24a, several thermal cycles are plotted from points taken alongside the solid-liquid boundary of the 2D- and the 3D-HTM solution indicated with "⊕" (Figures 4.24b and 4.24c). The melting temperature used for this very simulation is indicated in the diagram. While the TC taken from the 2D-solution reaches the melting point with its maximum temperature, T_{max} of the thermal cycles from the 3D-solution are ~ 800 K too low to reach T_M. In other words, the reached temperature in the indicated solid-liquid boundary of the 3D-HTM output is too low to coexist with molten material.

Table 4.11: *Input parameters for 2D- and 3D-HTM thermal cycle analysis*

Beam and geometry parameters		Material parameters	
U_A	120 kV	T_M	1810 K
P	7.2 kW	T_B	3133 K
v	1 $^{\text{cm}}/_{\text{s}}$	c_p	0.465 $^{\text{J}}/_{(\text{g K})}$
A	1.12 cm	ρ	7.83 $^{\text{g}}/_{\text{cm}^3}$
r_0	0.0146 cm	λ	0.41 $^{\text{W}}/_{(\text{cm K})}$
L_F	75 cm	σ_L	1.8 $^{\text{N}}/_{\text{m}}$
f_P	0 cm	σ_T	0.02 $^{\text{mN}}/_{(\text{m K})}$
h	30 mm	ΔH_{LG}	834.4 $^{\text{kJ}}/_{\text{kg}}$

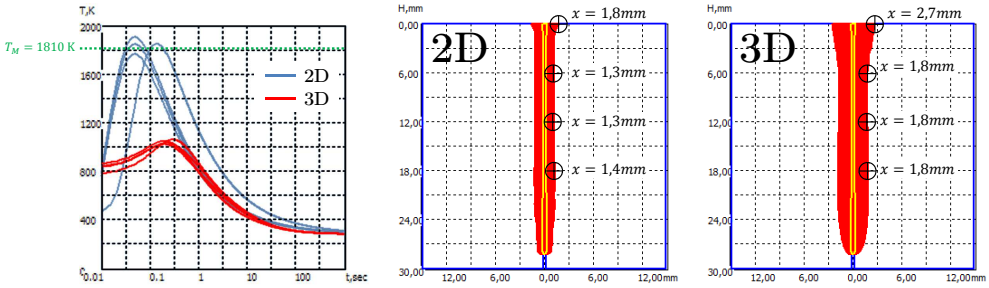

(a) *Thermal cycle output of several points alongside the solid-liquid boundary*

(b) *Points of thermal cycle output; 2D-HTM*

(c) *Points of thermal cycle output; 3D-HTM*

Figure 4.24: *Study of thermal cycles alongside solid-liquid boundary of an electron beam welding simulation at the cross section plane calculated with the 2D- and 3D-heat transfer model*

In Figure 4.25, thermal cycle outputs of points fulfilling the condition $T_{max} = T_M$ are taken from the 3D-HTM solution. As indicated in Figure 4.25c, the points move to the centre of the seam. Assuming that these points mark the "correct" solid-liquid boundary, the seam of the 3D-HTM is narrower than the one from the 2D-HTM.

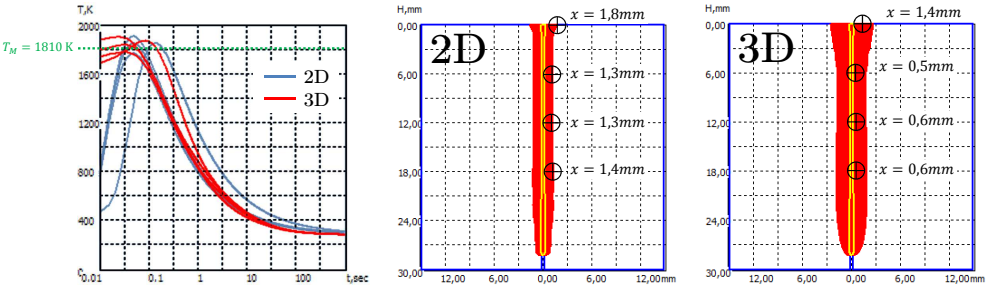

(a) *Thermal cycle output of several points with condition $T_{max} = T_M$*

(b) *Points of thermal cycle output; 2D-HTM*

(c) *Points of thermal cycle output; 3D-HTM*

Figure 4.25: *Study of thermal cycles with $T_{max} = T_M$ of an electron beam welding simulation at the cross section plane calculated with the 2D- and 3D-heat transfer model*

Similar to Figure 4.25, the same investigation was done using LaserCAD's laser welding model. Figure 4.26 shows, that the model shows reasonable behaviour. The seam calculated with the 3D-HTM is narrower, especially at the bottom part and the thermal cycle outputs alongside the fusion zone boundary fulfil the condition $T_{max} = T_M$.

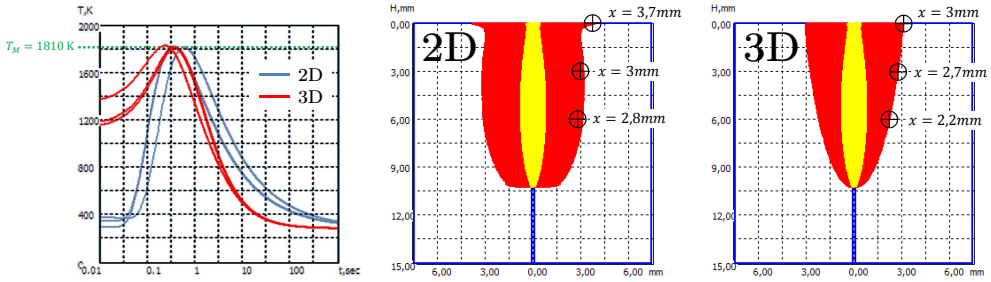

(a) *Thermal cycle output of several points with condition* $T_{max} = T_M$

(b) *Points of thermal cycle output; 2D-HTM*

(c) *Points of thermal cycle output; 3D-HTM*

Figure 4.26: *Study of thermal cycles with* $T_{max} = T_M$ *of a laser beam welding simulation at the cross section plane calculated with the 2D- and 3D-heat transfer model*

The coordinates of several points fulfilling $T_{max} = T_M$ were transfered to the CAD software CATIA V5 R19 [75] and boundaries along these points were drawn. The area laying within these boundaries S_l was measured. The results are juxtaposed in Figure 4.27. The fusion zone calculated with the 2D-HTM shows a deviation between LaserCAD's result S_{LC} and the measured result S_l of ~ 10 %. Due to the following reasons, this deviation is neglectable.

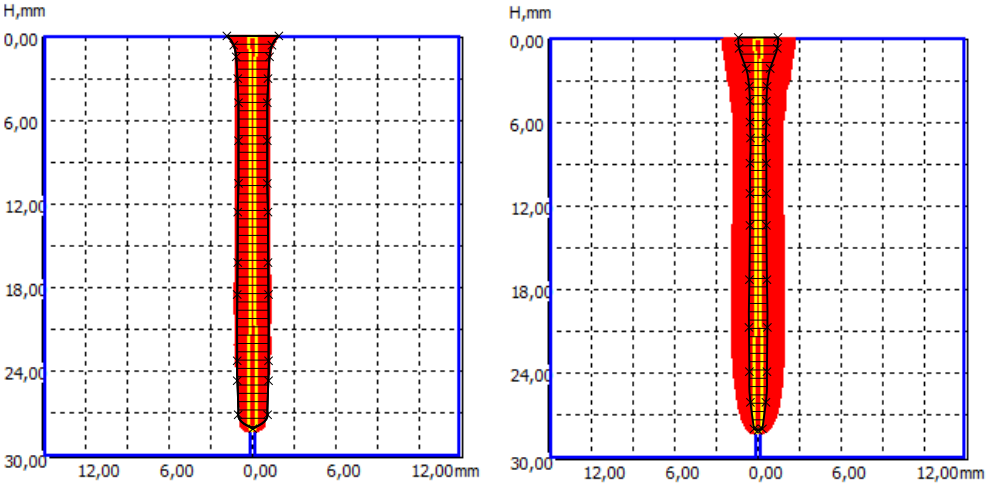

(a) *2D-HTM;* $S_{LC} = 65.7\,\text{mm}^2$*;* $S_l = 59.6\,\text{mm}^2$

(b) *3D-HTM;* $S_{LC} = 102.05\,\text{mm}^2$*;* $S_l = 35.6\,\text{mm}^2$

Figure 4.27: *Comparison of the area* S_l *fulfilling the condition* $T_{max} \geq T_M$ *for cross section results calculated with the 2D- and the 3D-heat transfer model*

The thermal cycle results are outputted by clicking on certain pixels in the cross section result, which has a rather coarse resolution of 272×272 px. In present matter, with an area representing a 30×30 mm section, a resolution of $> 0.1\,\text{mm}/\text{px}$ occurs. Moreover, the thermal cycle output has the same resolution, leading to a range of temperature variations of ~ 15 K within the line thickness of the time-temperature curve.

Looking at Figure 4.27b, a considerable deviation can be noticed. The measured area S_l fulfilling the condition $T_{max} \geq T_M$ is significantly smaller than the result

outputted by LaserCAD. Comparing the measured area of the 2D- and the 3D-HTM, the 3D result appears about 40 % smaller than the 2D ones. Moreover it can be said, that the 3D-HTM's fusion zone becomes more nail-shaped.

4.2.5 Marangoni effect

LaserCAD gives the user the opportunity to select or deselect the consideration of the MARANGONI effect. This effect describes a mass flow in the molten bath depending on the surface tension temperature gradient $\frac{\mathrm{d}\sigma}{\mathrm{d}T}$, in our case linear approximated with σ_T. Several simulations with different materials and different values for σ_T were made in order to detect the influence in LaserCAD's output. Calculations with the laser beam model showed, that with considerated MARANGONI convection the weld bath gets broader in the upper area and narrower in the lower area of the seam, like described in [57]. On the other hand, calculations with the EB-model showed no influence at all, regardless of the used input paramteres.

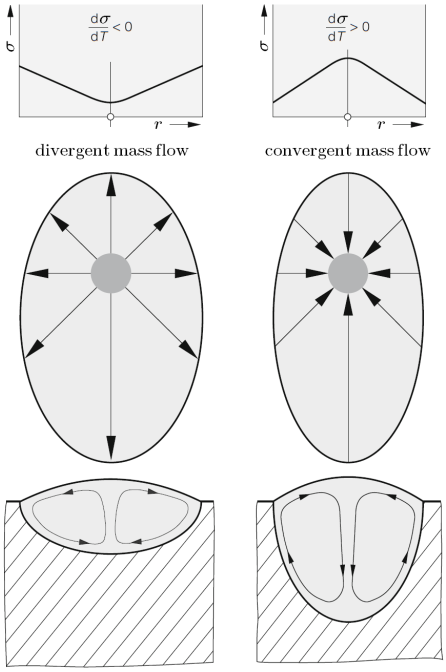

Figure 4.28: *Mass flow in the weld bath owing to the temperature gradient of the surface tension $\frac{\mathrm{d}\sigma}{\mathrm{d}T}$; adapted from [3]*

left .... $\frac{\mathrm{d}\sigma}{\mathrm{d}T} < 0 \quad \rightarrow \quad$ *divergent mass flow*

rigth ... $\frac{\mathrm{d}\sigma}{\mathrm{d}T} > 0 \quad \rightarrow \quad$ *convergent mass flow*

4.2.6 Oscillating figure approach

LaserCAD's electron beam model assumes a static beam, hence no beam oscillating (Figure 2.17) is simulated. In [1], solely weldings with oscillating beams were done (Table 3.1) in order to achieve a broader fusion zone and a better mouldability of the melt to prevent run-outs and root craters. With an oscillating beam, the impinging beam power is not concentrated at a single spot and can be distributed over a broader area, leading to a wider fusion zone and decreased penetration depth [37, p. 50ff]. Depending on the chosen figure, the amplitude in x- and y-direction and the oscillation frequency, stirring-effects, with arising convective fluxes in the weld bath may occur.

Although LaserCAD's EB-model is limited on point figures, an approach by changing the focal radius r_0 and/or the beam power P was attempted. The idea was to adjust the energy distribution of the impinging beam to simulate welds performed

with oscillating figures. Since errors with simulations of Cu-DHP occurred (Section 4.3.1) and experimental data with 1.4313 are available at IWS, the following simulations were done for this very material.

Figure 4.29 shows a section cut through a steel specimen with EB welds made with parameters listed in Table 4.12.

Table 4.12: *Welding parameters and simulation input parameters for 1.4313 bead on plate welds from C. Wiednig [76]; Material: Steel 1.4313; Specimen thickness:* 30 mm*; Oscillation figure: Ellipse (*dx = 1 mm, dy = 0.5 mm, f = 1 kHz*)*

Material parameters			Beam and geometry parameters						
			Seam	1	2	3	4	5	
T_M	1725	K	U_A	150	150	150	150	150	kV
T_B	3133	K	P	9.00	9.00	12.00	15.00	15.00	kW
c_p	0.46	J/(g K)	v	18	12	15	12	18	mm/s
ρ	7.70	g/cm^3	A	1.15	1.15	1.15	1.15	1.15	cm
λ	0.25	W/(cm K)	r_0	0.016	0.016	0.016	0.016	0.016	cm
σ_L	1.82	N/m	L_F	75	75	75	75	75	cm
σ_T	0.034	mN/(m K)	f_P	0	0	0	0	0	cm
ΔH_{LG}	6092.4	kJ/kg							

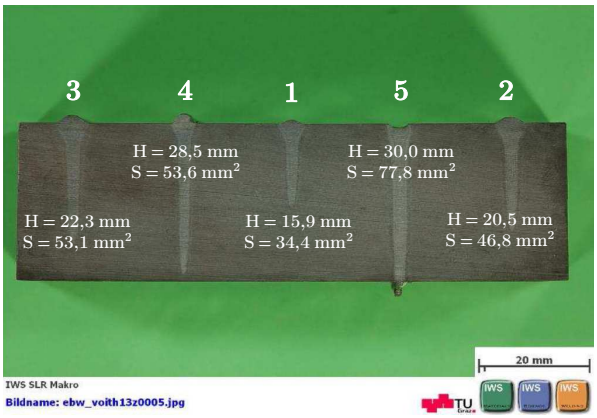

Figure 4.29: *Section cut of bead on plate welds through 1.4313 steel specimen with a thickness of* 30 mm *from [76] with measured penetration depth H and fusion zone area S*

As described in [37, p. 53], excluding x-oscillation, beam oscillation leads to a decreased penetration depth compared to welds carried out without oscillating beam. An increasing of the beam current and/or a decreasing of the welding speed is mentioned to compensate this effect.

Starting from parameters listed in Table 4.12, first simulations without adjustment of the focal radius r_0 or the beam power P lead to the expected consequence, that the penetration depth predicted by the simulation is up to ~ 150 % greater than the experimental achieved depth (Figure 4.30).

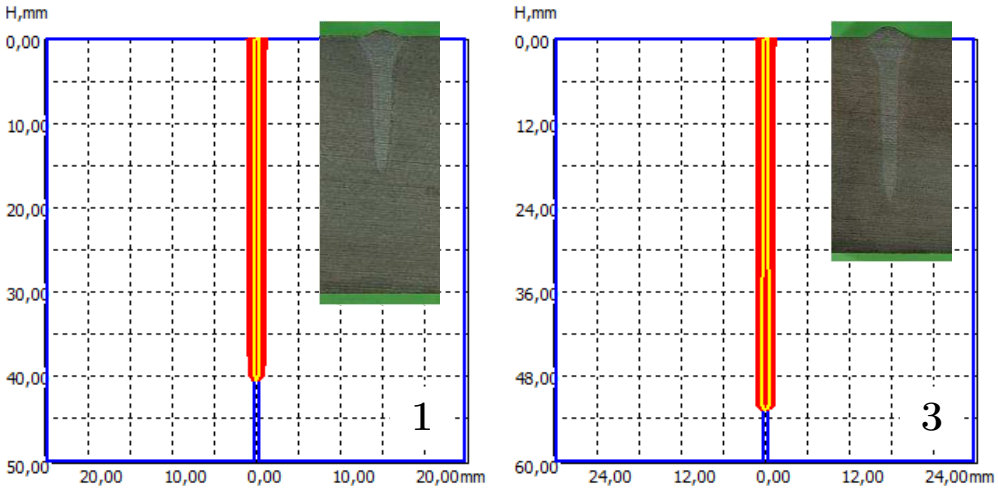

(a) *Simulation result versus experimental result for seam No. 1*

(b) *Simulation result versus experimental result for seam No. 3*

Figure 4.30: *Examples of simulation results without adaption of beam power and/or focal radius*

Adjustment of focal radius

The mere adaption of focal radius turned out to be unrewarding. For three different seams (No. 1, 3 and 4), three different focal radii for suitable results of penetration depth H are necessary (Figure 4.31). Hence it can be assumed that mere adjustment of the focal radius r_0 is insufficient for simulating welds with oscillating beam.

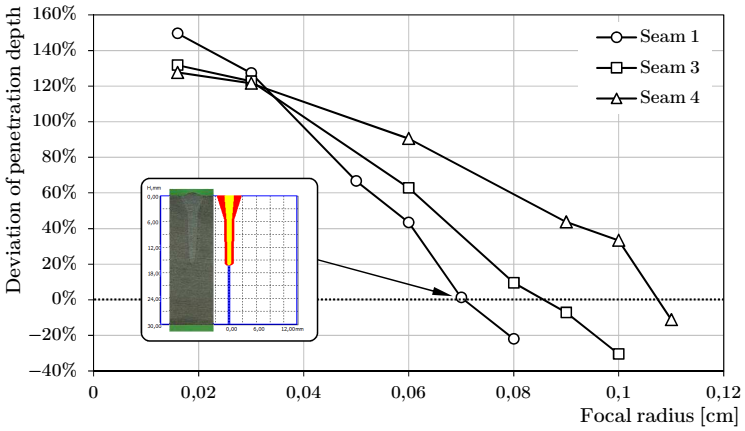

Figure 4.31: *Deviation of penetration depth H versus focal radius input r_0 for seams No. 1, 3 and 4; The graphic within shows one example cross section result for seam No. 1.*

Adjustment of focal radius, beam power and acceleration voltage

In the next step, the power of the impinging beam was adjusted as well. In Figure 4.32, the graph with points indicated as "◇", represents values with mere adjustment of focal radius to $r_0 = 0.5\,\text{mm}$. Graphs "□" and "×" indicate simulation results with adjusted beam power by factor $\eta < 1$ according to equation (4.9).

$$\widetilde{P} \quad = \quad P \cdot \eta \tag{4.9}$$

The mere adaption of the beam power P, without adaption of the acceleration voltage U_A means physically the mere decrease of the beam current I_B. To achieve a decrease of the acceleration voltage and the beam current on the same level, the acceleration voltage needs to be adjusted according to equation (4.11).

$$\widetilde{P} = \widetilde{U}_A \cdot \widetilde{I}_B$$

$$\widetilde{I}_B = I_B \cdot \sqrt{\eta} \tag{4.10}$$

$$\widetilde{U}_A = U_A \cdot \sqrt{\eta} \tag{4.11}$$

The graphs "△" and "○" represent results with adjusted beam power and additionally adjusted acceleration voltage (equations (4.9) and (4.11)).

The best results with a maximum deviation of 11.6 % for seam No. 4 and a minimum deviation of 2.2 % for seam No. 3 were achieved by adjusting beam power and acceleration voltage with factor $\eta = 0.7$ and a focal radius $r_0 = 0.6\,\text{mm}$.

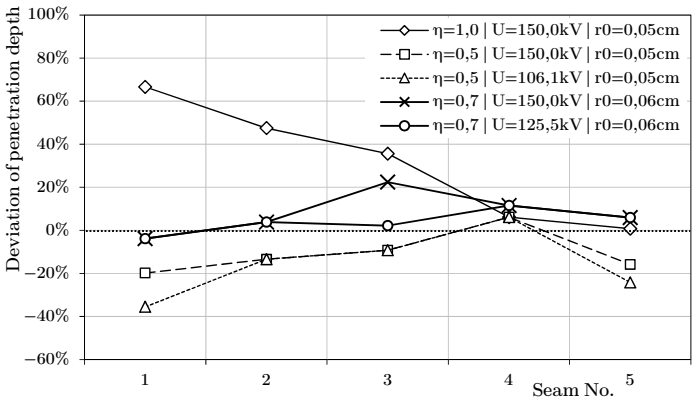

Figure 4.32: *Deviation of penetration depth H for seams No. 1...5 (specimen thickness 30 mm) with different input values for P, U_A and r_0*

For the same material, welds carried out on a specimen with a thickness of 80 mm have been provided by [76]. Again, theses welds were made with the same oscillating figure as used for the specimen of 30 mm thickness. The welding parameters are listed in Table 4.13 and a section cut is presented in Figure 4.33.

Table 4.13: *Welding parameters for bead on plate welds from C. Wiednig [76]; Material: Steel 1.4313; Specimen thickness:* 80 mm*; Oscillation figure: Ellipse (*$\mathrm{d}x$ = 1 mm, $\mathrm{d}y$ = 0.5 mm, f = 1 kHz*)*

Seam		1	2	3	4	5
U_A	kV	150	150	150	150	150
I_B	mA	150	170	150	190	190
v	$^{\text{mm}}/_{\text{s}}$	15	13	11	15	11
P	kW	22.50	25.50	22.50	28.50	28.50
E	$^{\text{kJ}}/_{\text{cm}}$	15.00	19.60	20.50	19.00	25.90

The same parameters leading to useful results for the 30 mm specimen were taken for the simulations, meaning that the focal radius was set to $r_0 = 0.6\,\text{mm}$ and the beam power as well as the acceleration voltage were adapted with $\eta = 0.7$ according to equations (4.9) and (4.11).

Figure 4.34a displays these results marked with "○". For all seams the deviation was > 14 % with a maximum deviation of 23.6 % for seam No. 5. Further adjustment

Figure 4.33: *Section cut of bead on plate welds through 1.4313 steel specimen with a thickness of* 80 mm *from [76] with measured penetration depth H and fusion zone area S*

of η and r_0 lead to less deviations. Results with fewer deviations were achieved by further decreasing η to 0.6, indicated with "□". For $\eta = 0.45$ and $r_0 = 0.2\,\text{mm}$, best results with depth deviations $< 5\,\%$ were achieved ("●"). Figure 4.34b compares the cross section outcome for the last mentioned parameters with experimental data.

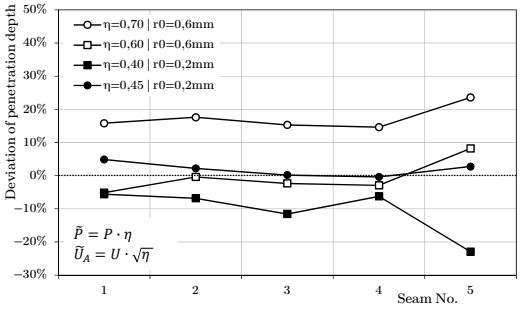

(a) *Deviation of penetration depth H for seams No. 1...5 with different input of P, U_A and r_0*

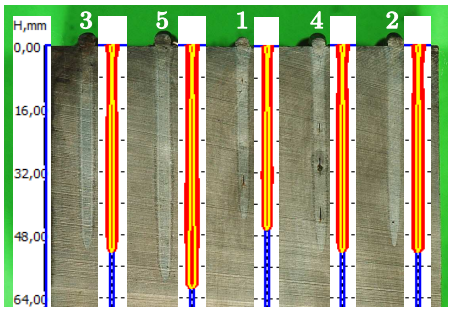

(b) *Experimental data versus simulation output for $\eta = 0.45$ and $r_0 = 0.2\,\text{mm}$*

Figure 4.34: *Deviation of penetration depth and examples of simulation results versus experimental data for the* 80 mm *steel specimen*

4.2.7 Point figure weldings and focal position influence

In order to investigate the accuracy when simulating experiments made without beam oscillation and to study the influence of the focal position f_P, welds on 1.4313 were done (Figure 3.11 on page 37). The weldings were realised with parameters according to Table 3.5 on page 36.

First simulations were done only for seams with focal position lying on the surface ($f_P = 0\,\text{mm}$) with material parameters from Table 4.12 (page 65), beam parameters U_A and P according to Table 3.5 as well as $r_0 = 0.02\,\text{cm}$, $A = 0.8\,\text{cm}$, $L_f = 75\,\text{cm}$ and a specimen thickness of $h = 50\,\text{mm}$. The results, compared to the experiments, are depicted in Figure 4.35a and show great deviations in penetration depth H ($\sim 10\,\%\ldots 90\,\%$) and fusion zone area S ($\sim -16\,\%\ldots +186\,\%$), especially for seams No. 5 and 13. Seams indicated with "☆" reached full penetration in the simulation, meaning the indicated deviations appear undersized because the penetration depth from the simulation is limited to the inputted specimen width h.

In order to decrease the depth deviation, the focal radius was increased to 0.08 cm (Figure 4.35b). The results still have a high level of deviation in depth of up to 83 % and deviations in area of up to 112 %.

A decrease of power and acceleration voltage according to equations (4.9) and (4.11) with $\eta = 45\,\%$ lead to results depicted in Figure 4.35c. Except of the area deviation of seam No. 5 (85 %), the deviation is sharply reduced, especially for penetration depth results.

In Figure 4.35d, results with adapted material properties are shown. Temperature profiles for heat capacity and thermal conductivity, calculated for this very material with J-MAT PRO, were provided by [76]. At $T \sim 1500\,°\mathrm{C}$, values for heat capacity of $c_p \sim 1\,\mathrm{J/(g\,K)}$ and thermal conductivity $\lambda \sim 0.36\,\mathrm{W/(cm\,K)}$ are reached. The depth deviation is reduced to values around maximum 30 % while the area deviation still remains on a high level.

Seam No. 5 attracts attention owing to its high area deviations of 85 % to 186 %. With 7.2 kW, this seam was welded with the lowest beam power. As will be presented later on (see Figure 4.38 on page 71), seams with higher beam power tend to lower area deviation. This leads to the assumption, that a certain input parameter set-up for the calculation is only valid for a certain parameter range.

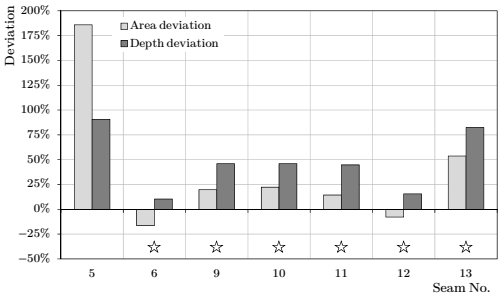

(a) *First try*

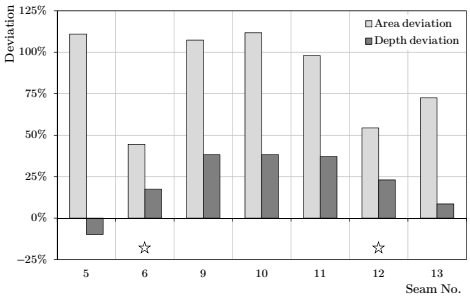

(b) *Like* (a) *with increased* $r_0 = 0.08\,\mathrm{cm}$

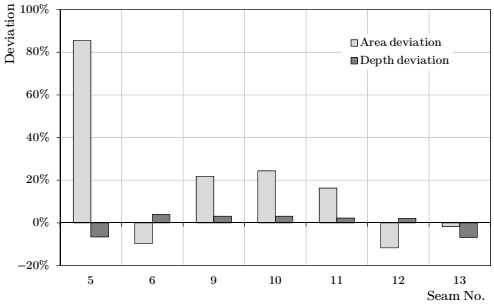

(c) *Like* (a) *with decreased* P *and* U_A *according to equations* (4.9) *and* (4.11) *with factor* $\eta = 45\,\%$

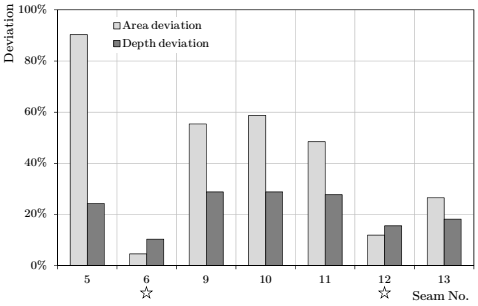

(d) *Like* (a) *with adapted material properties* $c_p = 1\,\mathrm{J/(g\,K)}$ *and* $\lambda = 0.36\,\mathrm{W/(cm\,K)}$

Figure 4.35: *Deviation of depth* H *and fusion zone area* S *for different input properties for seams with focal position on surface* $f_P = 0\,\mathrm{mm}$*; Results marked with " ☆" reached full penetration in simulation*

All described adaptations of input parameters lead to a reduction of deviations. From the physical point of view, a change of the material properties to values near the melting point seems legit. Adjustments of focal radius, beam power and acceleration

voltage in such a strong way, however, are unrealistic and are in no way whatsoever connected to the experimental data.

For these beam parameters with $U_A = 150\,\mathrm{kV}$ and $I_B = 48\,\mathrm{mA} \ldots 132\,\mathrm{mA}$, measurements of beam emittance ε have failed [46]. Hence a deviation to the assumed focal radius of $r_0 = 0.02\,\mathrm{cm}$ is plausible.

Moreover, the adaption of the beam power with corresponding adaption of acceleration voltage can be reasonable when comparing the simulation with the experiment. LaserCAD does not simulate the formation of a weld crown, but, looking at Figure 3.11 (page 37), pronounced weld crowns can be recognised in experimental data. A part of the impinging beam power is therefore used for the formation of the weld crown, hence unused for the fusion zone beneath the upper surface. This difference could be compensated by the adaption of the power P and the acceleration voltage U_A.

According to Figure 4.36, the area of the weld crown S_C and the whole fusion zone were measured. The factor η was calculated with equation (4.12):

$$\eta \quad = \quad 1 - \frac{S_C}{S} \tag{4.12}$$

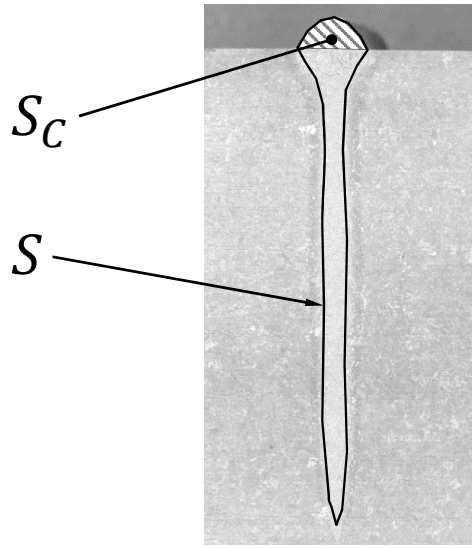

Figure 4.36: *Estimation of power loss factor η due to weld crown forming*

S_C . . . . . *Weld crown area*
S . . . . . *Fusion zone area*

An average value of $\eta \approx 88\,\%$ was found. The adaption of power with a corresponding adaption of acceleration voltage according to equations (4.9) and (4.11) in combination with material properties c_p and λ at $T \approx 1500\,^\circ\mathrm{C}$ and an adaption of the focal radius to $r_0 = 0.035\,\mathrm{cm}$ lead to results depicted in Figure 4.37. Except for seams number 5 and 13 with rather low beam power, the penetration depth result is with deviations of $-2.8\,\% \ldots +2.4\,\%$ very accurate. Nevertheless, rather high deviations in fusion zone area are still present.

In the next step, welds with the beam focus above and underneath the surface were taken into account as well. The values for the focal position listed in Table 3.5 are given with the unit mA, which is equal ΔI_L, the difference of the lens current compared to the current with the focus on the upper specimen surface. Converted to a length, 1 mA is approximately 1 mm at $U_A = 150\,\mathrm{kV}$ [76]. For seams with focal position $f_P \neq 0\,\mathrm{mm}$ the value for focal distance $L_F = 75\,\mathrm{cm}$ had to be changed correspondingly to $L_F = (75\,\mathrm{cm} - f_P)$, in order to simulate proper beam conditions (see Figure 4.7a).

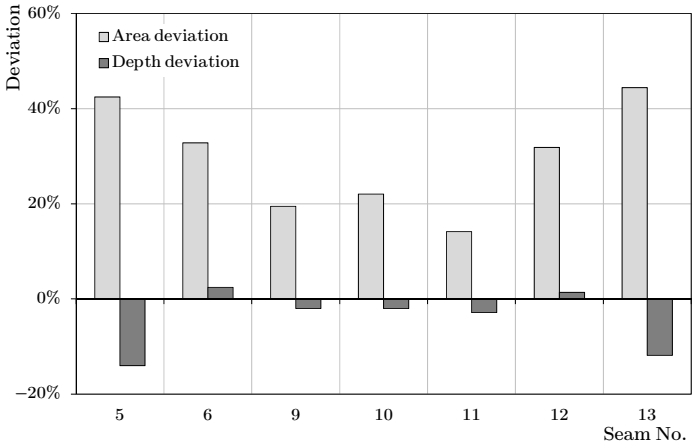

Figure 4.37: *Deviation of depth H and fusion zone area S with adapted P and U_A by factor $\eta = 0.88$ as well as c_p and λ for $T \approx 1500\,°\mathrm{C}$ and $r_0 = 0.035\,\mathrm{cm}$ for seams with focal position on surface*

The results for all seams are depicted in Figure 4.38. Besides deviation bars of depth and the fusion zone area, a graph of the experimental beam power is indicated. The results concerning the penetration depth of seams with lower beam power tend to have a higher deviation than seams welded with higher power.

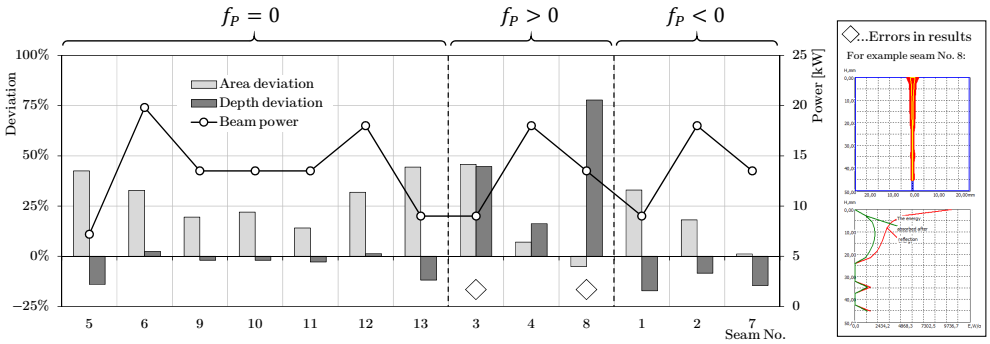

Figure 4.38: *Beam power of experiments and deviation of depth H and fusion zone area S with adapted P and U_A by factor $\eta = 0.88$ as well as c_p and λ for $T \approx 1500\,°\mathrm{C}$ and $r_0 = 0.035\,\mathrm{cm}$; Seams marked with " ◇" showed errors in absorbed energy graph as exemplary depicted in the right box for seam No. 8*

Seams with $f_P \neq 0\,\mathrm{mm}$ showed higher deviations in penetration depth than seams with normal focus position. Seams 3 and 8 of the over-focused welds ($f_P > 0\,\mathrm{mm}$) showed errors in the results. The calculated penetration depth of under-focused seams ($f_P < 0\,\mathrm{mm}$) is up to 17 % too small, compared to the experiments. The simulation of these seams without consideration of the focal offset, hence $f_P = 0\,\mathrm{mm}$, comes to results marked with "✻" in Figure 4.39. The errors for seams 5 and 9 disappear. The fusion zone area increases for all seams (Figure 4.39a), the deviation of penetration depth increases for over-focused seams and remains quite constant for seams with negative focus positions (Figure 4.39b).

Figure 4.40 juxtaposes metallographic data from experiments and cross section results of numerical simulations.

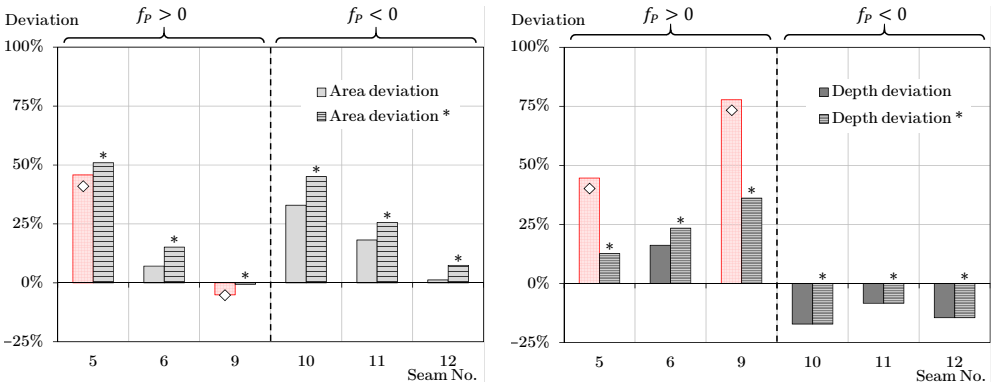

(a) *Area deviation* **(b)** *Depth deviation*

Figure 4.39: *Deviation of depth H and fusion zone area S for seams with focal position above or below surface $f_P \neq 0\,\mathrm{mm}$ calculated with f_P according to Table 3.5 and calculated with $f_P = 0\,\mathrm{mm}$ indicated with "✻"; Results marked with "◇" showed errors in absorbed energy graph*

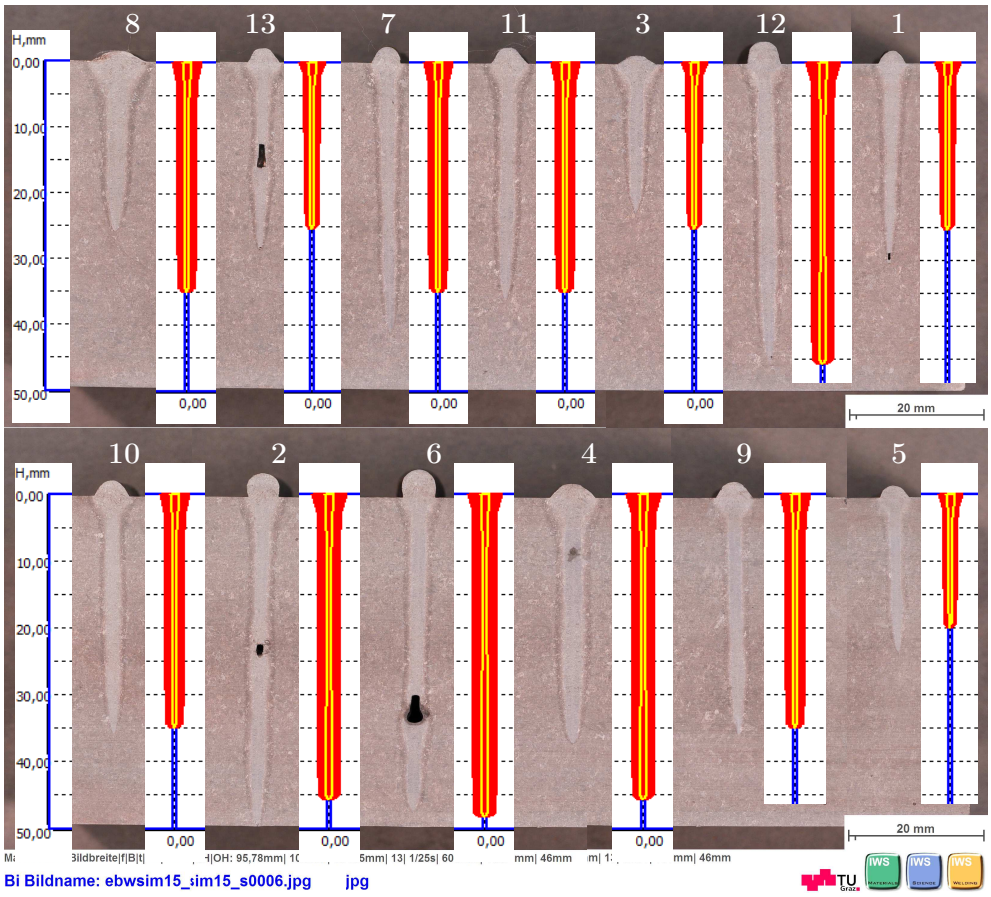

Figure 4.40: *Metallographic data versus cross section results of point figure welds on 1.4313; P and U_A adapted by factor $\eta = 0.88$ as well as c_p and λ for $T \approx 1500\,^{\circ}\mathrm{C}$ and $r_0 = 0.035\,\mathrm{cm}$; all seams calculated with normal focus position $f_P = 0\,\mathrm{mm}$*

4.3 EBW simulation of copper materials

The following pages will give an excerpt of the numerical simulations carried out with LaserCAD for this project. Numerous simulations have been done, and it is neither possible, nor target-aimed to show all of them in this work. Nevertheless, the presented results will give a representative documentation of the outcome.

If not denoted otherwise, the following calculations are realised using the 2D-HTM due to the problems with the 3D-heat transfer model as described in Section 4.2.4 (page 58).

4.3.1 Cu-DHP

After a brief overview of simulations conducted for welds carried out with oscillating beam from [1], the focus is laid on simulation of the point figure welds presented in Figure 3.3 (page 31).

First simulations of beam figure welds

The input parameters, used for the first calculations with the highly conductive copper material Cu-DHP are listed in Table 4.14. The beam parameters are based on a full penetration bead on plate weld from [1] with the seam ID *SF-D1-Naht1* (see Table 3.1 on page 30). The values for aperture A and focal radius r_0 were calculated with measured ε, θ_C and L_C for $U_A = 120\,\mathrm{kV}$ and $I_B = 80\,\mathrm{mA}$ (Table 4.4 on page 49). For the material properties, values at room temperature were taken into account.

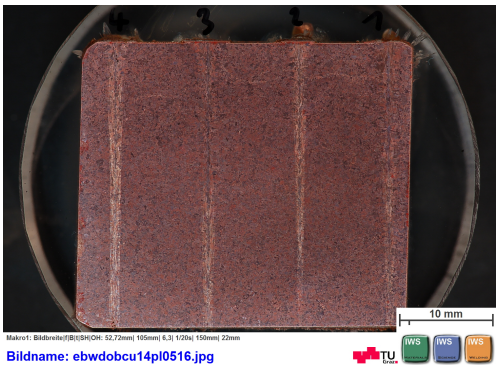

Figure 4.41: *Section cut of full penetration bead on plate welds through a Cu-DHP specimen of* 30 mm *thickness from [1]*

Left to right: SF-D1-Naht1 SF-D1-Naht2 SF-D1-Naht3 SF-D1-Naht4

Table 4.14: *Input parameters for Cu-DHP seam SF-D1-Naht1*

Beam and geometry parameters		Material parameters	
U_A	150 kV	T_M	1357 K
P	18 kW	T_B	2835 K
v	1 $^{\mathrm{cm}}/_{\mathrm{s}}$	c_p	0.444 $^{\mathrm{J}}/_{(\mathrm{g\ K})}$
A	1.15 cm	ρ	8.94 $^{\mathrm{g}}/_{\mathrm{cm}^3}$
r_0	0.016 cm	λ	3.69 $^{\mathrm{W}}/_{(\mathrm{cm\ K})}$
L_F	75 cm	σ_L	1.29 $^{\mathrm{N}}/_{\mathrm{m}}$
f_P	0 cm	σ_T	0.234 $^{\mathrm{mN}}/_{(\mathrm{m\ K})}$
h	30 mm	ΔH_{LG}	4826.9 $^{\mathrm{kJ}}/_{\mathrm{kg}}$

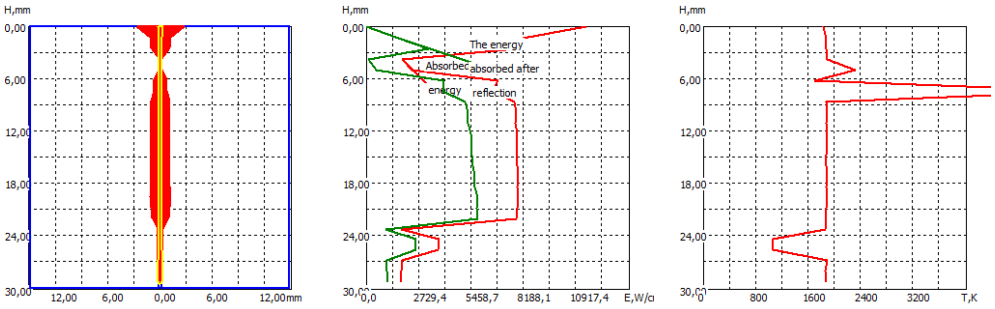

(a) *Cross section plane* **(b)** *Absorbed energy distribut.* **(c)** *Keyhole wall temperature*

Figure 4.42: *Excerpt of simulation results according to parameters from Table 4.14*

An excerpt of the calculation results is presented in Figure 4.42. The cross section shows an implausible shape with a necking area at ~ 4.5 mm below the surface and an additional constriction of the seam below 22 mm. These regions correlate with discontinuities in distribution of absorbed energy and keyhole wall temperature.

According to [62], the drop of the absorbed power at $y \approx 3\,\mathrm{mm}$ may be caused by unfavourable circumstances in the calculation of the beam reflections. This means, that the distribution of the reflections in unfavourable beam geometry cases result in areas without impinging beam, hence without heat generation.

Adjusting the beam divergence angle θ in order to change the impact angles, thus the trajectories of the reflected electrons, leads to different results, but always with discontinuities in the energy absorption graph, whether with single change of θ or with adjusted r_0 according to equation (4.1) (Figure 4.43). The graph from Figure 4.43d showed the most proper results, which can be attributed to the relatively high focal diameter (~ 0.9 mm) at the small beam divergence angle.

Since errors in results, like described above, did not occur when simulating 1.4313 with similar welding parameters, it is assumed, that these problems arise due to the material properties of highly conductive copper. For instance, Cu-DHP's thermal diffusivity at room temperature can be calculated to $a = 93\,\mathrm{mm^2/s}$ according to values from Table 4.14, which is more than 12 times higher than 1.4313 ones, calculated to $a = 7.6\,\mathrm{mm^2/s}$ with material properties at room temperature from Table 3.4 on page 36.

Adaption of material properties

In the next step, single material properties were changed one by one, starting from parameters from Table 4.14. A change of T_M or T_B cannot smooth the absorbed energy graph. A variation of λ, c_p, ρ or σ_L can lead to a smooth graph without errors and a reasonable shape of the seam. With either

$$\begin{aligned} \lambda &\leq 3.1\,\mathrm{W/(cm\,K)}\,, \\ c_p &\geq 0.67\,\mathrm{J/(g\,K)}\,, \\ \rho &\geq 13.4\,\mathrm{g/cm^3} \text{ or} \\ \sigma_L &\geq 7.0\,\mathrm{N/m}\,, \end{aligned}$$

the errors in the visible results disappear. Thermal diffusivity resulting from these threshold values are $a = 78.1\,\mathrm{mm^2/s}$ for the λ adaption, $61.6\,\mathrm{mm^2/s}$ for the adaption of c_p, $62.02\,\mathrm{mm^2/s}$ for adapted ρ and with adaption of σ_L the thermal diffusivity remains

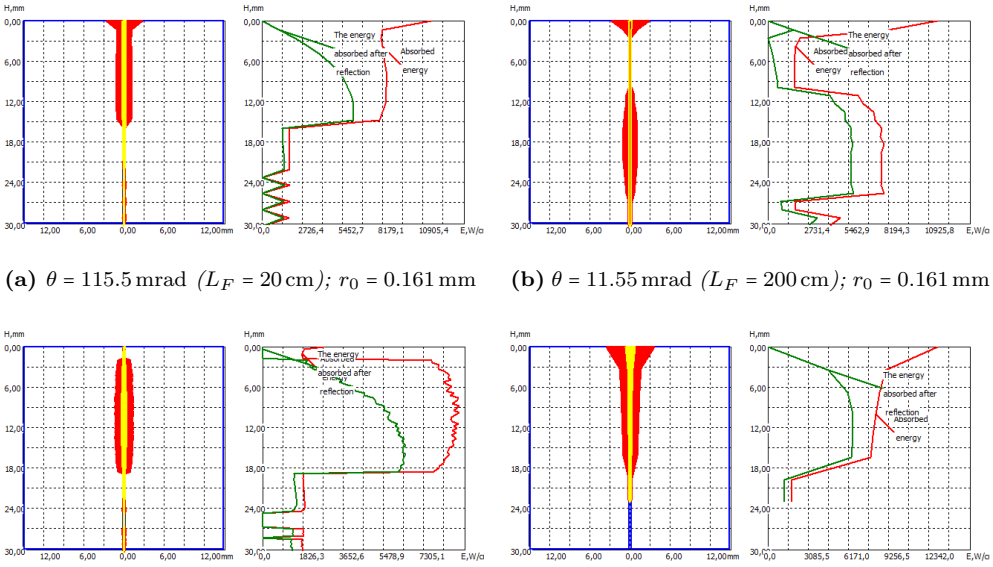

(a) $\theta = 115.5\,\text{mrad}$ *($L_F = 20\,\text{cm}$); $r_0 = 0.161\,\text{mm}$*

(b) $\theta = 11.55\,\text{mrad}$ *($L_F = 200\,\text{cm}$); $r_0 = 0.161\,\text{mm}$*

(c) $\theta = 115.5\,\text{mrad}$ *($L_F = 20\,\text{cm}$); $r_0 = 0.043\,\text{mm}$*

(d) $\theta = 11.55\,\text{mrad}$ *($L_F = 200\,\text{cm}$); $r_0 = 0.429\,\text{mm}$*

Figure 4.43: *Absorbed energy and cross section results with different beam divergence angles θ; 4.43a and 4.43b without adjustment of focal radius r_0; 4.43c and 4.43d with adjustment of focal radius r_0*

unchanged at $a = 93\,\text{mm}^2/\text{s}$. These threshold values are only valid for these very beam parameter setting. They vary with different beam parameter input, hence cannot be seen as distinct threshold values.

According to Figure 4.15 on page 55, these four material properties all have an influence in the seam geometry. Especially the thermal conductivity influences the depth H and the width W respectively the areas S of the fusion zone in a strong way, which can also be seen in the pareto charts of the standardised effects (Figure 4.16, page 56).

A closer look on error-free simulation outputs unveils discrepancies in seam shape and thermal cycle output. As, for instance, Figure 4.44 shows the cross section result calculated with $\lambda = 3\,\text{W}/(\text{cm}\,\text{K})$. Although the shape does not look irrational and the corresponding absorbed energy distribution shows no discontinuities, a study of the thermal cycles reveals discrepancies regarding the cross section output. Similar to the issues with the 3D-HTM discussed in Section 4.2.4, the thermal cycles do not match with the seam shape. The indicated black lines are connecting several points "×" fulfilling the condition $T_{max} = T_M$, meaning the material inside these lines is experiencing temperatures $> T_M$, hence is molten.

Adaption of v and U_A

Similar behaviour was detected when changing the welding speed v and acceleration voltage U_A. With values $v \geq 1.5\,\text{cm}/\text{s}$, respectively $U_A \leq 65\,\text{kV}$, again results without errors in the absorbed energy distribution and a reasonable looking cross section, but unreasonable thermal cycles were observed.

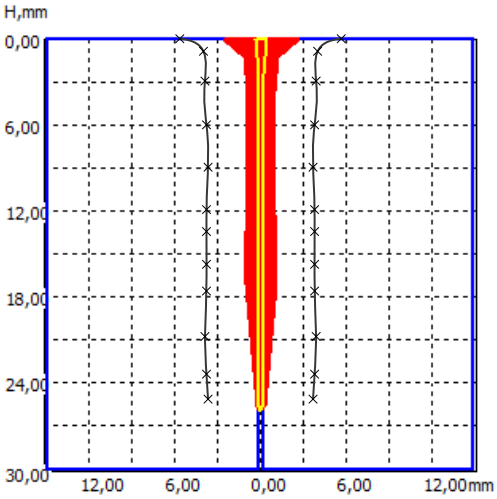

Figure 4.44: *Cross section result with indication of points fulfilling the condition $T_{max} = T_M$ in the thermal cycle output; simulation input according to parameters from Table 4.14 except $\lambda = 3\,\mathrm{W/(cm\,K)}$*

Adaption of λ, ρ and c_p according to values for liquid copper

In [10], a drop of thermal conductivity at the melting point to values $\lambda \approx 1.6\,\mathrm{W/(cm\,K)}$ was encountered [10, p. 63]. With values for $c_p \approx 0.7\,\mathrm{J/(g\,K)}$ [10, p. 58] and thermal diffusivity $a \approx 3.75 \cdot 10^{-5}\,\mathrm{m^2/s}$ [10, p. 64], the density can be calculated to $\rho \approx 6.1\,\mathrm{g/cm^3}$.

Figure 4.45 shows the results. In comparison to the first simulations, there are no visible errors in the absorbed energy distribution. Nevertheless, the thermal cycle output does not match the indicated fusion zone, as can be seen in Figure 4.45a. However, the divergence between the indicated lines fulfilling $T_{max} = T_M$ and the fusion zone is smaller compared to mere adaption of thermal conductivity to $\lambda = 3\,\mathrm{W/(cm\,K)}$ (Figure 4.44).

Compared to the macro pictures from the experiments (image section in Figure 4.45a), the seam looks broader and less conical in the simulation. The transmitting power for this very simulation is 4.25 kW, which is ~ 24 % of the beam power. A penetration depth of 38.7 mm could have been achieved, meaning the welded specimen thickness is reduced by a factor of $\frac{38.7\,\mathrm{mm}}{30.0\,\mathrm{mm}} = 0.78$, which is reasonable, as in [37, p. 48] a factor of ~ 0.8 is recommended to ensure a proper root forming.

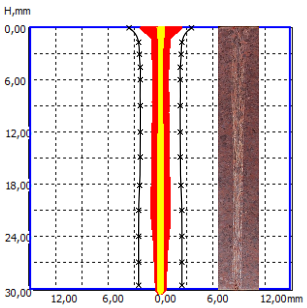

(a) *Cross section plane with indication of points fulfilling the condition $T_{max} = T_M$ in the thermal cycle output*

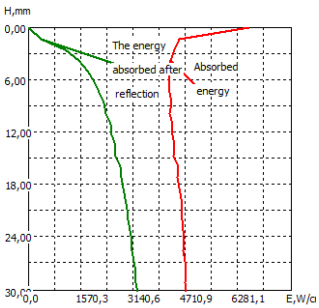

(b) *Absorbed energy distribut.*

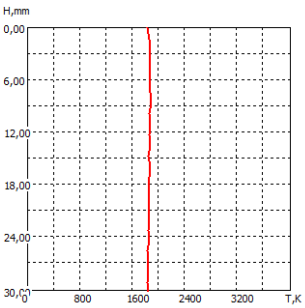

(c) *Keyhole wall temperature*

Figure 4.45: *Excerpt of simulation results with adaption of λ, ρ and c_p according to values for liquid copper*

Point figure welds

As mentioned before, the point figure welds were made in order to eliminate divergences between welds carried out with oscillating figure and simulations with a point figure model as well as uncertainties according to the focal radius r_0.

The input parameters for the simulation are listed in Table 4.15. For the material parameters λ, ρ and c_p, the values for liquid copper were used. With beam currents of 60 mA and 80 mA at 120 kV, the known focal radii and aperture values from Table 4.4 on page 49 can be used.

Figure 4.46: *Section cut of bead on plate welds of a Cu-DHP specimen of* 30 mm *thickness welded with parameters from Table 3.2*

Table 4.15: *Input parameters for Cu-DHP point figure welds*

Material parameters			Beam and geometry parameters							
			Seam	1	2	3	4	5	6	
T_M	1357	K	U_A	120	120	120	120	120	120	kV
T_B	2835	K	P	9.6	9.6	9.6	7.2	7.2	7.2	kW
c_p	0.70	$^{J}/_{(g\ K)}$	v	1.0	0.5	2.0	0.5	2.0	1.0	$^{cm}/_{s}$
ρ	6.10	$^{g}/_{cm^3}$	A	1.15	1.15	1.15	1.10	1.10	1.10	cm
λ	1.60	$^{W}/_{(cm\ K)}$	r_0	0.016	0.016	0.016	0.014	0.014	0.014	cm
σ_L	1.29	$^{N}/_{m}$	L_F	75	75	75	75	75	75	cm
σ_T	0.234	$^{mN}/_{(m\ K)}$	f_P	0	0	0	0	0	0	cm
ΔH_{LG}	4826.9	$^{kJ}/_{kg}$	h	30	30	30	30	30	30	mm

For the penetration depth result, the average deviation was +50 % compared to experimental data. The deviation is assumed to result from the adaption of material parameters (see also Table 4.7). All simulation results were free of visible errors, except for seam number 4, with a discontinuity concerning the absorbed energy distribution at $H \approx 4.5$ mm leading to an irregularity in the seam shape. Nevertheless differences between the indicated fusion zone and the thermal cycle outputs exist.

In Figure 4.47 measured and calculated thermal cycles are superimposed. Owing to artefacts in the measuring signal, very few data can be used for analysis. Only the cooling phase, beginning at ~ 4 s after the EB has passed the thermocouple, is recorded properly. Comparing seam No. 1 to seam No. 6, a temperature offset in the experimental data of ~ 100 K could be recognised. This temperature difference ΔT_{PH} can be explained by the heating that the specimen experiences between welds No. 1 and 6. For plotting the graphs Cu_6_3 and Cu_6_1 in Figure 4.47b a pre-heating effect of $\Delta T_{\mathrm{PH}} = 100$ K was substracted. The slope of the time-temperature curves is, within the range of the TC-measurement (~ 4 s ... 200 s), higher for the calculated results.

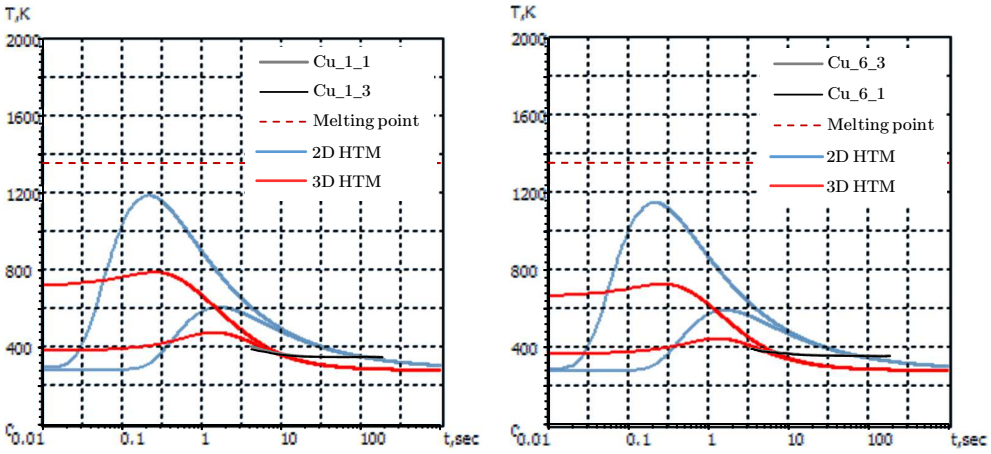

(a) *Seam No. 1*

(b) *Seam No. 6 ($\Delta T_{\mathrm{PH}} = 100\,\mathrm{K}$ considered)*

Figure 4.47: *Experimental and calculated thermal cycle output of Cu-DHP point figure welds for seams No. 1 and 6 with input data according to Table 4.15*

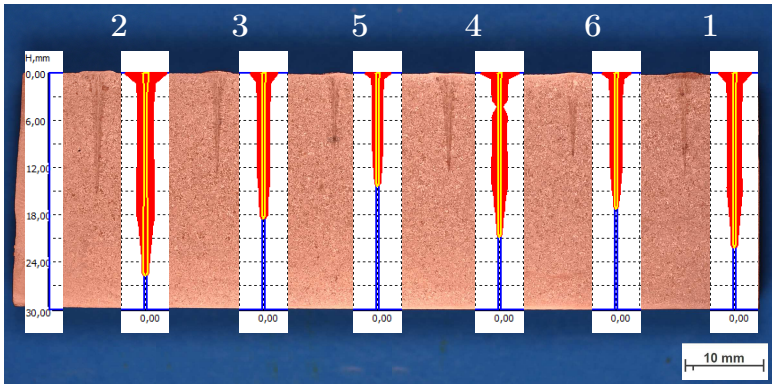

Figure 4.48: *Experimental data versus simulation output for Cu-DHP point figure welds with input data according to Table 4.15*

4.3.2 Cu80 Sn20

The bronze material Cu80 Sn20 was welded with the same welding parameters as the point figure weldings of Cu-DHP. The input parameters for LaserCAD are listed in Table 4.16. For the melting point, the liquidus temperature from the Cu-Sn phase diagram from Figure 2.4a (page 9) was taken, which is ~ 895 °C. For the boiling point temperature, the value for pure copper was taken. For a first approach, values for heat capacity, density and heat conductivity were estimated based on Figure 2.6 from page 11. Surface tension values were estimated according to Figure 2.7 (page 11). For latent heat of evaporation, the value, provided by the material database of LaserCAD, was taken.

In Figure 4.50 the cross section results are compared to experimental data. On an average and without consideration of seam No. 2, the calculated penetration depth is 21 % higher than the experimental results. The calculated seam width on the upper surface W_0 appears 29 % too narrow and the width at half of penetration depth $W_{H/2}$ appears 45 % too wide.

Figure 4.49: *Section cut of bead on plate welds of a Cu80 Sn20 specimen with a thickness of* 37 mm *welded with parameters from Table 3.3*

Table 4.16: *Input parameters for Cu80 Sn20 point figure welds*

Material parameters			Beam and geometry parameters							
			Seam	1	2	3	4	5	6	
T_M	1168	K	U_A	120	120	120	120	120	120	kV
T_B	2835	K	P	9.6	9.6	9.6	7.2	7.2	7.2	kW
c_p	0.37	$^{J}/_{(g\,K)}$	v	1.0	0.5	2.0	0.5	2.0	1.0	$^{cm}/_{s}$
ρ	8.56	$^{g}/_{cm^3}$	A	1.15	1.15	1.15	1.10	1.10	1.10	cm
λ	0.60	$^{W}/_{(cm\,K)}$	r_0	0.016	0.016	0.016	0.014	0.014	0.014	cm
σ_L	0.835	$^{N}/_{m}$	L_F	75	75	75	75	75	75	cm
σ_T	0.000	$^{mN}/_{(m\,K)}$	f_P	0	0	0	0	0	0	cm
ΔH_{LG}	4826.9	$^{kJ}/_{kg}$	h	30	30	30	30	30	30	mm

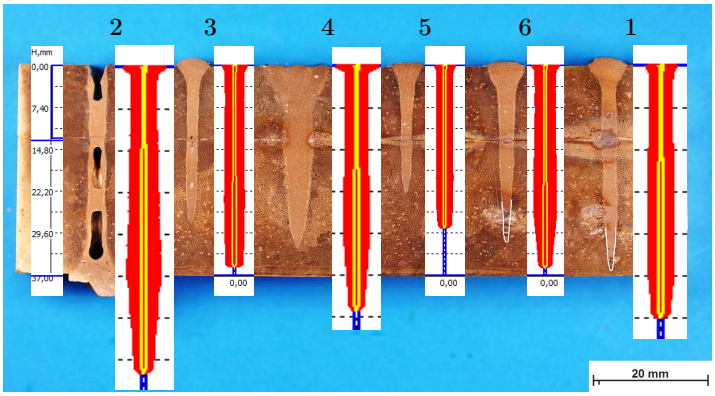

Figure 4.50: *Experimental data versus simulation output for Cu80 Sn20 point figure welds with input data according to Table 4.16; Root of seams No. 1 and 6 are outlined for better recognition despite etching defects*

Adaption of evaporation enthalpy and thermal conductivity

With a linear approach the evaporation enthalpy was adapted according to the mass fractions w_i of the main alloy elements copper and tin. With $\Delta H_{LG,\mathrm{Cu}} = 4730\,^{kJ}/_{kg}$ [21] and $\Delta H_{LG,\mathrm{Sn}} = 2492\,^{kJ}/_{kg}$ [21] latent heat of evaporation is calculated with equation (4.13) to $4282.4\,^{kJ}/_{kg}$.

$$\Delta H_{LG} \approx \sum_i \left[\Delta H_{LG,i} \times w_i\right] \tag{4.13}$$

The thermal conductivity at higher temperatures is unknown for this material. In Figure 4.51, the thermal conductivity range for copper and copper-tin alloys at different temperatures is shown. For the bronze materials ("○", "△", "◇", "□" and "×") no data for temperatures > 200 °C is available. At temperatures of ~ 1000 °C, just before melting occurs, λ is assumed to reach ~ $100\,^{W}/_{(m\,K)}$. That implies a roughly linear $\lambda(T)$ behaviour, which cannot be verified, yet excluded.

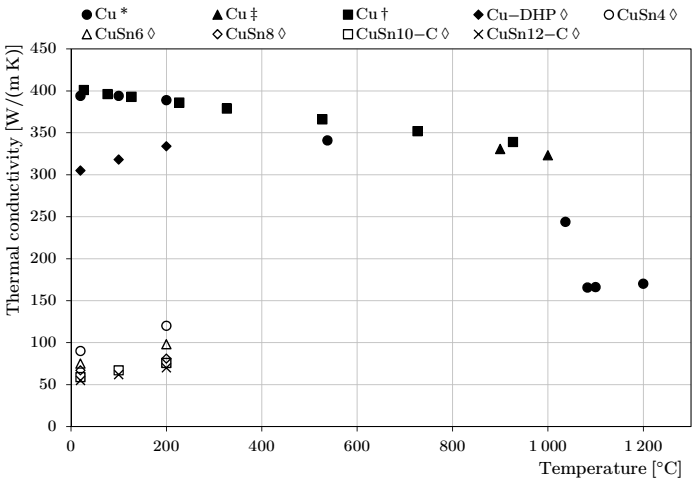

Figure 4.51: *Thermal conductivity of copper and copper-tin alloys versus temperature from different sources;*

✻ ..... [17]
† ..... [15]
‡ ..... [10]
◊ ..... [8, 12, 24–27]

With adaptions $\Delta H_{LG} = 4282.4\,\mathrm{kJ/kg}$ and $\lambda = 1\,\mathrm{W/(cm\,K)}$ simulation results leading to deviations marked with "†" in Figure 4.53 arise. The deviation of penetration depth could be drastically decreased to an average of +1.7 %. The deviation of W_0, the seam width on the upper surface, increased to an average of −34.5 %. The absolute values for the width at half of depth $W_{H/2}$ decreased in general, leading to smaller deviations except for seam No. 4.

Adaption of evaporation enthalpy, thermal conductivity and melting point

An additional change of the melting point temperature to the solidus temperature of ~ 1073 K (Figure 2.4a) lead to results depicted in Figure 4.52.

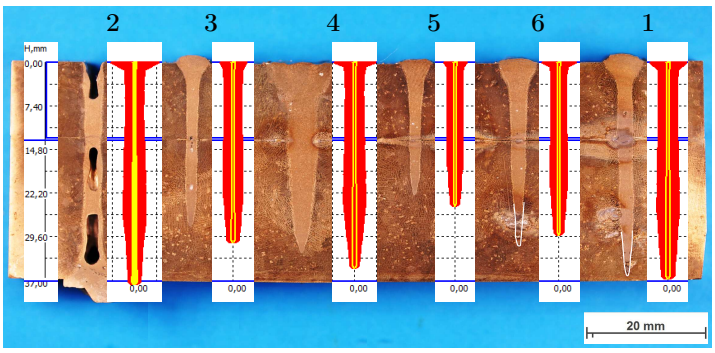

Figure 4.52: *Experimental data versus simulation output for Cu80Sn20 point figure welds with input data according to Table 4.16, except* $\lambda = 1\,\mathrm{W/(cm\,K)}$, $\Delta H_{LG} = 4282.4\,\mathrm{kJ/kg}$ *and* $T_M = 1073\,\mathrm{K}$

Figure 4.54 shows a comparison of measured and calculated thermal cycles for seams No. 1 and 6. As in case of the copper weldings, merely during the cooling phase evaluable measurement signals were gathered. The temperature offset ΔT_{PH} in the experimental data between seam No. 1 and 6 is ~ 60 K, hence ~ 40 K less compared to the copper weldings. Again, this pre-heating effect was substracted in plotting the graphs for seam No. 6 (Figure 4.54b). The moment the time-temperature-curves meet, thus the two measuring points reach the same temperature level, is reached at a later point in experimental data than in simulation outcome. This time shift is ~ 30 s for seam No. 1 and ~ 8 s for seam No. 6 and could be interpreted as an indication, that the real thermal diffusivity is smaller than the thermal diffusivity assumed for the simulation. The thermophysical values used for this very calculation were estimated for the solid phase at temperatures around the melting point. Thermal

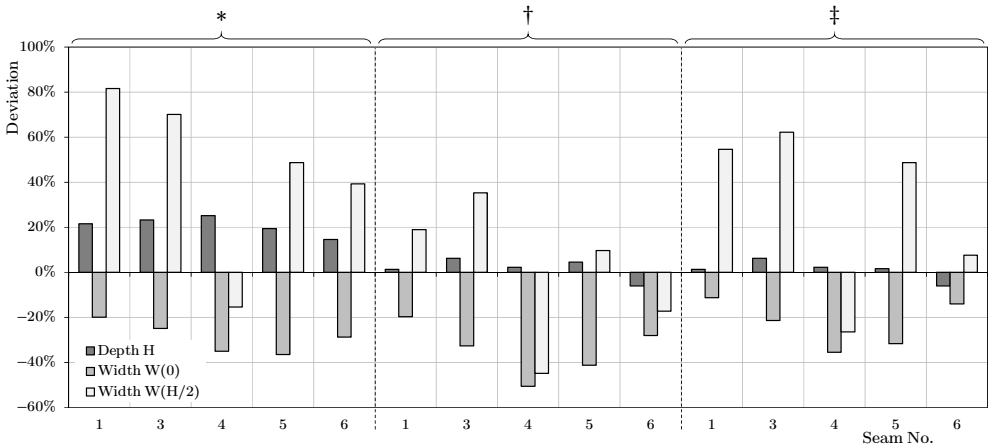

✻ . . . Parameters from Table 4.16
† . . . As ✻ except $\lambda = 1\,\mathrm{W/(cm\,K)}$ and $\Delta H_{LG} = 4282.4\,\mathrm{kJ/kg}$
‡ . . . As ✻ except $\lambda = 1\,\mathrm{W/(cm\,K)}$, $\Delta H_{LG} = 4282.4\,\mathrm{kJ/kg}$ and $T_M = 1073\,\mathrm{K}$

Figure 4.53: *Deviation of penetration depth H, width on surface W_0 and width at half of depth $W_{H/2}$ for different input parameters (✻, † and ‡); Seam No. 2 is a full penetration weld, thus is not taken into account*

conductivity as well as thermal diffusivity of pure copper experience a drop of ~ 50 % when melting (Figures 2.3b and 2.3c on page 7). Assuming that thermal conductivity of bronze experiences such a drop as well, the effective physical thermal diffusivity in the molten bath is smaller than the solid phase values. With the adjustment of c_p and λ to decrease thermal diffusivity a, the time shift in the thermal cycles decreases from ~ 30 s to ~ 20 s (Figure 4.54). Nevertheless, such an adaption increases the deviation of the penetration depth result to about 25 %.

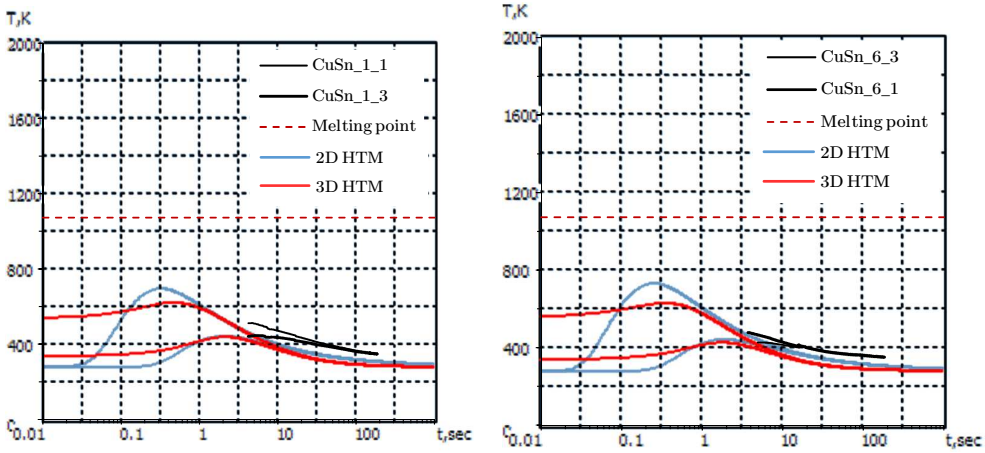

(a) *Seam No. 1*

(b) *Seam No. 6 ($\Delta T_{\mathrm{PH}} = 60\,\mathrm{K}$ considered)*

Figure 4.54: *Experimental and calculated thermal cycle output of Cu80 Sn20 point figure welds for seams No. 1 and 6 with input data according to Table 4.16, except $\lambda = 1\,\mathrm{W/(cm\,K)}$, $\Delta H_{LG} = 4282.4\,\mathrm{kJ/kg}$ and $T_M = 1073\,\mathrm{K}$*

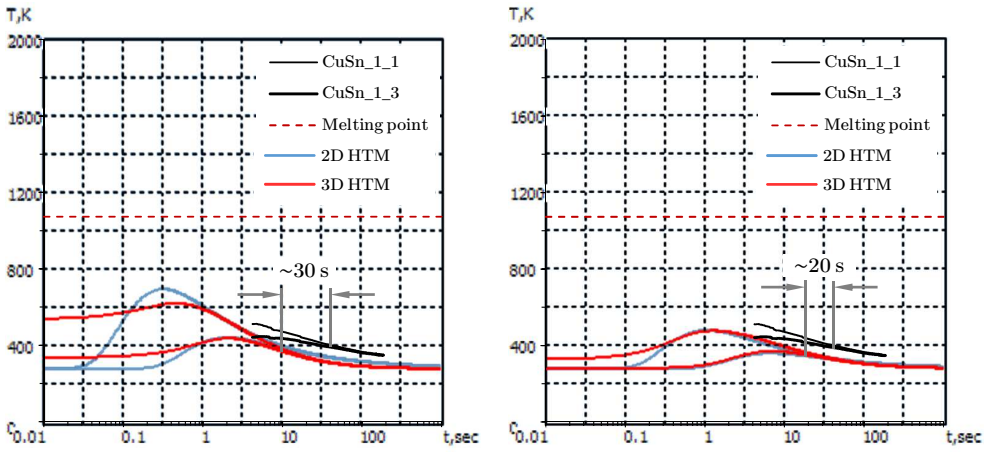

(a) $\lambda = 1\,\mathrm{W/(cm\,K)}$; $c_p = 0.37\,\mathrm{J/(g\,K)}$; *depth deviation* = +1.3 %

(b) $\lambda = 0.5\,\mathrm{W/(cm\,K)}$; $c_p = 0.6\,\mathrm{J/(g\,K)}$; *depth deviation* = +24.9 %

Figure 4.55: *Experimental and calculated thermal cycle output of Cu80 Sn20 point figure welds for seams No. 1; Input data according to Table 4.16, except* $\Delta H_{LG} = 4282.4\,\mathrm{kJ/kg}$ *and* $T_M = 1073\,\mathrm{K}$ *with different values for* λ *and* c_p

4.3.3 CuSn6

In [1], butt welds with Cu-DHP as base material and sheets of CuSn6 as filler metal were made, in order to gain a melting range instead of a melting point leading to a more viscous - hence easier to control - weld bath. The following investigations were conducted to simulate the influence of the different materials on the behaviour and the geometry of the fusion zone.

Based on the experiences presented above with simulations of Cu-DHP and the bronze material Cu80 Sn20, material input parameters for CuSn6 are listed in Table 4.17. For the melting point, the solidus temperature for CuSn6, which is ~ 900 °C [8], was chosen. For the boiling point, the value for pure copper was taken. Values for heat capacity c_p and density ρ were taken from [8] as well. On the basis of investigations in Section 4.3.2, the thermal conductivity was estimated to $1.2\,\mathrm{W/(cm\,K)}$. According to Figure 2.7 on page 11, σ_L was estimated to $1.28\,\mathrm{N/m}$ and $\sigma_T = -0.123\,\mathrm{mN/(mK)}$. LaserCAD does not consider a negative algebraic sign of surface tension's temperature coefficient σ_T, meaning $-0.123\,\mathrm{mN/(mK)}$ is interpreted as $+0.123\,\mathrm{mN/(mK)}$. Therefore σ_T was set = 0 and for σ_L, the surface tension at melting point $\sigma(T_M)$ was taken, calculated to $1.136\,\mathrm{N/m}$ according to equation (2.2) on page 10. Latent heat of evaporation was calculated to $\Delta H_{LG} = 4595.7\,\mathrm{kJ/kg}$ according to equation (4.13) (page 79).

In order to compare the simulation outcome with the results presented in Figure 4.45, the calculation was conducted with the same welding parameters (*SF-D1-Naht1*, Table 3.1, page 30).

In Figure 4.56, two cross sections are presented. The simulations were carried out using the same beam parameters and joint geometry but different material properties. While Figure 4.56a shows simulation results calculated with Cu-DHP and a metallographic section cut of seam *SF-D1-Naht1*, Figure 4.56b shows results for CuSn6 with a picture of *SF-V25*. Seam *SF-D1-Naht1* was carried out with a circular oscillation

Table 4.17: *Input parameters for simulation of SF-D1-Naht1 with material properties of CuSn6*

Beam and geometry parameters		Material parameters	
U_A	150 kV	T_M	1173 K
P	18 kW	T_B	2835 K
v	1 $^{\mathrm{cm}}/_{\mathrm{s}}$	c_p	0.377 $^{\mathrm{J}}/_{(\mathrm{g\ K})}$
A	1.15 cm	ρ	8.82 $^{\mathrm{g}}/_{\mathrm{cm}^3}$
r_0	0.016 cm	λ	1.20 $^{\mathrm{W}}/_{(\mathrm{cm\ K})}$
L_F	75 cm	σ_L	1.136 $^{\mathrm{N}}/_{\mathrm{m}}$
f_P	0 cm	σ_T	0.00 $^{\mathrm{mN}}/_{(\mathrm{m\ K})}$
h	30 mm	ΔH_{LG}	4585.7 $^{\mathrm{kJ}}/_{\mathrm{kg}}$

figure with dx = 0.5 mm and dy = 0.5 mm while for seam *SF-V25* the triangular figure with dx = 0 mm and dy = 1.5 mm were used.

Since in the experiments beam oscillation is used, the comparability with the experimental data is limited. Moreover for seam *SF-V25* CuSn6 was only used as a filler metal with C-DHP as the base material. Meaning the tin amount of the fusion zone lays somewhere between 0 and 6 % in case of an ideal mixture. Nevertheless, a juxtaposition to show the differences of the two alloys was made. Looking at the results in Figure 4.56, a broader fusion is observable when simulating CuSn6. Moreover, the tapering shape in the bottom area is noticeable in the CuSn6 calculation.

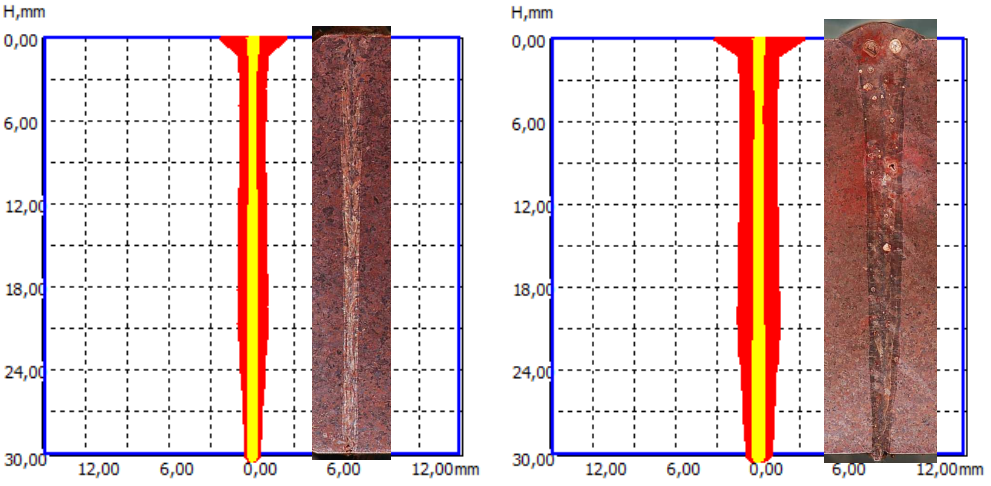

(a) *Simulation input material: Cu-DHP; Metallographic section cut: SF-D1-Naht1 [1] (full penetration bead on plate weld on Cu-DHP)*

(b) *Simulation input material: CuSn6; Metallographic section cut: SF-V25 [1] (full penetration butt weld with Cu-DHP base material and CuSn6 filler metal)*

Figure 4.56: *Comparison of cross section results for parameter input according to seam SF-D1-Naht1 from Table 3.1 for two different material input values with metallographic pictures*

Cu-DHP . . Material properties according to Table 4.14, except $\lambda = 1.6\,^{\mathrm{W}}/_{(\mathrm{cm\,K})}$, $c_p = 0.7\,^{\mathrm{J}}/_{(\mathrm{g\,K})}$ *and* $\rho = 6.1\,^{\mathrm{g}}/_{\mathrm{cm}^3}$ *(Figure 4.45)*
CuSn6 . . . . Material properties according to Table 4.17

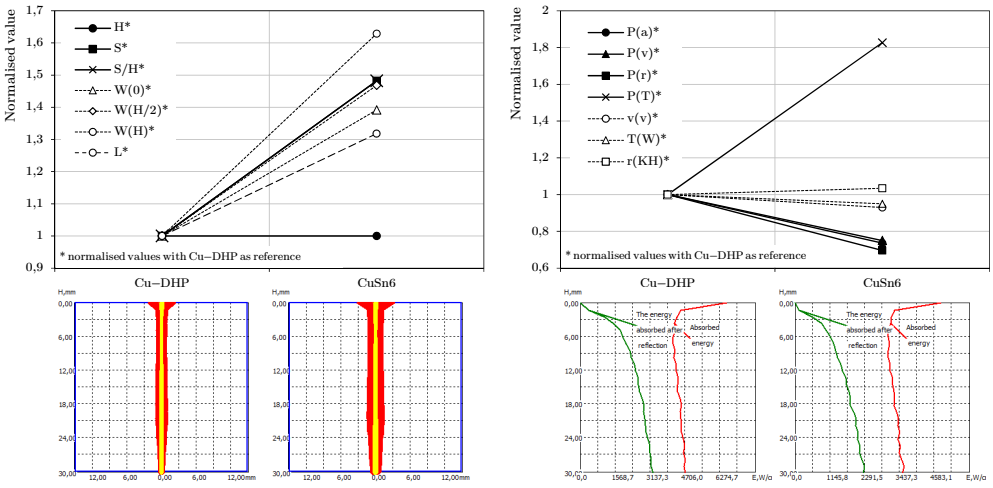

(a) *Seam geometry-related parameters* **(b)** *Energy- and keyhole-related parameters*

Figure 4.57: *Comparison of simulation outcome for parameter input according to seam SF-D1-Naht1 from Table 3.1 for two different material input values*

Cu-DHP . . Material properties according to Table 4.14, except $\lambda = 1.6\,\mathrm{W/(cm\,K)}$, $c_p = 0.7\,\mathrm{J/(g\,K)}$ *and* $\rho = 6.1\,\mathrm{g/cm^3}$ *(Figure 4.45)*
CuSn6 . . . . Material properties according to Table 4.17

Table 4.18: *Numeral simulation results for simulation with Cu-DHP and CuSn6; Beam parameters* $U_A = 150\,\mathrm{kV}$, $P = 18\,\mathrm{kW}$, $v = 10\,\mathrm{mm/s}$, $A = 1.15\,\mathrm{cm}$, $r_0 = 0.016\,\mathrm{cm}$, $L_F = 75\,\mathrm{cm}$, $f_P = 0\,\mathrm{cm}$, $h = 30\,\mathrm{mm}$ *(SF-D1-Naht1 from Table 3.1)*

Material	Cu-DHP	CuSn6	Unit
Geometry-related results			
H	30.08	30.08	mm
S	37.88	56.14	$\mathrm{mm^2}$
S/H	1.26	1.87	mm
W_0	4.66	6.45	mm
$W_{H/2}$	1.85	2.71	mm
W_H	1.23	2.00	mm
L	5.54	7.30	mm
Energy- and keyhole-related results			
P_a	13466	9910	W
P_v	96	72	W
P_r	79	55	W
v_v	364.8	339.2	m/s
T_W	1838	1746	K
r_{KH}	0.348	0.360	mm

Figure 4.57 compares the simulation results based on results for Cu-DHP. The abscissa represents the two different materials and the ordinate gives the normalised values for each output parameter. In Figure 4.57a, geometry-related parameters and

in Figure 4.57b, energy-related and keyhole-related parameters are represented. Results for Cu-DHP serve as a reference, wherefore Cu-DHP's normalised values are equal to 1.

Looking at the geometry-related parameters, it can be seen that the geometry increases in general. The only exception is the penetration depth, which is constant, since a full penetration level was achieved. In case of partial penetration ($h > H$), the penetration depth H would increase from 38.7 mm to 51.7 mm which would mean an increase of 33.6 %. In return to unvarying H, it is evident that the absorbed power P_a decreases and the amount of transmitted power P_T increases drastically (Figure 4.57b). The reflection losses P_r and evaporation losses P_v decrease as well. Looking at the graphs of absorbed energy distributions, the absorbed energy per penetration depth for Cu-DHP is ~ 6300 $^{\mathrm{W}}/_{\mathrm{cm}}$ at the upmost layer. Compared to this, the level of CuSn6 is at ~ 4600 $^{\mathrm{W}}/_{\mathrm{cm}}$, hence about 27 % smaller, which correlates to the normalised values $P_r^* = 0.70$ and $P_v^* = 0.75$. Vapour flow speed v_v and wall temperature T_W decrease slightly about 7 % and 5 % and keyhole radius on surface r_{KH} increases about 3.5 %.

A similar juxtaposition was made with simulation results for welding parameters of seam No. 1 from Cu-DHP and Cu80 Sn20 point figure welds (Table 3.2 and Table 3.3 on page 31 respectively 33). The calculations with material parameters for Cu-DHP, CuSn6, Cu80 Sn20 and 1.4313 were conducted. The parameters and the numeral simulation outputs are listed in Table 4.19. Again, the results have been normalised with Cu-DHP as a reference. Together with the cross section results and absorbed energy graphs, the normalised values are plotted in Figure 4.58.

Looking at the copper materials Cu-DHP, CuSn6 and Cu80 Sn20, the geometry-related parameters increase with increasing amount of tin. The only exception is the width on the surface W_0, which decreases from CuSn6 to Cu80 Sn20. Especially the fusion zone area S increases drastically. The calculated area of Cu80 Sn20 is 3.2 times higher than the value of Cu-DHP. When simulating with CuSn6, the penetration depth H is 33 % higher than Cu-DHP ones and with Cu80 Sn20 even 66 % higher than Cu-DHP ones. The average width $^{S}/_{H}$ increases to normalised values of 1.6 for CuSn6 and 1.9 for Cu80 Sn20, which is quite the same level as the width at half of depth $W_{H/2}$ attains.

The penetration depth resulting for stainless steel 1.4313 is 55 % higher than Cu-DHP ones. The average width and the width at half of depth of 1.4313 are quite at the same level as the widths calculated with Cu-DHP. In general, the fusion zone of 1.4313 appears narrower than the fusion zone of bronze. While the normalised width on the surface W_0 reaches values of about 1.6 for CuSn6 and 1.5 for Cu80 Sn20, the width in the root W_H increases to 1.8 and 2.2 times the values for Cu-DHP. The width on the surface, calculated for steel, falls below Cu-DHP ones, the width in the root is ~ 1.6 times higher. The length of the molten bath L increases by 36 % and 44 % for the bronze materials and decreases by 18 % for steel.

Aspect ratios of ~ 1:18 for Cu-DHP, ~ 1:15 for CuSn6, ~ 1:16 for Cu80 Sn20 and ~ 1:27 can be calculated using average seam width $^{S}/_{H}$ and penetration depth H.

The vapour flow out speed v_v as well as the keyhole wall temperature T_W decrease slightly with increasing tin amount. The vapour flow speed calculated for steel is 20 % higher and the wall temperature is, measured in K, 10 % higher than Cu-DHP ones. The keyhole radius on the surface r_{KH} increases by 4 % and 7 % for the bronze materials and 5 % for 1.4313. The absorbed power P_a remains nearly constant for all materials.

The losses P_v and P_r decrease compared to Cu-DHP, except for evaporation losses when simulating steel. However, their summarised fraction on the impinging power P is with $\sim 1\,\% \ldots 2\,\%$ very small. LaserCAD does not consider losses owing to thermal radiation P_R. A rough estimation using the adapted STEFAN-BOLTZMANN law for calculating the effective radiated power for grey bodies [39] (equation (4.14)) proofs the legitimacy to neglect these influences.

$$P_R = \epsilon(T) \cdot k_B \cdot A \cdot \left(T^4 - T_a^4\right) \tag{4.14}$$

Here ϵ is the emissivity of the grey body, k_B is the so-called STEFAN-BOLTZMANN constant[5], A is the emitting surface area, T the temperature of the grey body and T_a the ambience temperature. Assuming an elliptic weld bath with the width W_0 and the length L, the area can be calculated with equation (4.15):

$$A = \frac{\pi}{4} \cdot W_0 \cdot L \tag{4.15}$$

For the temperature T, the keyhole wall temperature T_W was taken, which is a conservative assumption since the molten bath temperature around the cavity is surely on a lower temperature level. An ambience temperature of 293 K was assumed. The emissivity of liquid copper is 0.15, for cuprous oxide in a temperature range of $800\,^\circ\mathrm{C} \ldots 1100\,^\circ\mathrm{C}$, emissivity values from $\epsilon = 0.66 \ldots 0.54$ can be assumed. The highest emissivity value for copper is $\epsilon = 0.88$ for oxidised copper at $800\,^\circ\mathrm{C}$. [77] Nevertheless, an emissivity value of 1, hence a black body was assumed. The results are listed in Table 4.20 with power losses owing to thermal radiation $\leq 0.21\,\%$.

[5] $k_B = 5.670 \times 10^{-8}\,\mathrm{W/(m^2\,K^4)}$ [39]

Table 4.19: *Material input parameters and numeral simulation results for simulation with different materials Cu-DHP, CuSn6, Cu80 Sn20 and 1.4313; Beam parameters* U_A = 120 kV, P = 9.6 kW, v = 10 mm/s, A = 1.15 cm, r_0 = 0.016 cm, L_F = 75 cm, f_P = 0 cm, h = 50 mm *(seam No. 1 of Cu-DHP and Cu80 Sn20 point figure welds)*

Material	Cu-DHP	CuSn6	Cu80 Sn20	1.4313	Unit
Material input parameters					
T_M	1357	1173	1073	1725	K
T_B	2835	2835	2835	3133	K
c_p	0.70	0.38	0.37	1.00	J/(g K)
ρ	6.10	8.82	8.56	7.70	g/cm^3
λ	1.60	1.20	1.00	0.36	W/(cm K)
σ_L	1.290	1.136	0.835	1.820	N/m
σ_T	0.234	0.000	0.000	0.034	mN/(m K)
ΔH_{LG}	4826.9	4595.7	4282.4	6092.4	kJ/kg
Geometry-related results					
H	21.68	28.88	36.08	33.68	mm
S	25.45	54.94	80.12	41.44	mm^2
S/H	1.17	1.90	2.22	1.23	mm
W_0	4.02	6.34	6.00	2.32	mm
$W_{H/2}$	1.72	2.87	3.45	1.81	mm
W_H	1.08	1.97	2.39	1.70	mm
L	5.19	7.05	7.48	4.28	mm
Energy- and keyhole-related results					
P_a	9337	9400	9428	9308	W
P_v	90	68	49	143	W
P_r	85	59	46	55	W
v_v	364.8	339.2	324.4	438.8	m/s
T_W	1882	1779	1627	2069	K
r_{KH}	0.323	0.336	0.345	0.339	mm

Table 4.20: *Estimation of thermal radiation losses according to equation* (4.14) *for different materials Cu-DHP, CuSn6, Cu80 Sn20, 1.4313 based on simulation results from Table 4.19*

	Cu-DHP	CuSn6	Cu80 Sn20	1.4313	Unit
P_R	11.6	19.9	14.0	8.1	W
P_R/P	0.12	0.21	0.15	0.08	%

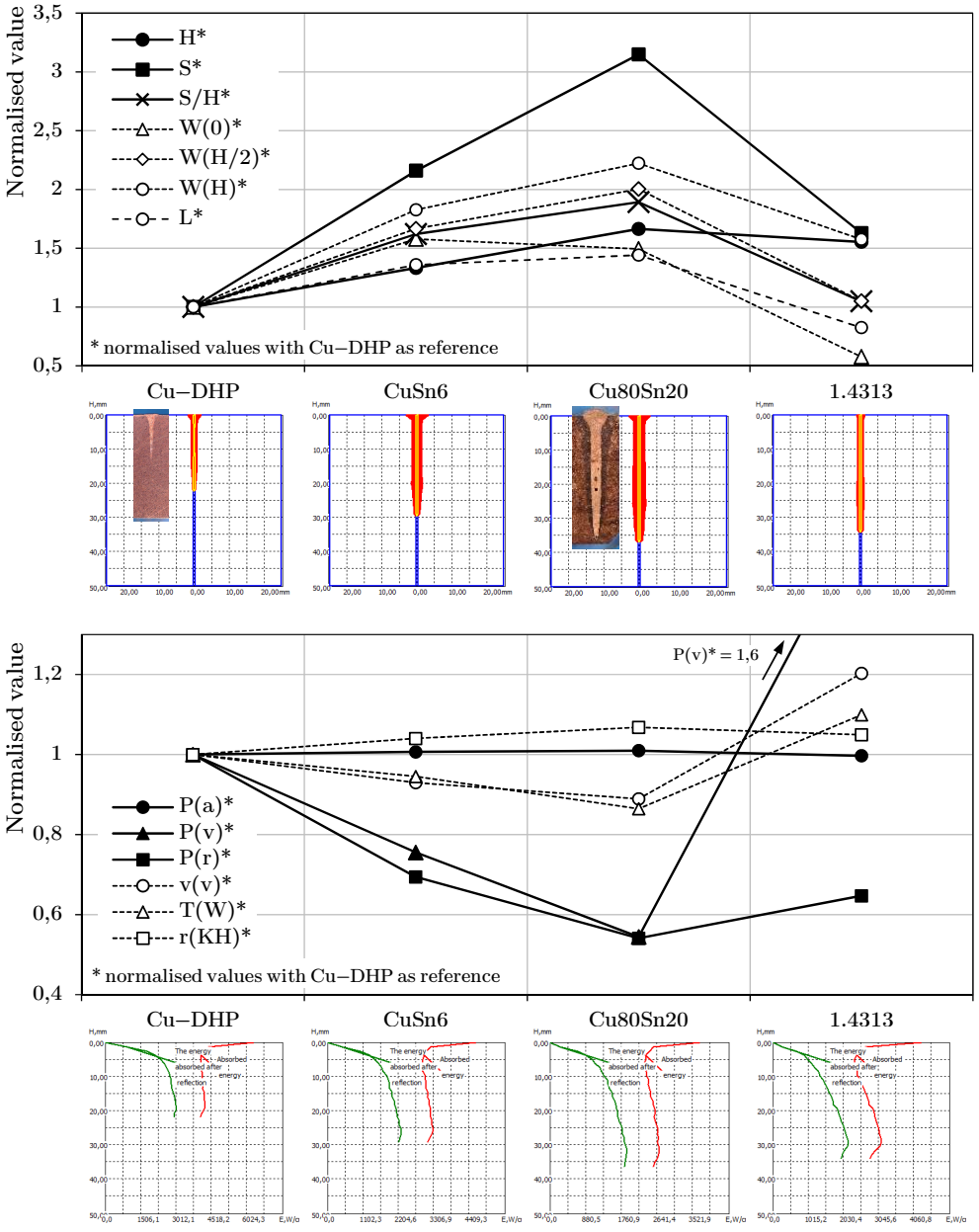

Figure 4.58: *Normalised seam geometry-related results* H^*, S^*, S/H^*, W_0^*, $W_{H/2}^*$, W_H^* *and* L^* *as well as normalised energy- and keyhole-related results* P_a^*, P_v^*, P_r^*, v_v^*, T_W^* *and* r_{KH}^* *versus different materials Cu-DHP, CuSn6, Cu80Sn20 and 1.4313; Beam parameters* $U_A = 120\,\mathrm{kV}$, $P = 9.6\,\mathrm{kW}$, $v = 10\,\mathrm{mm/s}$, $A = 1.15\,\mathrm{cm}$, $r_0 = 0.016\,\mathrm{cm}$, $L_F = 75\,\mathrm{cm}$, $f_P = 0\,\mathrm{cm}$, $h = 50\,\mathrm{mm}$ *(seam No. 1 of Cu-DHP and Cu80Sn20 point figure welds)*

Chapter 5

Discussion

The purpose of this thesis was to deal with the task of numerical simulation of electron beam welding of copper materials with LaserCAD. It was accomplished in cooperation with experts of the Institute of Laser and Welding Technology at St. Petersburg State Polytechnic University, which provided the academic software.

In order to comprehend the operating principles of LaserCAD, a systematic analysis of the numerical software was conducted, before simulations for certain copper materials were made.

Furthermore, experiments for the evaluation of simulations were conducted with the EBW machine at IWS, TU Graz. Artefacts in thermocouple measurements due to scattered electron radiation during the welding process could not be avoided. Cross sections of the specimens were sanded, polished and etched to analyse the geometry of the fusion zone area.

Systematic analysis

Generally speaking, the systematic analysis showed a reasonable behaviour of the EB-model. With decreasing U_A, I_B or increasing v, the penetration depth and the fusion zone area decreases.

LaserCAD's input parameter of the focal radius corresponds to an area, where $(1 - 1/e) \simeq 63\,\%$ of the total beam power impinges. This needs to be taken into account when the beam parameter value characterises a different amount of the Gaussian distribution, like $(1 - 1/e^2) \simeq 86.5\,\%$ in the present case. The influence of r_0 was investigated to be rather small on deviations in depth, but high on deviations in seam width, length of bath and fusion zone area, especially for bronze material.

An influence matrix of material parameter input to give a brief overview of influences in depth and area was generated. In order to examine the main effects, a screening design plan was chosen. Thermal conductivity λ has the highest effect on the result of penetration depth H, followed by latent heat of evaporation ΔH_{LG}. The highest effect on the average seam width S/H has λ as well, followed by melting point T_M and ΔH_{LG}. For further investigations on λ, ΔH_{LG}, σ_L and c_p, a CCD plan was set up. No strong interactions between these input parameters were found.

Gaps between joint faces are not considered and the chosen joint type as well as the specimen width have no influence on the results of the numerical EB-model. The sample thickness was found to correlate linearly with the transmitting power P_T, which is plausible, looking at absorbed energy graphs.

The seams calculated with the help of the 3D-HTM are broader compared to the calculation with the 2D-HTM, although, resulting from 3D-HTM's additional heat flux in z-direction, the other way round would be reasonable. Furthermore, a discrepancy in 3D-HTM's thermal cycle output and the corresponding seam shape calculation was found. According to LaserCAD's thermal cycle output, the fusion zone area calculated with the 3D-HTM is supposed to appear ~ 40 % smaller than the one calculated with the 2D-model.

Simulations with considering MARANGONI convection do not differ from simulations conducted without.

An approach of welds carried out with oscillating figures was not expedient with the mere adaption of focal radius r_0. Beam power P as well as acceleration voltage U_A need to be adapted additionally. No general adjustment setting was found to achieve simulations with proper agreement to experiments for all investigated welding parameters.

The simulations of weldings carried out without beam oscillation could achieve results with depth deviations < 3 % for seams with $P > 10\,\mathrm{kW}$ with adaption of P and U_A according to the weld crown fraction compared to the fusion zone area as well as adaption of c_p and λ to values at $T \approx T_M$ and $r_0 = 0.035\,\mathrm{cm}$. The focal positions $f_P \neq 0$ should be calculated with $f_P = 0$, in order to achieve a better accordance of penetration depth results and avoid errors in simulation results, which occurred at focal positions $f_P > 0$.

Simulation of copper materials

The simulation of the unalloyed copper material Cu-DHP led to errors in absorbed energy graph and irrational seam shapes. Threshold values for λ, c_p, ρ and σ_L to avoid these errors were investigated. Since their magnitude varies with varying beam parameters, no distinct values to avoid errors were found. Error-free simulation results with mere adaption of a single parameter showed discrepancies between seam shape and thermal cycles. Likewise, the adaption of the acceleration voltage U_A or the welding speed v led to error-free results with discrepancies between seam shape and thermal cycles.

The fact, that simulation errors do not only occur at Cu-DHP simulations, but also when calculating over-focused stainless steel welds, leads to the assumption, that no particular threshold values for certain input properties can be given.

A change of the material properties to values for liquid copper led to error-free results, yet with unreasonable thermal cycles. The simulation results of the point figure welds on Cu-DHP showed a rather high penetration depth deviation of +50 % on an average. A comparison of thermal cycles with the thermocouple measurement is unrewarding owing to the lack of useable measurement data.

For the bronze material Cu80 Sn20, simulation results calculated with thermophysical values at 20 °C showed rather high deviations. On an average, the penetration depth H is calculated 21 % too deep, the width on surface is 29 % too narrow and the width at half of depth is 45 % too wide. Appropriate results with little deviation of penetration depth of ±6 % have been achieved with an approximated value for λ at temperatures just before melting, an estimation of the alloys latent heat of evaporation ΔH_{LG} proportionate to the main element fractions as well as the alloy's solidus temperature for melting point input T_M. Deviations in seam width are with ~ ±50 % still rather high.

According to the thermal cycle analysis, a time shift between the experimental data and the simulation outcome could be recognised. The point, where the closest

and the furthest TC reach a similar temperature level appears earlier in the calculated thermal cycles than in measured ones. It was assumed, that the thermal diffusivity of the calculation is too high compared to experimental data. A decrease in the simulation's thermal diffusivity by the adaption of λ and c_p decreases this time shift, yet the penetration depth increases leading to higher deviations. LaserCAD only allows one input value per material parameter, which is used for keyhole calculation (vapour) and heat field calculation of liquid and solid, hence a classic conflict of objectives takes place.

A comparison of CuSn6 with Cu-DHP exemplary depicted for two welds from [1] showed similarities between the experiment and the simulation despite a limited potential of comparability. Simulation of CuSn6 yields an increase in the seam width and an increase of the transmitted power in contrast to Cu-DHP.

At last, a juxtaposition of simulations with different materials was realised. The unalloyed copper grade Cu-DHP, the bronze materials CuSn6 and Cu80 Sn20 as well as the stainless steel 1.4313 were compared. For copper materials, the penetration depth and the fusion zone increase with increasing tin amount. The fusion zones calculated for Cu-DHP and CuSn6 look nail-shaped. In contrast, Cu80 Sn20 and 1.4313 led to a more I-shaped seam. The penetration depth of steel lays between both bronze materials. Furthermore, the smallest aspect ratio of ~ 1:27 was achieved for steel. Compared to the impinging beam power, the evaporation and reflection losses are very small for all materials. A rough estimation showed, that radiation losses are negligibly as well.

Parts of this work were already published in form of a poster presentation at the *"8th International Conference of Beam Technologies & Laser Application"* (21^{st}–24^{th} September 2015, St. Petersburg, Russia). [78]

Simplifications and restrictions of the software

- A static beam with GAUSSIAN energy distribution is assumed as the power source. Oscillating figures cannot be simulated.
- A physically adequate model calculates the power absorption and heat generation in the keyhole and considers multiple reflections with reflection coefficients depending on the impinging angle.
- The software calculates a steady state process, no dynamic model was implemented.
- A gap between the joint faces is not taken into account and the width of the specimen has no influence on the results.
- The fusion zone calculated with the help of the 3D-heat transfer model appears taller than expected and showes discrepancies according to the thermal cycle output.
- The impinging beam on the upmost layer is the input value for the calculation procedure. The beam caustic below this layer has no influence on the calculation, which limits the possibility of investigations on focal position influences.
- Weld crown forming and root forming are not calculated (flat boundary condition).

- The ambience temperature and the working pressure are predetermined by LaserCAD and cannot be adjusted.
- The activation of the MARANGONI effect consideration has no effect on the outcome of the performed simulation.
- Thermophysical values are simply approximated by an temperature-independent value. Only for surface tension, a linear temperature dependency is considered.
- The temperature gradient of surface tension $\sigma_L = \frac{\mathrm{d}\gamma}{\mathrm{d}T}$ is always considered as a positive value.[1]
- The material's melting behaviour is approximated with a melting point, no melting range resulting in a viscous two phase region is considered. Furthermore, latent heat of melting is neglected.
- The boiling point T_B has no influence on any simulation result at all.
- Losses owing to thermal radiation are not taken into account.
- Simulations carried out with thermophysical values of high conductive materials tend to lead to numerical instabilities.
- Simulations carried out for over-focused welds ($f_P > 0$) tend to lead to numerical instabilities.

[1] $\sigma_L > 0$ is typical for weld baths with amounts of surface-active elements like S, O, As, but σ_L can also have negative values which is typical for pure metals [3]

Chapter 6

Conclusion

Based on acquired results, this chapter tries to draw a conclusion by answering preceded questions introduced in Section 1.2.

Secondary question 1
How accurate is the calculated seam geometry in relation to the experimental data?

Answer
Besides the penetration depth H as the most important geometrical parameter, the seam width W and/or fusion zone area S were analysed as well.

The simulation of welds carried out with oscillation figures is restricted. An approach with adjustment of the beam input parameters for certain welds can provide usable results, yet for merely limited parameter windows. Moreover, several experiments in advance are necessary to get input parameters for a trustworthy prediction of the seam geometry.

In LaserCAD's intended field of application, which is the simulation of point figure welds, valuable data can be achieved. With confinements in simulating highly conductive materials e.g. pure copper, reasonable results for steel and bronze materials could be gained. But again it can be said that experiments beforehand are necessary to find a proper input parameter set-up.

Although root and weld crown forming is not simulated, reasonable I-shaped seams for steel were achieved, yet with too broad root tips. Cu-DHP's V-shaped weld seams as well as the nail-shaped bronze seams could not be observed explicitly.

Generally speaking, results with both, depth- and width- or area-accordance, are rare occasions. While depth deviations in narrow limits can be attained, the calculated fusion zones tend to appear too wide compared to the experimental data.

Due to discrepancies in the 3D-HTM's simulation results, most of the calculations were carried out using the 2D-HTM. Moreover, it was shown, that a proper working 3D-heat transfer model has the potential to combine good depth- and width-accordances as well as better accordances in seam shapes.

Secondary question 2
Can LaserCAD be used to estimate occurring welding defects?

Answer
The provided version of LaserCAD only allows the calculation of the steady state condition. Dynamic welding defect formations like humping, pore formation, root run outs, spiking etc. cannot be simulated. Nevertheless, a few conclusions on occurring welding defects may be drawn based on steady state results:

- A distinct bottle neck in the keyhole shape can be interpreted as an indication, that the process is prone to keyhole collapsing.
- Seams with a sharp, narrow root are more likely to form root cavities.
- The width of the fusion zone can be used as a hint for possible porosity formations. With an increasing size of the weld pool, it becomes easier for pores to rise and escape from the fusion zone.
- Errors in the absorbed energy graph for certain focus positions or divergence angles can be a hint to unstable conditions in keyhole-beam-interaction.
- Excessive or too low transmitting power in full penetration welds, can lead to root defects.

Secondary question 3
How sensitive is LaserCAD in welding parameter influences?

Answer
Information about the beam caustics of the EBW machine is indispensable for a proper simulation outcome. Since LaserCAD's model calculates the energy absorption inside the keyhole based on absorption and reflection processes of the impinging beam, it is of vital importance to provide beam parameters which are close to reality.

The input parameter r_0 refers to the surface area corresponding to $(1 - 1/e) \simeq 63\,\%$ of the total beam power, assuming a GAUSSIAN beam. A conversion of the widely used beam measurement in agreement with *"zweites zentriertes Moment der Leistungsdichteverteilung"*[1] according to DIN 32511 [79] is necessary. Furthermore, it can be recommended to simulate weldings with a normal focus position in order to avoid erroneous results.

[1] r_0 is indicating an area corresponding to $(1 - 1/e^2) \simeq 86.5\,\%$ of the total power of a GAUSSIAN beam

Secondary question 4
How sensitive is LaserCAD according to different copper alloys?

Answer
The knowledge about the thermophysical values of the welded materials were found to be one of the most important preconditions for useful simulation results.

Thermal conductivity λ was found to be the material parameter with the most significant influence on the simulation outcome. The simulation of highly thermal conductive materials are prone to numerical instabilities leading to simulation errors.

Moreover, the calculation of the gas, the liquid and the solid phase with the usage of a single value for each thermophysical characteristic is seen as a limiting factor in gaining suitable simulation results. The usage of thermophysical values for solid state around the melting point turned out to lead to proper results.

Impurities or alloy elements in copper materials have a significant influence on their thermophysical properties. Subsequently, with changing material properties, the welding behaviour changes as well.

Results according to simulations of unalloyed, thus highly conductive copper grades need to be interpreted with caution. Nevertheless, significant differences compared to calculations of copper-tin alloys could be recognised. With increasing tin amount, the fusion zone increases in depth and width. Furthermore, alterations in the shape of the seam can be noticed for different materials.

Leading question
Is LaserCAD a useful tool for the simulation of electron beam welding of thick-walled copper materials?

Answer
LaserCAD's intuitive user interface and the efficient calculation algorithm allows fast simulations, which makes LaserCAD a suitable tool for many kinds of parameter studies.

With restrictions on highly conductive materials and weldings carried out with oscillating beam, many useful results have been gained using LaserCAD. Despite many simplifications of the model, valuable electron beam welding simulations, especially for copper-tin alloys, have been realised, where penetration depth accordance with deviations less than 3 % can be achieved. Yet, for each material, experiments beforehand were necessary to find a proper set-up of input parameters.

Although its limitations in prediction of particular occurring welding defects, the model reproduces the physical behaviour of the electron beam welding processes with deep penetration in a reasonably way.

On balance, LaserCAD is, with certain restrictions on highly conductive materials, a valuable software in simulating electron beam welds of various copper materials and has the potential to become an advantageous tool to diminish required experimental steps to produce weld seams free of any defects.

Chapter 7

Outlook

The realisation of the following aspects would lead to an improvement of LaserCAD, broaden its field of application and unlock its entirely potential.

Improvement of LaserCAD's calculation result

- Facilitate the input of the physical properties' temperature dependency or allow at least three different values for each phase: vapour, liquid and solid.
- The fix of 3D-heat transfer model's fusion zone calculation could enhance the accordance of the simulation with the experimental data.
- The correction of the graphical output of the fusion zone and the temperature distribution in general (HAZ) is essential for useful simulation outcomes.
- The implementation of different energy distribution profiles besides the GAUSSIAN distribution could enable an approach of oscillating beam figures.
- The implementation of the dynamic models described in [59–61] would allow the investigation of defect formations like pore formation or humping.
- The implementation of MARANGONI effect similar to the laser beam model could enhance the simulation output.

Improvement of experimental data for validation

- The accomplishment of electron beam welds with thermal cycle measurements which are free of defects would allow a precise validation of LaserCAD's thermal cycle output.
- The beam properties measurement to gather the beam emittance depending on the acceleration voltage and the beam current $\varepsilon(U_A, I_B)$ would enhance the accurateness of beam input parameters.

Improvement of the informative content of LaserCAD's outcome

- Direct output of the transmitting power P_T, the energy flow through the open keyhole in full penetration welding
- Output of the narrowest keyhole radius and its position

- Possibility to define points by entering coordinates and gather numeric output data of thermal cycles in a tabular form
- Enhancement of the resolution of the graphic output data

Improvement of the user experience

- Implementation of an EBW equipment database with possibility to save information about beam caustics $\varepsilon(U_A, I_B)$, so that focus diameter r_0 can be calculated automatically, depending on acceleration voltage U_A, beam current I_B and divergence angle θ.
- Possibility to save simulation session data

References

[1] P. Loidolt and N. Enzinger. *Elektronenstrahlschweißen dickwandiger Kupferbauteilen*. Tech. rep. Graz: Institute of Materials Science and Welding, Graz University of Technology, 2014.

[2] G. Turichin, E. Valdaitseva, and P. Malkin. *Software: LaserCAD Version 4.0*. St. Petersburg, 2015.

[3] G. Schulze. *Die Metallurgie des Schweißens*. 4th ed. Berlin: Springer-Verlag Berlin Heidelberg, 2010. ISBN: 9783642031823.

[4] V. Lopota, G. Turichin, E. Valdaitseva, P. E. Malkin, and A. Goumeniuk. "CAE System for Laser and Electron Beam Welding". In: *Laser Technologies in Welding and Materials Processing*. Ed. by B. E. Paton and V. S. Kovalenko. Kiev: E. O. Paton Welding Institute, 2005, pp. 96–99. ISBN: 966-8872-01-0.

[5] H.-J. Bargel and G. Schulze. *Werkstoffkunde*. 10th ed. Berlin: Springer-Verlag Berlin Heidelberg, 2008. ISBN: 978-3-540-79296-3.

[6] C. Sommitsch, H. Cerjak, N. Enzinger, and I. Holzer. *LV Skriptum Werkstoffkunde (LV-Nr.: 303.003 & 303.010)*. Graz: Institute of Materials Science and Welding, Graz University of Technology, 2015.

[7] Deutsches Kupferinstitut. *Niedriglegierte Kupferwerkstoffe*. 2012. URL: https://www.kupferinstitut.de/fileadmin/user_upload/kupferinstitut.de/de/Documents/Shop/Verlag/Downloads/Werkstoffe/i008.pdf (visited on 02/18/2015).

[8] Deutsches Kupferinstitut. *Werkstoff Datenblatt CuSn6*. 2005. URL: https://www.kupferinstitut.de/fileadmin/user_upload/kupferinstitut.de/de/Documents/Shop/Verlag/Downloads/Werkstoffe/Datenblaetter/Bronze/CuSn6.pdf (visited on 03/23/2015).

[9] Dr. Wilhelm Mertens GmbH. *Datenblatt Edelstahl 1.4313*. 2015. URL: http://www.mertens-stahl.de/fileadmin/files/mertens-stahl.de/documents/Datenblaetter/Edelstahl/gewalzt/1.4313_X3CrNiMo_13-4_gewalzt.pdf (visited on 04/16/2015).

[10] C. Cagran. "Thermal conductivity and thermal diffusivity of liquid copper". PhD thesis. Graz University of Technology, 2000, p. 78. URL: http://portal.tugraz.at/pls/portal/docs/page/Files/i5110/files/Forschung/Thermophysik/DA-Claus_Cagran.pdf.

[11] Ecodesign Guide of WEEE Compliance Schemes. *Materials - Copper*. 2015. URL: http://eco3e.eu/materials/copper/ (visited on 08/03/2015).

[12] Deutsches Kupferinstitut. *Werkstoff Datenblatt Cu-DHP*. 2005. URL: https://www.kupferinstitut.de/fileadmin/user_upload/kupferinstitut.de/de/Documents/Shop/Verlag/Downloads/Werkstoffe/Datenblaetter/Kupfer/Cu-DHP.pdf (visited on 02/18/2015).

[13] Copper Development Association (CDA). "High Conductivity Coppers for Electrical Engineering". In: *CDA Publication* 122 (1998). URL: http://docs/librariesprovider5/pub-122-hicon-coppers-for-electrical-engineering-pdf.pdf?sfvrsn=2.

[14] Oriental Copper Co., Ltd. *Material Safety Data Sheet Copper Anode: Cu-DHP*. 2010. URL: http://www.orientalcopper.com/admin_oc/images/Meterial-safety-data-sheet-copper-anode.pdf (visited on 03/23/2015).

[15] EFunda. *Element Information: Copper*. 2015. URL: http://www.efunda.com/materials/elements/element_info.cfm?Element_ID=Cu (visited on 03/25/2015).

[16] D. Lide, A. R., and G. Baysinger. *CRC Handbook of Chemistry and Physics*. Boca Raton, FL, 2005. URL: http://www.tau.ac.il/$\sim$chemlaba/Files/CRCPress-2004-CRCHandbookofChemistryandPhysics,85.pdf.

[17] C. J. Smithells. *Smithells Metals Reference Book*. Ed. by E. A. Brandes. 6th ed. London: Butterworth & Co Ltd, 1983. ISBN: 0-408-71053-5.

[18] J. Lee, W. Shimoda, and T. Tanaka. "Surface Tension and its Temperature Coefficient of Liquid Sn-X (X=Ag, Cu) Alloys". In: *Materials Transactions* 45.9 (2004), pp. 2864–2870. ISSN: 1345-9678.

[19] J. Brillo and I. Egry. "Surface tension of nickel, copper, iron and their binary alloys". In: *Journal of Materials Science* 40 (2005), pp. 2213–2216.

[20] The Engineering Toolbox. *Melting and Boiling Temperatures*. 2012. URL: http://www.engineeringtoolbox.com/melting-boiling-temperatures-d_392.html (visited on 03/25/2015).

[21] J. Garai. "Physical model for vaporization". In: *Fluid Phase Equilibria* 283.1-2 (2009), pp. 89–92. ISSN: 03783812. arXiv: 0611289 [physics].

[22] Copper Development Association (CDA). *Webpage: Copper Development Association*. URL: http://copperalliance.org.uk/ (visited on 02/12/2015).

[23] Deutsches Kupferinstitut. *Kupfer-Zinn-Knetlegierungen (Zinnbronzen)*. Tech. rep. Düsseldorf: Deutsches Kupferinstitut, 2004.

[24] Deutsches Kupferinstitut. *Werkstoff Datenblatt CuSn4*. 2005. URL: https://www.kupferinstitut.de/fileadmin/user_upload/kupferinstitut.de/de/Documents/Shop/Verlag/Downloads/Werkstoffe/Datenblaetter/Bronze/CuSn4.pdf (visited on 06/23/2015).

[25] Deutsches Kupferinstitut. *Werkstoff Datenblatt CuSn8*. 2005. URL: https://www.kupferinstitut.de/fileadmin/user_upload/kupferinstitut.de/de/Documents/Shop/Verlag/Downloads/Werkstoffe/Datenblaetter/Bronze/CuSn8.pdf (visited on 06/23/2015).

[26] Deutsches Kupferinstitut. *Werkstoff Datenblatt CuSn10-C*. 2005. URL: https://www.kupferinstitut.de/fileadmin/user_upload/kupferinstitut.de/de/Documents/Shop/Verlag/Downloads/Werkstoffe/Datenblaetter/Bronze/CuSn10-C.pdf (visited on 06/23/2015).

[27] Deutsches Kupferinstitut. *Werkstoff Datenblatt CuSn12-C*. 2005. URL: https://www.kupferinstitut.de/fileadmin/user_upload/kupferinstitut.de/de/Documents/Shop/Verlag/Downloads/Werkstoffe/Datenblaetter/Bronze/CuSn12-C.pdf (visited on 06/23/2015).

[28] G. Mayer, J. Zähr, and U. Füssel. *Schweißen von Kupfer und Kupferlegierungen*. 2009. URL: http://www.kupferinstitut.de/front_frame/frameset.php3?client=1&parent=19&idcat=19&lang=1&sub=yes (visited on 02/18/2015).

[29] N. Enzinger. *Personal communication*. Graz, 2015.

[30] S. Claesson and U. Ronneteg. *Electron beam welding of copper lids*. Tech. rep. Stockholm: Swedish Nuclear Fuel and Waste Management Co, 2003.

[31] B. von Brömssen. *Electron Beam Welding of Thick Copper Material*. Tech. rep. August. Stockholm, 2002.

[32] C. N. Ribton and R. E. Andrews. *Canister sealing for high level waste encapsulation*. 2001. URL: http://www.twi-global.com/technical-knowledge/published-papers/canister-sealing-for-high-level-waste-encapsulation-may-2001/ (visited on 02/19/2015).

[33] W. H. Bowyer. *Design Basis For The Copper/Steel Canister*. Tech. rep. Stage Four, Final Report. Swedish Nuclear Power Inspectorate, 1998.

[34] H. Aalto. *EB-welding of the copper canister for the nuclear waste disposal*. Tech. rep. Outokumpu Oy Poricopper, 1998. URL: http://www.iaea.org/inis/collection/nclcollectionstore/_public/30/013/30013963.pdf.

[35] G. R. LaFlamme and D. E. Powers. "Electron Beam Welding of Copper Containers to Encapsulate nuclear Waste". In: *Welding Journal* December (1994), pp. 37–40.

[36] P. Y. Y. Maak. *Electron Beam Welding of thick-walled Copper Containers for Nuclear Fuel Waste Disposal*. Tech. rep. Ontario hydro research division, 1985.

[37] H. Schultz. *Electron beam welding*. Woodhead Publishing Ltd, 1993, p. 232. ISBN: 1-85573-050-2.

[38] S. Böhm. *The electron beam as a tool for joining technology*. Tech. rep. Düsseldorf: Research Association for Welding and Allied Processes of DVS, 2014.

[39] P. Dobrinski, G. Krakau, and A. Vogel. *Physik für Ingenieure*. 12th ed. Wiesbaden: Vieweg+Teubner — GWV Fachverlage GmbH, 2010. ISBN: 978-3-8348-0580-5.

[40] V. Adam, U. Clauß, D. Dobeneck v., T. Krüssel, and T. Löwer. *Elektronenstrahlschweißen - Grundlagen einer faszinierenden Technik*. pro-beam AG & Co. KGaA, 2011. URL: http://www.pro-beam.com/fileadmin/userdaten/dokumente/BlaueBuecher/Band1_Grundlagen_gesamt.pdf.

[41] S. Schiller, U. Heisig, and S. Panzer. *Elektronenstrahltechnologie*. 1. Auflage. Berlin: VEB Verlag Technik, 1976.

[42] American Welding Society (AWS) C7 Committee on High Energy Beam Welding and Cutting. *Recommended Practices for Electron Beam Welding and Allied Processes*. 4th ed. Doral, Florida: American Welding Society, 2013. ISBN: 978-0-87171-835-8.

[43] A. Klassen, A. Bauereiß, and C. Körner. "Modelling of electron beam absorption in complex geometries". In: *Journal of Physics D: Applied Physics* 47.6 (2014). ISSN: 0022-3727.

[44] E. H. Darlington. “Backscattering of 10-100 keV electrons from thick targets”. In: *Journal of Physics D: Applied Physics* 8.1 (1975), pp. 85–93. ISSN: 0022-3727.

[45] M. P. Groover. *Fundamentals of Modern Manufacturing: Materials, Processes and Systems*. 4th ed. Hoboken, New Jersey: John Wiley & Sons, Inc., 2010. ISBN: 978-0470-467008.

[46] C. Liebig. *Email correspondence (pro-beam AG & Co. KGaA)*. 2015.

[47] G. Petzow. *Metallographisches Keramographisches Plastographisches Ätzen*. 6th ed. Berlin, Stuttgart: Gebrüder Borntraeger, 2006.

[48] M. Carin, P. Rogeon, D. Carron, P. Le Masson, and D. Couëdel. *Numerical Simulation of Electron Beam Welding and Instrumental Technique*. 2004.

[49] G. Weber. *Email correspondence*. Graz, 2015.

[50] Z. Li, K. Mukai, M. Zeze, and K. C. Mills. “Determination of the surface tension of liquid stainless steel”. In: *Journal of materials science* 40 (2005), pp. 2191–2195. ISSN: 0022-2461. URL: `http://link.springer.com/article/10.1007/s10853-005-1931-x`.

[51] E. Valdaitseva. *Email correspondence*. 2015.

[52] V. Somonov, S. Böhm, M. Geyer, and S. Bertelsbeck. “Study on the Effect of Induction Heating to prevent Hot Cracking during Laser Welding of Aluminum Alloys”. In: *The Paton Welding Journal* 4 (2013), pp. 26–33.

[53] V. M. Levshakov, N. A. Steshenkova, and N. A. Nosyrev. “High-Production Laser and Plasma Welding Technologies for High-Speed Vessels Production”. In: *International Journal of Mechanical, Aerospace, Industrial and Mechatronics Engineering* 8.9 (2014), pp. 1595–1600.

[54] U. Dilthey, A. Goumeniouk, V. Lopota, and G. Turichin. “Kinetic description of keyhole plasma in laser welding”. In: *Journal of Physics D: Applied Physics* 33 (2000), pp. 2747–2753. ISSN: 0022-3727.

[55] G. Turichin, V. Lopota, E. Zemliakov, E. Pozdeeva, A. Grigoriev, A. Gumenyuk, and U. Dilthey. “Kinetics of optical Discharge in Plasma Plume during Laser Welding in Shielding Gas”. In: *Laser Technologies in Welding and Materials Processing*. Ed. by B. E. Paton and V. S. Kovalenko. Kiev: E. O. Paton Electric Welding Institute, 2005, pp. 49–53. ISBN: 966-8872-01-0.

[56] G. Turichin, V. Lopota, E. Valdaitseva, E. Zemlyakov, and V. Kirichenko. “Hybrid laser welding - theory, modeling and advantages”. In: *Beam technologies & Laser application*. Ed. by V. Lopota and G. Turichin. St. Petersburg: Publishing house SPbSPU, 2006, pp. 41–49. ISBN: 5-7422-1373-5.

[57] V. Lopota, G. Turichin, E. Valdaitseva, E. Beyer, and S. Voellmar. “Calculation of Convection Effect in the Melt Pool versus Cavity Shape in Laser Welding with Deep Penetration”. In: *Лазерные технологии и средства их реализации*. St. Petersburg, 2004, pp. 127–133.

[58] G. Turichin, E. Zemljakov, E. Pozdeeva, and A. Abdurachmanov. “Modeling of Heat Field in Weld Bath with Consideration of Material Evaporation During Pulse Laser Welding in Vacuum”. In: *Лазерные технологии и средства их реализации*. St. Petersburg, 2004, pp. 181–184.

[59] G. Turichin, E. Valdaitseva, O. Klimova, T. Hassel, and A. Beniyash. “Modelling of influence of dynamic processes in the laser, laser-arc and electron-beam welding on the formation of defects in welded joints”. In: *11th International Seminar - Numerical Analysis of Weldability*. Graz, Seggau, 2015.

[60] G. Turichin, E. Valdaitseva, E. Pozdeeva, U. Dilthey, and A. Gumeniuk. "Theoretical Investigation of Dynamic Behavior of Molten Pool in Laser and Hybrid Welding with Deep Penetration". In: *The Paton Welding Journal* 7 (2008), pp. 11–15. ISSN: 0957-798X.

[61] G. Turichin, E. Valdaytseva, I. Tzibulsky, A. Lopota, and O. Velichko. "Simulation and Technology of Hybrid Welding of Thick Steel Parts with High Power Fiber Laser". In: *Physics Procedia* 12 (2011), pp. 646–655. ISSN: 18753884. URL: http://dx.doi.org/10.1016/j.phpro.2011.03.081.

[62] G. Turichin. *Personal communication*. St. Petersburg, 2015.

[63] E. Valdaitseva. *Personal communication*. St. Petersburg, 2015.

[64] European Committee for Standardization (CEN) ISO TC 44/SC 10. *ISO 14744-1:2008 – Welding – Acceptance inspection of electron beam welding machines – Part 1: Principles and acceptance conditions*.

[65] European Committee for Standardization (CEN) ISO TC 44/SC 10. *ISO 14744-2:2000 – Welding – Acceptance inspection of electron beam welding machines – Part 2: Measurement of accelerating voltage characteristics*.

[66] European Committee for Standardization (CEN) ISO TC 44/SC 10. *ISO 14744-3:2000 – Welding – Acceptance inspection of electron beam welding machines – Part 3: Measurement of beam current characteristics*.

[67] European Committee for Standardization (CEN) ISO TC 44/SC 10. *ISO 14744-4:2000 – Welding – Acceptance inspection of electron beam welding machines – Part 4: Measurement of welding speed*.

[68] European Committee for Standardization (CEN) ISO TC 44/SC 10. *ISO 14744-5:2000 – Welding – Acceptance inspection of electron beam welding machines – Part 5: Measurement of run-out accuracy*.

[69] European Committee for Standardization (CEN) ISO TC 44/SC 10. *ISO 14744-6:2000 – Welding – Acceptance inspection of electron beam welding machines – Part 6: Measurement of stability of spot position*.

[70] K. Siebertz, D. van Bebber, and T. Hochkirchen. *Statistische Versuchsplanung - Design of Experiments (DoE)*. Springer-Verlag Berlin Heidelberg, 2010. ISBN: 978-3-8349-8484-5.

[71] Minitab Inc. *Software: Minitab 17.2.1*. 2015. URL: http://www.minitab.com.

[72] A. Munteanu and G. Nagit. "The influence of the input parameter in case of electron beam welding". In: *1st International Conference on Manufacturing Engineering, Quality and Production Systems*. Vol. II. Romania, 2009, pp. 484–488. ISBN: 978-960-474-122-9.

[73] C. G. Menhard and T. Löwer. "Die Elektronenstrahlgeometrie - Definition, Vermessung und Bedeutung für den Schweißprozess". In: *Schweißen und Schneiden* 61.2 (2009), pp. 68–73.

[74] B. Buchmayr. *Werkstoff- und Produktionstechnik mit Mathcad*. Berlin: Springer-Verlag Berlin Heidelberg, 2002. ISBN: 978-3-540-43014-8.

[75] Dassault Systems. *Software: CATIA V5 R19*. 2010.

[76] C. Wiednig. *Email correspondence*. Graz, 2015.

[77] Mikron Instrument Company Inc. "Table of emissivity of various surfaces". URL: http://www-eng.lbl.gov/dw/projects/DW4229_LHC_detector_analysis/calculations/emissivity2.pdf.

[78] G. Turichin, E. Valdaytseva, and P. Fritzl. “Computer Simulation of Electron Beam Welding of Copper Alloys”. In: *8th International Conference - Beam Technologies & Laser Application*. St. Petersburg, 2015.

[79] Deutsches Institut für Normung e.V. - Gemeinschaftsausschuss NA 092-00-15 AA. *DIN 32511:2007-03 – Welding – Electron beam process for material treatment – Terms for processes and equipment.*